UNIVERSITY OF CALIFORNIA
RIVERSIDE

Solid-State NMR Spectroscopy and Computational Modeling for Structure Elucidation

A Dissertation submitted in partial satisfaction
of the requirements for the degree of

Doctor of Philosophy

in

Chemistry

by

Winn Huynh

June 2022

Dissertation Committee:
Dr. Matthew P. Conley, Chairperson
Dr. Richard J. Hooley
Dr. Yadong Yin

The Dissertation of Winn Huynh is approved:

_____

_____

_____

Committee Chairperson

University of California, Riverside

Acknowledgments

I would like to express my greatest gratitude to Dr. Matthew P. Conley, who has been an exceptional mentor for these past six years. Under his guidance, I have learned to appreciate a wide variety of chemistry, meticulously analyze data, explore organometallic chemistry syntheses, and develop a joy for computational chemistry. I would also like to thank Dr. Leonard J. Mueller, who provided me guidance on navigating the math behind rank-2 tensors and for developing TensorView, which was used in several publications, and for the use of your 400 MHz spectrometer. I thank Dr. Gregory Beran who taught me the basics of computational chemistry and helped me with Gaussian 09 during my first year as a graduate student. In addition, I would like to thank Dr. Hosein Tafazolian who patiently and personally mentored me during my first year in the development of my Schlenk technique, NMR spectral analysis, and glove box skills.

I thank Dr. Richard J. Hooley and Dr. Yadong Yin, whom both provided insightful commentary on my qualifying exam and dissertation and helped me to better communicate my research. I also thank Dr. Jordan Taylor and Dr. Hill Harman for providing the B_2P_2 complexes which resulted in a collaborative publication. I thank the Rossini group (Amrit and Rick) at Iowa State University for their NMR expertise in obtaining structural parameters for Chapter 7 and another published work. To Damien, Jessica, Jiaxin, Kavya, Max, and Sumeng, thank you for being a part of my graduate school journey, for the academic and mental support, and for the remarkable memories. Thank you for becoming my second family, my home away from home, and always being there when I needed either a hand or an ear.

To my undergraduate research mentors: Dr. Richard Kaner and Dr. Jeffrey Long, thank you for the research opportunities in inorganic chemistry and air- and water- free syntheses. I especially thank Jaime Torres, my graduate student mentor, who introduced me to UC LEADS, which without I would not be where I am today. I thank Dr. Tama Hasson, Diana Lizarraga, and Dr. Devin Horton for their overwhelming support of me and helping me to realize my potential when I was not at my best academically. Thank you for the second chance, a fresh beginning, and for encouraging me become a mature scientist.

To my high school teachers Mrs. Trang Tong, Mrs. Jennifer Daniels, Ms. Betty Erdos, Ms. Lynn Dominguez, and Ms. Marilyn Corbett, thank you for an engaging curriculum and for being with me when I wanted to pursue the AP Sciences. Thank you for the early mornings, long nights, and fun weekends in Science Olympiad and the Science Department. Thank you for teaching me how to experience science in high school and for supporting me in my applications to college. I also express my thanks to Ms. Sarah Hunter and Mr. Bret Loewen, who always stressed the importance and relevance of writing well regardless of whichever career path I select.

To Dr. Matthew D. Casselman and Dr. Kevin Kou, thank you for the extra push towards the later years of my graduate career and for the motivation to finish strong. Thank you for spurring me on towards my career goal of one day becoming a chemistry faculty member and for training me to become a better communicator and educator. Thank you for the countless discussions in organic chemistry, in chemical education, and in helping me to appreciate a field of chemistry that I once was not mature enough to during my undergraduate years.

The text, figures, and schemes for the following chapters have been reproduced in part from the following published manuscripts:

Chapter 2: The β-Agostic Structure in $(C_5Me_5)_2Sc(CH_2CH_3)$: Solid-State NMR Studies of $(C_5Me_5)_2Sc$-R (R = Me, Ph, Et)

Culver, D. B.*; Huynh, W.; Tafazolian, H.*; Ong, T.-C.*; Conley, M. P. *Angew. Chem. Int. Ed.* **2018**, *57*, 9250-9253.

Chapter 3: Solid-state 45Sc NMR of Cp^*_2Sc-X and $Cp^*_2ScX(THF)$

Huynh, W.*; Culver, D. B.*; Tafazolian, H.*; Conley, M. P.* *Dalton Trans.* **2018**, *47*, 13063-13071.

Chapter 4: Solid-State ^{45}Sc NMR Studies of Cp^*_2Sc-OR (R = CMe_2CF_3, $CMe(CF_3)_2$, $C(CF_3)_3$, $SiPh_3$) and Relationship to the Structure of Cp^*_2Sc-sites Supported on Partially Dehydroxylated Silica.

Culver, D. B.*; Huynh, W.; Tafazolian, H.*; Conley, M. P. *Organometallics*, **2020**, *39*, 1112-1122.

Chapter 5: Solid-State ^{11}B NMR Studies of Coinage Metal Complexes Containing a Phosphine Substituted Diboraantracene Ligand

Huynh, W.*; Taylor, J. T.*; Harman, H. H.; Conley, M. P. *Dalton Trans.* **2021**, *50*, 14855-14863.

Chapter 6: Origin of the ^{29}Si NMR Chemical Shift in R_3Si-X and Relationship to Formation of Silylium (R_3Si^+) Ions

Huynh, W.; Conley, M. P. Dalton Trans. **2020**, *49*, 16453-16463.

Chapter 7: Formation of a Strong Heterogeneous Aluminum Lewis Acid on Silica

Samudralala, K.*; Huynh, W. Dorn, R. W.*; Rossini, A. J.; Conley, M. P. *Manuscript In Preparation*

* denotes co-author(s) who synthesized the compounds and/or ran experimental spectra.

The co-author (Matthew P. Conley) listed in the above publications directed and supervised the research which forms the basis for this dissertation.

ABSTRACT OF THE DISSERTATION

Solid-State NMR Spectroscopy and Computational Modeling for Structure Elucidation

by

Winn Huynh

Doctor of Philosophy, Graduate Program in Chemistry
University of California, Riverside, June 2022
Dr. Matthew P. Conley, Chairperson

Multinuclear solid-state NMR spectroscopy and computational modeling are powerful techniques for the elucidation of chemical structure. Multinuclear $^{45}Sc\{^{1}H\}$ and $^{13}C\{^{1}H\}$ CPMAS NMR spectra unambiguously assigns a β-CH agostic interaction in $Cp^*_2Sc\text{-}CH_2CH_3$, a compound synthesized by Bercaw and co-workers in 1987. The quadrupolar coupling constant (C_Q) obtained in $^{45}Sc\{^{1}H\}$ solid-state NMR for three-coordinate scandocenes $Cp^*_2Sc\text{-}R$ (R = Ph, Me, $OSiPh_3$, $OCMe_2CF_3$, $OCMe(CF_3)_2$, $C(CF_3)_3$), $Cp^*_2Sc\text{-}X$ (X = F, Cl, Br, I), and $Cp^*_2Sc\text{-}OR$ are large (C_Q > 27MHz), but for four-coordinate THF adducts of $Cp^*_2Sc\text{-}X$ are small (C_Q < 26 MHz). The C_Q (^{45}Sc) of $Cp^*_2Sc\text{-}X$ and $Cp^*_2Sc\text{-}X(THF)$ are affected by the local coordination environment at Sc. When supported on silica partially dehydroxylated at 700 ^{o}C, Cp^*_2ScMe reacts to form methane and, $Cp^*_2ScOSi{\equiv}$ (C_Q = 35.4 MHz), and $Cp^*_2Sc(OSi{\equiv})O(SiO_x)_2$ (C_Q = 21.9 MHz).

These differences are related to the change in symmetry at scandium. The C_Q is also affected by coordination of a metal to boron in complexes containing the phosphine substituted 9,10-diboraantracene ligand B_2P_2. Coordination of B_2P_2 to a coinage metal in a cationic environment forms $[M(B_2P_2)][PF_6]$ (M = Cu, Ag, Au), in which the borane is three-coordinate, exhibits trigonal planar geometry, and contains a large C_Q > 4 MHz. Formation of the boro-auride $[K(18\text{-}c\text{-}6)][Au(B_2P_2)]$ forms a tetrahedral boron, and the ^{11}B NMR signals for this compound a small C_Q of 1.5 MHz. The natural localized molecular orbitals for each can be calculated, and the contribution of each bonding orbital can be analyzed. The ^{29}Si NMR chemical shift of $R_3Si\text{-}X$ (R = ^{i}Pr) is also studied via solid-state NMR, and calculations reveal that the magnitude of the coupling of the occupied σ(Si-R) to the unoccupied σ(Si-X) / p_{Si} is responsible for the deshielding of ^{29}Si. These results allow for the elucidation of structure in $[^{i}Pr_3Si][MO_x]$ (MO_x = sulfated zirconia and $Al(OC(CF_3)_3)_3$ activated $SiO_{2\text{-}700}$).

Table of Contents

Chapter 1: Introduction……..……**1**

1.1 Origin of the NMR Chemical Shielding……1

1.2 The Chemical Shielding Tensor……..2

1.3 The Electric Field Gradient Tensor…….8

1.4 Visualization of the CST and EFG Tensors……13

1.5 Objective of the Dissertation……14

1.6 References……16

Chapter 2: The Beta-Agostic Structure in $(C_5Me_5)_2ScCH_2CH_3$ – Solid-State NMR Studies of $(C_5Me_5)_2Sc$-R (R = Me, Ph, Et)……..……**19**

2.1 Abstract……19

2.2 Introduction……..19

2.3 Results and Discussion……..……..23

2.4 Conclusion……30

2.5 Materials and Methods…….31

2.6 References……36

Chapter 3: Solid-state ^{45}Sc NMR Studies of Cp^*_2Sc-X and $Cp^*_2ScX(THF)$……**38**

3.1 Abstract……38

3.2 Introduction……38

3.3 Results and Discussion.....……39

3.4 Conclusion……52

3.5 Materials and Methods…….53

3.6 References……57

Chapter 4: Solid-state ^{45}Sc NMR Studies of Cp^*_2Sc-OR (R = CMe_2CF_3, $CMe(CF_3)_2$, $C(CF_3)_3$, $SiPh_3$) and Relationship to the Structure of Cp^*_2Sc-Sites Supported on Partially Dehydroxylated Silica..…..…….……**59**

4.1 Abstract……59

4.2 Introduction……..60

4.3 Results and Discussion……..……..63

4.4 Conclusion……72

4.5 Materials and Methods……72

4.6 References……77

Chapter 5: Solid-state ^{11}B NMR Studies of Coinage Metal Complexes Containing a Phosphine Substituted Diboraanthracene Ligand……..……..…...**78**

5.1 Abstract……78

5.2 Introduction……..78

5.3 Results and Discussion…….81

5.4 Conclusion……95

5.5 Materials and Methods…….95

5.6 References……97

Chapter 6: Origin of the ^{29}Si NMR Chemical Shift in R_3Si-X and Relationship to the Formation of Silylium (R_3Si^+) Ions……**99**

6.1 Abstract……99

6.2 Introduction……..99

6.3 Results and Discussion……...102

6.4 Conclusion……...…118

6.5 Materials and Methods……...118

6.6 References……..120

Chapter 7: Formation of a Strong Heterogeneous Aluminum Lewis Acid on Silica.....**122**

7.1 Abstract……..122

7.2 Introduction……122

7.3 Results and Discussion……...124

7.4 Conclusion……..131

7.5 Materials and Methods……...132

7.6 References……..135

Chapter 8: Conclusion……...137

List of Figures

Figure 1.1 The Zeeman effect……..1

Figure 1.2 The chemical shielding tensor and related equations……..2

Figure 1.3 Simulated solid-state ^{13}C NMR spectra at various magic-angle spinning speeds……..4

Figure 1.4 Simulated solid-state ^{13}C NMR for various Ω and κ values……5

Figure 1.5 Orbital rotation model for a typical carbene……6

Figure 1.6 Arduengo's first isolated carbene and Chugaev's salt……7

Figure 1.7 The electric field gradient tensor and related equations ……8

Figure 1.8 Simulated solid-state ^{45}Sc NMR spectra with various C_Q and η values……...9

Figure 1.9 Schematic of $AlMes_3$ and $Al(NTMS_2)_3$.....11

Figure 1.10 The C_Q of $Cp_2ZrClCH_3$ and Cp_2ZrHCl. X-ray crystal structure of Cp_2ZrHCH_3 and MicroED structure of Cp_2ZrHCl……..12

Figure 1.11 Spherical polar plots of rank-2 tensors……14

Figure 2.1 Examples of C-H agostic interactions……...20

Figure 2.2 X-ray crystal structure of Cp^*_2Sc-Et……21

Figure 2.3 Static $^{45}Sc\{^1H\}$ NMR spectra of Cp^*_2Sc-R (R = Me, Ph, Et)……24

Figure 2.4 3QMAS $^{45}Sc\{^1H\}$ NMR spectra of Cp^*_2Sc-Et at 0 °C……..24

Figure 2.5 $^{13}C\{^{1}H\}$ CPMAS NMR spectra of Cp^*_2Sc-Et spinning at 1.25 kHz…….25

Figure 2.6 Simulation of $^{13}C\{^{1}H\}$ CPMAS NMR spectra for C_β of Cp^*_2Sc-Et spinning at 1.25 kHz…….26

Figure 2.7 Simulation of $^{13}C\{^{1}H\}$ CPMAS NMR spectra for C_α of Cp^*_2Sc-Et spinning at 1.8 kHz……...26

Figure 2.8 Plot of C_Q and Ω versus Sc-C_α-C_β angle relative to SCF energy……29

Figure 2.9 Calculated structural parameters and CST orientation of of Cp^*_2Sc-Et and the associated orbital rotation models for C_α and C_β…….30

Figure 2.10 CST of Cp^*_2Sc-R (R = Me, Ph, Et)…….33

Figure 2.11 NLMO contributions to $\sigma_{11}(^{13}C)$ for Cp^*_2Sc-Et……..35

Figure 3.1 X-ray crystal structures of Cp^*_2Sc-X (X = F, Cl, Br, I)…….40

Figure 3.2 Solid-state ^{45}Sc NMR spectra for Cp^*_2Sc-X……...……..41

Figure 3.3 Geometry optimized Cp^*_2Sc-X(THF)……..42

Figure 3.4 Geometry optimized Cp^*_2Sc-X……44

Figure 3.5 Solid-state 45Sc NMR spectra for Cp^*_2Sc-X(THF)……45

Figure 3.6 EFG tensor plots for Cp^*_2Sc-X and Cp^*_2Sc-X(THF)……..49

Figure 3.7 NLMO contributions to V_{33} for Cp^*_2Sc-X…..…….50

Figure 3.8 NLMO contributions to V_{33} for Cp^*_2Sc-X(THF)…….51

Figure 3.9 Qualitative molecular orbitals in Cp^*_2Sc-X and Cp^*_2Sc-X(THF)……52

Figure 4.1 Summary of known ^{45}Sc quadrupolar coupling constants…….61

Figure 4.2 DFT models for $Cp^*_2ScOSi\equiv$ and $Cp^*_2Sc(OSi\equiv)O(SiO_x)_2$…….63

Figure 4.3 X-ray crystal structure of Cp^*_2Sc-$OCMe_2CF_3$ and Cp^*_2Sc-$O(C(CF_3)_3$……64

Figure 4.4 FTIR spectra of $Cp^*_2ScOSi\equiv$ (5a) and $Cp^*_2Sc(OSi\equiv)O(SiO_x)_2$ (**5b**)……66

Figure 4.5 Solid-state $^{13}C\{^1H\}$ CPMAS NMR of **5a** and **5b**……..66

Figure 4.6 Static solid-state $^{45}Sc\{^1H\}$ NMR spectra of **1-4**……67

Figure 4.7 Solid-state $^{45}Sc\{^1H\}$ NMR of **5a** and **5b**……67

Figure 4.8 EFG tensor plots for **1-4**, **6ab**……70

Figure 4.9 NLMO contributions to V_{33} for **1-4, 6ab**……..71

Figure 5.1 Selected transition metal compounds with Z-type ligands……79

Figure 5.2 Predicted orbital coupling models for tri- and tetra- coordinate boron……..80

Figure 5.3 Coinage metal complexes of B_2P_2……81

Figure 5.4 $^{11}B\{^1H\}$ NMR spectra of B_2P_2 at 9.4T……..82

Figure 5.5 Calculated structures for various B_2P_2 model structures……...83

Figure 5.6 Solid-state $^{11}B\{^1H\}$ NMR spectra for **1-4** obtained at 14.1 T……86

Figure 5.7 Solid-state $^{11}B\{^1H\}$ NMR spectra for **1-4** obtained at 9.1 T……..87

Figure 5.8 Calculated EFG tensor plots of **1-4**……...90

Figure 5.9 NLMO contributions to V_{33} for **3** and **4** and relevant orbitals……91

Figure 5.10 NLMO contributions to V_{33} for **1** and **2**……..92

Figure 5.11 CST and orbital coupling model for deshielding in **3** and **4**…….93

Figure 5.12 Qualitative molecular orbital analysis of for deshielding in **3** and **4**……94

Figure 6.1 Selected ^{29}Si NMR chemical shifts in R_3Si-X and [R_3Si][X]……..100

Figure 6.2 CST for N-heterocyclic silylene and orbital coupling for deshielding…..…..101

Figure 6.3 Structures **1-17**……...103

Figure 6.4 DFT calculated structures of **14-17**…….106

Figure 6.5 Plot of calculated and experimental ^{29}Si NMR chemical shift for selected R_3Si-X and [R_3Si][X]……...108

Figure 6.6 Simulated ^{29}Si NMR spectra of **10**, **3**, **5**, **2**, **1**……...110

Figure 6.7 Comparison of σ, σ^d, σ^p versus $\delta(^{29}Si)$ for σ_{11} in **1-17**…….111

Figure 6.8 CST plots of **1-17**……113

Figure 6.9 NLMO contributions to $\sigma_{11,}$ $\sigma_{22,}$ and σ_{33} for **1**……..114

Figure 6.10 Qualitative molecular orbital diagram of orbital coupling in **1**…..……114

Figure 6.11 Orientation of the CST in **5**, **7-9**……115

Figure 6.12 Total diamagnetic and paramagnetic contribution to the isotropic chemical shielding tensor for **5**, **7-9**…….116

Figure 6.13. Plots of ^{29}Si NMR chemical shift versus charge……...117

Figure 7.1 Isodesmic reaction for the calculation of ion affinity……..123

Figure 7.2. FTIR spectra of 1 and $SiO_{2\text{-}700}$……...125

Figure 7.3 Static ^{27}Al NMR Spectrum of **1** at 14.1T…….126

Figure 7.4. Calculated structures of **1**……..127

Figure 7.5. $^{13}C\{^{1}H\}$ CPMAS NMR spectrum of $Cp_2Zr(^{13}CH_3)_2$/**1**……..129

Figure 7.6. $^{27}Al\{^{1}H\}$ MAS spectrum of **3** spinning at 10kHz……...129

Figure 7.7. $^{13}C\{^{27}Al\}$ PM-RESPDOR curve of **3**……130

Figure 7.8 DFT calculated structure of **3**……..131

List of Tables

Table 2.1 Kinetic studies of ethylene oligomerization……..21

Table 2.2 ^{13}C NMR parameters of Cp*$_2$Sc-Et……27

Table 2.3 Experimental and calculated C_Q for Cp*$_2$Sc-R (R = Me, Ph, Et)……27

Table 2.4 NLMO contributions to Cp*$_2$Sc-Et……34

Table 3.1 Selected structural parameters for Cp*$_2$Sc-X (X = F, Cl, Br, I)……..40

Table 3.2 Experimental ^{45}Sc NMR parameters for Cp*$_2$Sc-X……41

Table 3.3 Calculated ^{45}Sc NMR parameters for Cp*$_2$Sc-X and Cp*$_2$Sc-X(THF)……..…43

Table 3.4 Selected structural parameters for geometry optimized Cp$^*_2$Sc-X…….44

Table 3.5 Selected structural parameters for geometry optimized Cp$^*_2$Sc-X(THF)……44

Table 4.1 Experimental ^{45}Sc NMR Parameters for **1-5**……..……68

Table 4.2 Geometrical parameters for DFT optimized structures of 1-4, 6ab…….69

Table 4.3 Calculated ^{45}Sc NMR Parameters for 1-4, 6ab……...69

Table 5.1 Simulated ^{11}B{^{1}H} NMR parameters for B_2P_2……...82

Table 5.2 Calculated ^{11}B{^{1}H} NMR parameters for B_2P_2……..85

Table 5.3 Experimental ^{11}B{^{1}H} NMR parameters for **1-4**……87

Table 5.4 Crystal structure parameters for **1-4**……...89

Table 5.5 Geometric parameters DFT calculated structures for **1-4**……...89

Table 5.6 DFT calculated ^{11}B NMR parameters for **1-4**…….89

Table 6.1 Key geometric data for **1-17**…….104

Table 6.2 Calculated ^{29}Si NMR parameters of **1-17**…….108

Table 7.1. Fluoride Ion Affinity of Selected Lewis Acids……127

List of Schemes

Scheme 3.1 Synthesis of Cp^*_2Sc-X (X = F, Cl, Br, I)…….39

Scheme 3.2 Synthesis of Cp^*_2Sc-X(THF)…….42

Scheme 4.1 Reaction of organometallic with surface oxide……...60

Scheme 4.2. Synthesis of Cp^*_2ScOR (R = CMe_2CF_3, $CMe(CF_3)_2$, $C(CF_3)_3$, $SiPh_3$)……...63

Scheme 4.3. Synthesis of $Cp^*_2ScOSi\equiv$ and $Cp^*_2Sc(OSi\equiv)O(SiO_x)_2$…….65

Scheme 7.1 Reaction of $SiO_{2\text{-}500}$ with $B(C_6F_5)_3$……...…….123

Scheme 7.2 Synthesis of **1**……124

Scheme 7.3. Reaction of $Cp_2Zr(CH_3)_2$ and **1**……128

CHAPTER 1

Introduction

1.1 Origin of the NMR Chemical Shielding

In the presence of a magnetic field, nuclei containing a magnetic spin I ≥ ½ orient either parallel (α) or anti-parallel (β) to the magnetic field. (Figure 1.1) The population of the α and β spin states is described by the Boltzmann distribution in eq 1.[1] The energy between the α and β states is directly proportional to Planck's constant (6.626 x 10^{-34} m^2 kg s^{-1}), the gyromagnetic ratio (γ) of the nucleus, and the applied magnetic field (B_0) given in eq. 3. The interaction between spin and B_0 is defined by the Zeeman interaction shown in Figure 1.1.

$$\frac{N^{\beta}}{N^{\alpha}} = e^{-\frac{E}{kT}} \qquad (1)$$

$$\Delta E = \gamma h B_0 = h\nu_0 \qquad (2)$$

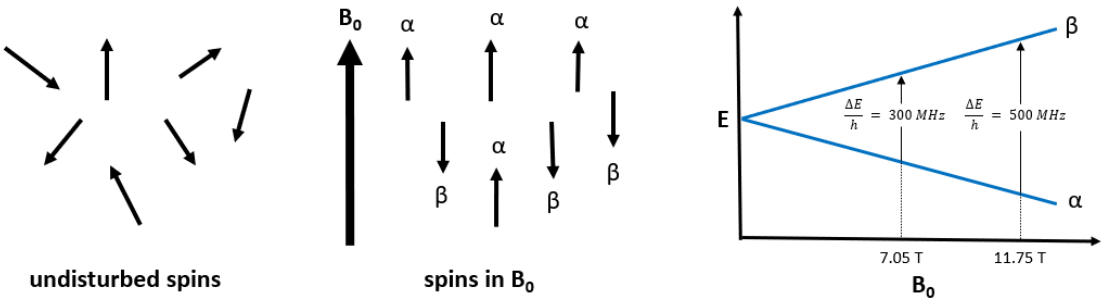

Figure 1.1. The Zeeman effect in a magnetic field and a depiction of the consequences.

Irradiating a sample with radio frequency in a strong magnetic field inverts the α and β spin states, and relaxation of the perturbed system releases energy. The radio

frequency depends on the γ and the chemical environment of the nucleus. In a typical NMR spectrum, the radio frequency is plotted on the x-axis, and the absorption at these frequencies is plotted as the y-axis. The frequency of absorption depends on the chemical shielding of the nucleus in its chemical environment. Chemical shielding values are often converted to chemical shifts and are measured with respect to the shielding of an identical nucleus in a reference sample described by eq. 3.[2] For ^{13}C, ^{1}H, and ^{29}Si NMR, tetramethylsilane is the reference and is assigned the chemical shift value of 0.00 ppm.

$$\delta \equiv \frac{\sigma_{ref} - \sigma}{1 - \sigma_{ref}} \quad (3)$$

1.2 The Chemical Shielding Tensor

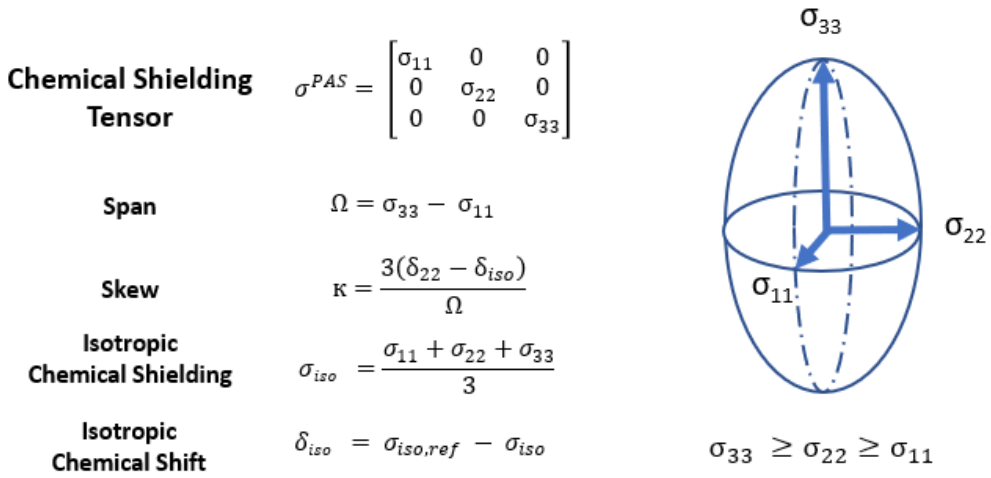

Figure 1.2. Graphical depiction of the chemical shielding tensor and related equations that describe the chemical shielding tensor.

The chemical shielding tensor (CST) is a rank-2 tensor that describes the shielding of electrons around a nucleus and is commonly represented in the principal axis system (PAS).[2] (Figure 1.2) The span (Ω) describes the difference between the smallest (σ_{11}) and

the largest (σ_{33}) components of the CST. The skew (κ) relates the location of σ_{22} with respect to the isotropic chemical shielding, σ_{iso}. The σ_{iso} is the shielding that is referenced to a known standard to obtain the isotropic chemical shift (δ_{iso}).

In solution, the terms of the CST are averaged due to rapid tumbling, and only δ_{iso} is detectable in NMR experiments. In rigid solids, the components of the CST are observable in samples spinning at the magic angle slower than the Ω of the CST. In cases where the magic angle spinning (MAS) speed is smaller than the Ω for a given CST, the isotropic chemical shift is flanked by spinning side bands that appear at intervals equal to the MAS frequency. The intensities of the spinning side bands are related to the individual components of the CST.[3] (Figure 1.3, page 4)

For static solid-state NMR spectra, the chemical shielding anisotropy is observable, and examples of this behavior are shown in Figure 1.4 on page 5 for δ_{iso} = 100ppm with both Ω and κ varied. A low Ω value indicates a CST that is more isotropic, whereas a higher Ω indicates a larger chemical shielding anisotropy which results in a wider peak. When κ is 0 the peak is axially symmetric and situated near δ_{iso}. However, as κ increases towards 1.00, the peak is biased towards the left of the line shape and is much more anisotropic.

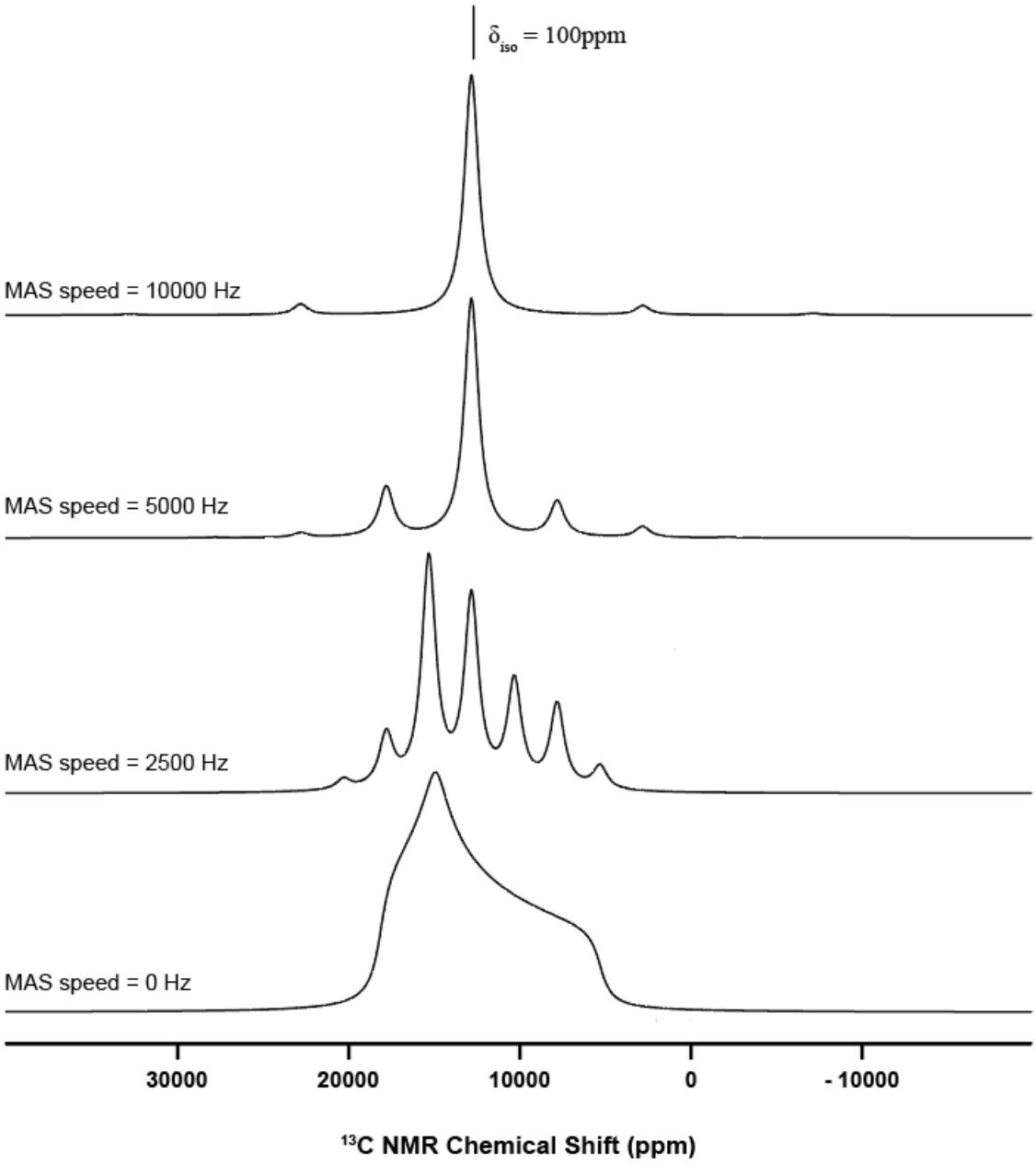

Figure 1.3. Simulated ^{13}C NMR spectra with TopSpin 4.1.1 for $\delta(^{13}C)$ = 100ppm and Ω = 100ppm at various MAS spinning speeds. The κ is set to 0.50, and the line broadening is set to 1000 Hz.

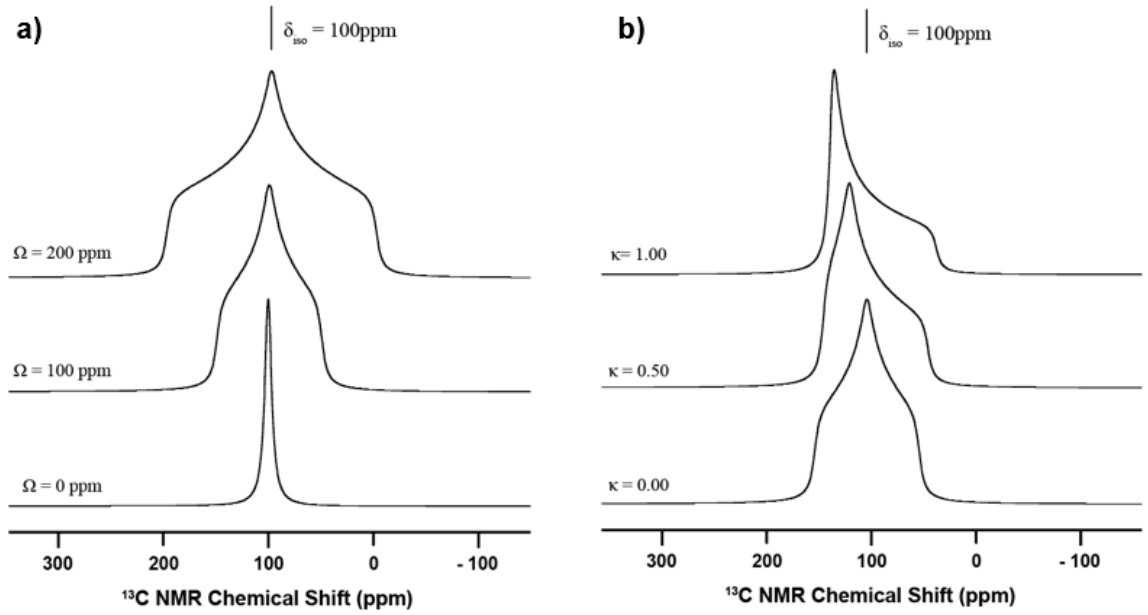

Figure 1.4. Simulated solid-state ^{13}C NMR spectra with various values for Ω (a) for δ(^{13}C) = 100ppm in TopSpin 4.1.1. Various values for κ (b) were also simulated for δ(^{13}C) = 100ppm and Ω = 100ppm.The line broadening is set to 1000 Hz.

Ramsey decomposed chemical shielding into two terms, the diamagnetic and the paramagnetic term.[4a-b] (eq. 4-6) Solvent effects are also known to affect the NMR chemical shift and are represented by σ^m. The diamagnetic term (σ^d) term results from the induction of molecule's electrons in the presence of an applied magnetic field, and all contributions can be readily calculated from the ground-state wave function.[2] The value of σ^d varies little

$$\sigma_{iso} = \sigma^d + \sigma^{p+SO} + \sigma^m \qquad (4)$$

$$\sigma_{ij}^d = \frac{e^2\mu_0}{8\pi m_e}\left\langle\varphi_0\left|\frac{\sum_k(r_{k*}r_{kN}\delta_{ij}^k - r_{kNi}r_{kNj})}{r_{kN}^3}\right|\varphi_0\right\rangle; i,j = x,y,z \qquad (5)$$

$$\sigma_{ij}^p = \frac{\left\langle\varphi_0\left|\hat{L}_{\mathrm{ki}}\right|\varphi_n\right\rangle\left\langle\varphi_n\left|\frac{\widehat{(L_{\mathrm{kNj}})}}{r_{kN}^3}\right|\varphi_0\right\rangle}{\Delta E_{n-0}} \qquad (6)$$

between nuclei in different molecules and is generally not the parameter that affects the chemical shift of nuclei in different chemical environments. In contrast, the paramagnetic shielding (σ^p) results from the coupling of ground-state wavefunction (φ_0) to an excited state wave function (φ_n) through the angular momentum operator ($\hat{L}_{ki,}$ ki = element of the CST) in the presence of an applied magnetic field. (eq. 6) The denominator in eq. 6 shows that the paramagnetic shielding is highest when φ_0 and φ_n are closest in energy. Specifically, σ^p is maximized when φ_0 is the highest occupied molecular orbital (HOMO) and when φ_n is the lowest unoccupied molecular orbital (LUMO). The σ^p also contains spin-orbit coupling if the nucleus interacts with a heavy element and is abbreviated as σ^{p+SO} in the eq.4. The work presented in this dissertation concern lighter nuclei, and the spin-orbit contributions are negligible which result in $\sigma^{p+SO} \approx \sigma^p$. The value of the medium term (σ^m) is dependent on the solvent, and in gas phase calculations is set to 0. [4b]

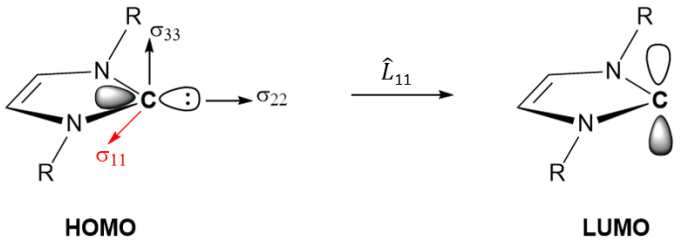

Figure 1.5. Orbital rotation model of a typical carbene for deshielding via the angular momentum operator $\hat{L}_{11}$ through the coupling of the HOMO and LUMO.

Orbital rotations models help visualize the implications of this equation. For example, the ^{13}C chemical shift of N-heterocyclic carbenes (NHC) such as the cyclic diaminocarbenes commonly contain a deshielded carbon with a chemical shift signal beyond 200 ppm.[5-9] (Figure 1.5) The lone pair localized on carbon in the NHC is also the

HOMO. The σ_{11} component of the CST is the most deshielded and is aligned perpendicular to the HOMO. Rotation about the σ_{11} axis ($\hat{L}_{11}$) results in the empty p-orbital that is the LUMO in the NHC. Therefore, the σ^p contribution is large because the HOMO couples to the LUMO, resulting in a deshielded ^{13}C NMR chemical shift for the NHC carbon.

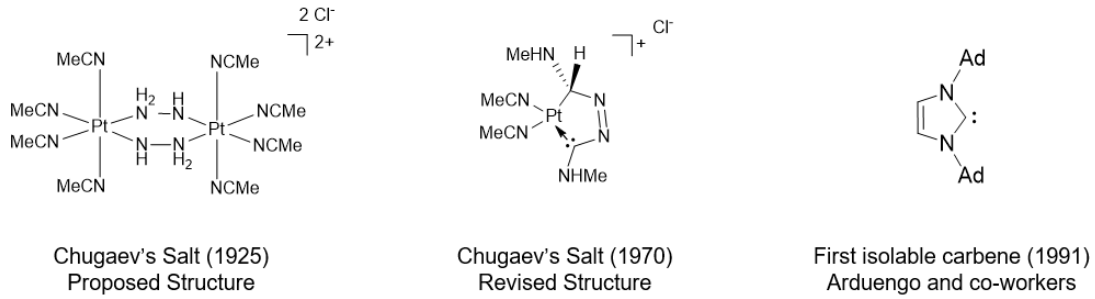

Figure 1.6. Isolated free carbene in 1991 by Arduengo (left) and Chugaev's salt (right).

A molecular orbital understanding of the CST provides information that relates structure and bonding and may even predict reactivity.[7, 10] The free carbene described in Figure 1.6 was first isolated by Kline and coworkers in 1991.[11] Until then, free carbenes were postulated to only exist as intermediates.[12] In contrast, Chugaev's salt, $[Pt_2(N_2H_3)_2(MeNC)_8]Cl_2$, is a metal carbene that was synthesized in 1925 but not correctly characterized to be a metal carbene until 1970 when revisited by Rouschias and Shaw.[13-14] Metal alkylidenes, a class of metal carbenes, are often invoked as key organometallic intermediates in olefin metathesis. They are commonly synthesized from metal alkyls, but not all metal alkyls form alkylidenes. Coperet et al. showed that the ability of metal alkyls to form metal alkylidenes is related to the NMR chemical shift of the α-carbons. Specifically, calculations of a library of metal alkyls revealed that a M-C_α-C_β containing a π-type interaction at C_α increases the ability of the compound to form a metal alkylidene.[10]

1.3 The Electric Field Gradient Tensor

For nuclei with spin greater than ½ (I > ½), the NMR spectra are dramatically impacted by the electric field gradient (EFG) tensor. The EFG tensor describes the distribution of charge, which is sensitive to chemical environment. Like the CST, the EFG is described as a rank-2 tensor. All nuclei contain an EFG tensor, but the EFG tensor only affects NMR spectra when the nucleus contains a quadrupole moment (I > ½). The coupling of the quadrupole moment Q and the EFG tensor produce the quadrupolar coupling constant (C_Q) observed in NMR. Specifically, the C_Q is dependent on the magnitude of Q and the largest component (V_{33}) of the EFG tensor in the principal axis system.[15] (Figure 1.7)

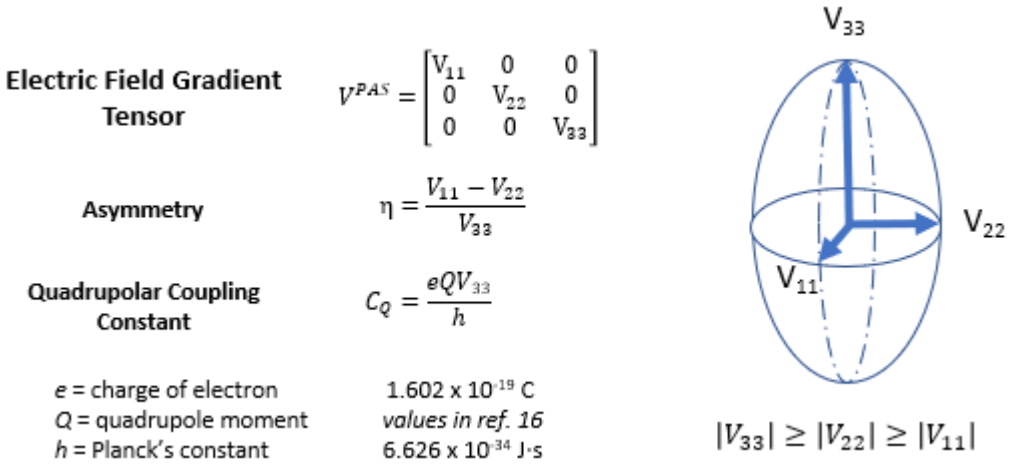

Figure 1.7. Simulated solid-state NMR spectra parameters with various C_Q.

The quadrupolar component of solid-state NMR line shapes is commonly described with a C_Q value and its asymmetry parameter. The consequence of a large C_Q is a broader line shape. Figure 1.8a shows a simulated solid-state ^{45}Sc NMR spectrum (I = 7/2,

γ = - 0.220 barns, 100% natural abundance) containing different C_Q values with η = 0.00. Figure 1.8b shows similar simulations but with C_Q fixed at 30 MHz and η varied. When $V_{11} = V_{22}$, the asymmetry parameter is 0, and the line shape is described as a Pake doublet.[17] When the asymmetry is increased from 0 to 1, the horns of the Pake doublet start to move closer together, until $V_{11} - V_{22} = V_{33}$, which has η = 1.00. The consequence of η = 1.00 is a line shape that is axially symmetric.

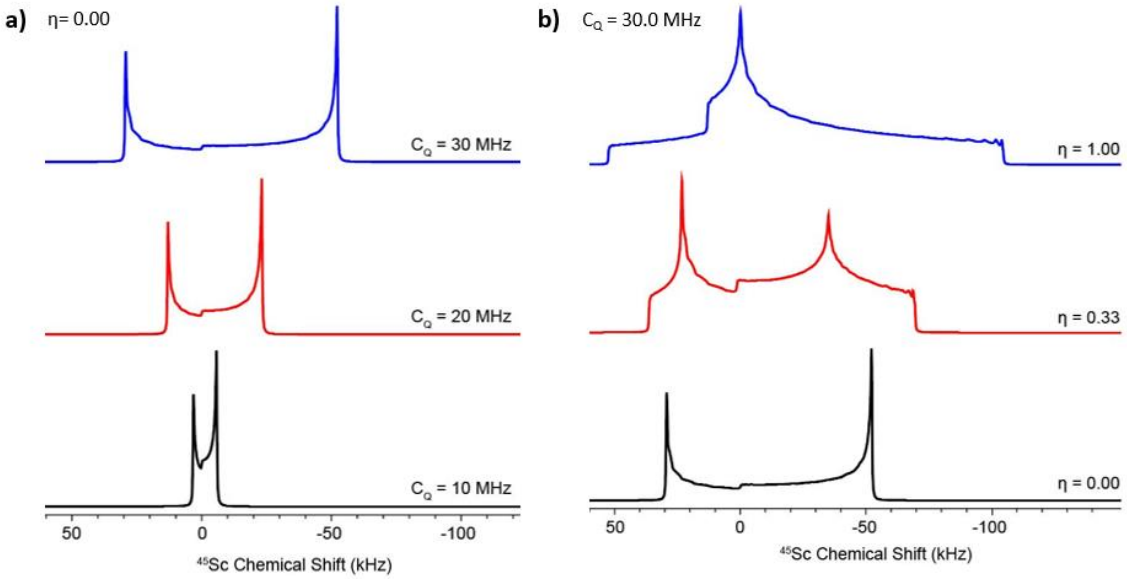

Figure 1.8. Simulated solid-state ^{45}Sc NMR spectra with various values for C_Q and η in TopSpin 4.1.1 when η = 0.00 (a), and C_Q = 30.0 MHz (b).

The occupation of core and valence orbitals determines the nuclear distribution of charge and gives rise to the EFG. An early understanding of the value of C_Q was pioneered by the Townes and Dailey model in 1949, where the EFG results primarily from the occupation of valent p atomic orbitals.[18] They later used this simple model to relate the electronegativity of diatomic molecules containing Cl, Br, and I to the quadrupolar

coupling constant in order to measure the ionicity of chemical bonds in diatomic molecules containing Cl, Br, and I. [19] Since then, advances in computation have allowed for a more accurate description of the EFG tensor by making use of Natural Localized Molecular Orbitals (NLMOs). In this procedure, all atomic interactions in a molecule are transformed into localized orbitals that maximize interactions between two atoms while taking into consideration electron delocalization. This is in contrast to Natural Bond Orbitals (NBOs), which generate orbitals that representative typical Lewis structures and generally localized to 1 or 2 atoms.[20] Under these definitions, a canonical molecular orbital (φ_k^{MO}) can be calculated as the sum of all NLMOs multiple by a transformation matrix T_{jk} that affects the localization criterion.[15] (eq. 7) These equations can be further broken down into their components, similar to the reduction of the canonical MOs into component NLMOs.

$$\varphi_k^{MO} = \sum_j^{NLMO} \phi_j^{NLMO} T_{jk} \qquad (7)$$

Since the EFG is a property of all electronic interactions, the total EFG tensor can be calculated by considering the interaction of the electronic and nuclear contributions of an atom A with nearby NLMOs eq. 8. The equation computes V_{ii} (ii = 11, 22, 33), and the combination of these three principal axes forms the EFG tensor. In this equation, $\langle \chi_r | \hat{V}_{ii} | \chi_s \rangle$ represents the individual electronic and nuclear contributions of the atomic orbitals in atom A, and C_{rk}^* transforms these contributions from the AOs into a mixed AO-MO representation.[15] These equations provide a more accurate description of the EFG tensor, and also take into the account nuclear core contributions to the EFG.

$$V_{ii}^A = \sum_{k,r,s}^{NLMO} \langle \chi_r | \hat{V}_{ii} | \chi_s \rangle \, C_{rk}^* \varphi_k^{MO} \qquad (8)$$

The occupation of empty orbitals affects V_{33} and therefore also affects the C_Q. As seen in Figure 1.9, the three-coordinate $AlMes_3$ contains an empty p_z orbital on aluminum and has a C_Q of 48.2 MHz.[21] However, in $Al(NTMS_2)_3$, the additional N → Al interaction results in a partial occupation of the p_z orbital. The occupation of empty orbitals affecting V_{33} increases the symmetry of the complex and as a result decreases the ^{27}Al C_Q.

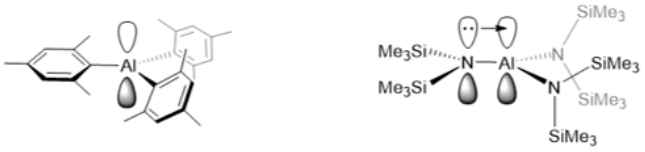

$AlMes_3$
C_Q = 48.2 MHz

$Al(NTMS_2)_3$
C_Q = 36.3 MHz

Figure 1.9. A schematic of the Al p_z orbital in and $AlMes_3$ and $Al(NTMS_2)_3$.

The effect of symmetry on C_Q was important to gaining structural information about Schwartz's reagent, Cp_2ZrHCl, which was known since the 1970s and used in a variety of chemical transformations including hydrogenation, hydrogenation, and other carbon-carbon bond formation reactions.[22-24] Despite its synthetic relevance, no X-ray diffraction structure was reported. In 2009, Rossini and coworkers recorded the solid-state ^{35}Cl NMR of Group IV metal chlorides.[25] Their studies revealed that $Cp_2ZrClCH_3$ has a C_Q of 13.7 MHz, but Cp_2ZrHCl has a C_Q of 19.7 MHz. (Figure 1.10) Given that these compounds are very similar, that they have different C_Q values suggests that Cp_2ZrHCl has a have different crystal structure than the monomeric $Cp_2ZrClCH_3$. The C_Q value was also different than that of Cp^*ZrCl_3, which forms clusters and contains multiple sites with C_Q values between 13-15 MHz. Zirconocene hydrides are also known to form bridging complexes[26], and the IR spectra of Cp_2ZrHCl suggests the presence of bridging hydrides.[29]

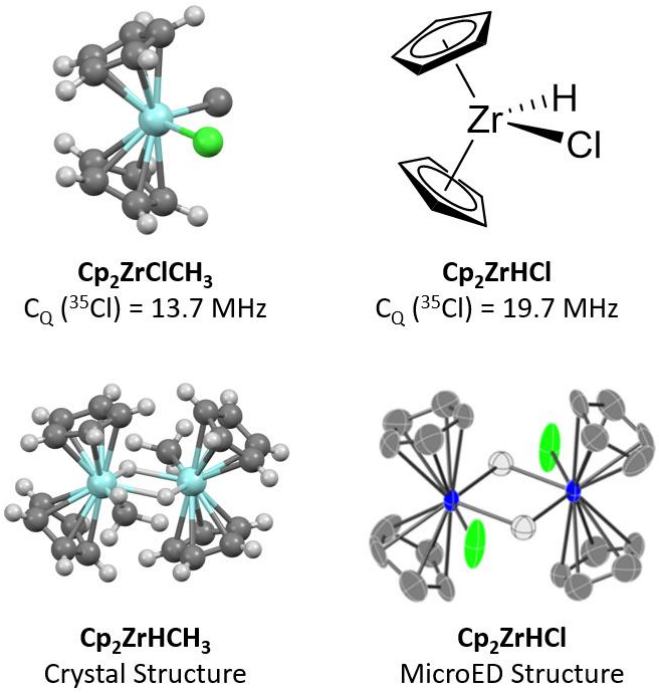

Figure 1.10. C_Q values for $Cp_2ZrMeCl$ and Cp_2ZrHCl. Crystal structure for $Cp_2ZrClCH_3$, Cp_2ZrHMe and MicroED structure for Cp_2ZrHCl, reproduced with permission from ACS.[30c] The hydrogens on the methyl group were not resolved because of disorder.[31]

The related compound Cp_2ZrHCH_3 was studied by Barron and coworkers in 1997, and the X-ray diffraction structure reveals the dimeric structure $[Cp_2ZrCH_3(\mu\text{-}H)]_2$.[32] Using this crystal structure as a starting point, replacing the methyl with chloride, and setting the Zr-Cl bond length to 2.46 Å based on terminal Zr-Cl bond lengths resulted in a C_Q value of 18.9 and 21.1 MHz, which match the values obtained in experiment. The powder X-ray diffraction experiments and simulations of Cp_2ZrHCl and $[Cp_2ZrCH_3(\mu\text{-}H)]_2$ are extremely close and suggest a similar crystal structure, space group, and unit cell parameter for Cp_2ZrHCl. Gratifyingly, the development of microcrystal electron diffraction (MicroED) in 2019 later confirmed the bridging structure.[30]

1.4 Visualization of the CST and EFG Tensors:

The CST and EFG tensors described in Section 1.2 and 1.3 may be calculated with computational chemistry software such as TURBOMOLE, ORCA, Gaussian, and Amsterdam Density Functional (ADF).[33-36] The NLMO analysis of these tensors to gain a molecular orbital understanding of bonding was implemented in ADF in 2009. The computational NLMO analysis of the CST and EFG tensor in conjunction with experimental multinuclear solid-state NMR experiments provides a thorough analysis of structure and bonding for all structures.

The CST and EFG tensors that are responsible for solid-state NMR line shapes are visualized when the tensors are plotted in computational software. A useful characteristic of the tensor is the orientation of each axis. For the CST, the orientation of σ_{11} is often the most important, since it is responsible for nuclear deshielding. For the EFG tensor, V_{33} is important because it determines the value of C_Q. Figure 1.2 and 1.7 depicted the EFG and CST as ellipsoids, and the size is determined by the magnitude of each principal axis. A better representation of these rank-2 tensors is via a spherical polar plot. Mathematica is the common software to obtain these plots, and examples of two popular styles are shown in Figure 1.11.[37-38] Spherical polar plots offer the advantage that information regarding the skew in CST and the asymmetry in EFGs can also be described without loss of information regarding the principal axis system.

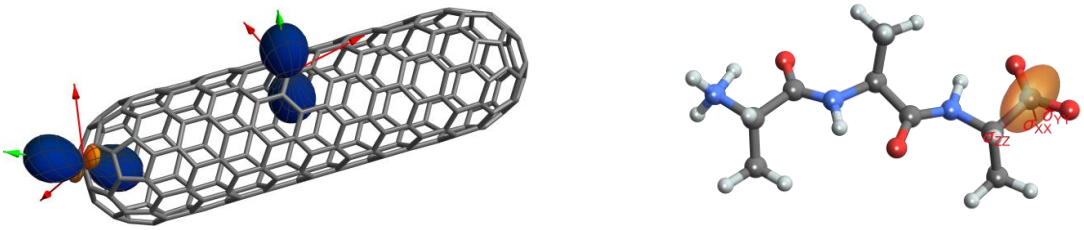

Figure 1.11. Example rank-2 tensors of a carbon nanotube (left) and alanine (right) generated via ref. 37-38.

1.5 Objective of the Dissertation

The objective of the dissertation is to show that multinuclear solid-state NMR spectroscopy with the support of computational chemistry is a valuable technique in elucidating chemical structure. The analysis of the CST and EFG tensors allow for an understanding of shielding and electron distribution, respectively, around a nucleus. The calculation of NMR parameters allows for a molecular orbital understanding of the CST and EFG tensors, which in turn provide information regarding chemical structure.

Chapter 2 introduces the application of multinuclear solid-state NMR to Cp^*_2Sc-R (R = Me, Ph, Et) in the elucidation of structure for Cp^*_2Sc-Et. Chapter 3 explores solid-state ^{45}Sc NMR and the application of C_Q towards understanding the bonding environment around scandium for the related Cp^*_2Sc-X (X = F, Cl, Br, I) compounds and their base-coordinated adducts Cp^*_2Sc-X(THF). Chapter 4 builds upon Chapter 2-3 by relating molecular Cp^*_2Sc-OR (R = CMe_2CF_3, $CMe(CF_3)_2$, $C(CF_3)_3$, $SiPh_3$) to Cp^*_2Sc-sites supported by partially dehydroxylated silica. The theme of exploring secondary interactions after these family of scandocenes continues with a discussion of the EFG

tensor in a series of tri-coordinate boron complexes in Chapter 5 for coinage metal complexes of a diboraanthracene ligand.

Chapter 6 is dedicated to understanding the origin of the ^{29}Si NMR chemical shift and its relation towards the formation of silylium ions. These concepts are used to understand the surface silicon species supported on solid oxides in silica, Lewis acid activated silica, and sulfated zirconia. Chapter 7 presents the thermolysis of $Al(OR^F)_3$ activated silica to form a strong heterogeneous aluminum Lewis acid on silica and its reaction with Cp_2ZrMe_2 to access Lewis acidic zirconium cations.

1.6 References

[1] H. Günther, NMR spectroscopy: basic principles, concepts, and applications in chemistry, 2nd ed., Wiley, Chichester; New York, 1995.

[2] Widdifield, C. M.; Schurko, R. W. *Conc. Mag. Res. Part A.* **2009**. *34(2)*, 91-123.

[3] Laws, D. D.; Bitter, H. L.; Jerschow, A. *Angew. Chem. Int. Ed.* **2002**, *41*, 3096-3129.

[4] a) Ramsey, N. F. *Phys. Rev.* **1950**. *78(6)*, 699-703.
b) Lau, E. Y. and Gerig, J. T. *J. Chem. Phys.* **1995**, *103*, 3341-3349.

[5] Bourissou, D.; Guerret, O.; Gabbai, F. P.; Bertrand, G. *Chem. Rev.* **2000**, *100 (1)*, 39-92.

[6] Huynh, H. V.; *Chem. Rev.* **2018**, *118*, 9457-9492.

[7] Arduengo, A. J.; Dixon, D. A.; Kumashiro, K. K.; Lee, C.; Power, W. P.; Zilm, K. W. *J. Am. Chem. Soc.* **1994**, *116*, 6361-6367.

[8] Tapu, D.; Dixon, D. A.; Roe, C. *Chem. Rev.* **2009**, *109*, 3385-3407.

[9] Ejchart, A *Org. Magn. Res.* **1977**, 9(6), 351-354.

[10] Gordon, C. P.; Yamamoto, K.; Searles, K.; Shirase, S.; Andersen, R. A.; Eisenstein, O.; Coperet, C. *Chem. Sci.* **2018**, *9*, 1912-1918.

[11] Arduengo, A. J.; Harlow, R. L.; Kline, M. *J. Am. Chem. Soc.* **1991**, *113*, 361-363.

[12] W. von E. Doering, A. K. Hoffmann,J. Am. Chem. Soc.1954,76, 6162 – 6165

[13] Rouschias, G.; Shaw, B. L. *J. Chem. Soc. D*, **1970**, 183.

[14] L. Chugaev, M. Skanavy Grigorieva, and A. Posniak, 2. *Anorg. Chem.*, **1925**, *148*, 37.

[15] Autschbach, J.; Zheng, S.; Schurko, R. W. *Concepts Magn. Reson., Part A,* **2010**, *36A*, 84-126.

[16] Stone, N. J. *Atomic Data and Nuclear Data Tables*, **2016**, *111-112*, 1-28.

[17] Pake, G. E. *J. Chem. Phys.* **1948**, *16*, 327-336.

[18] Townes, C. H.; Dailey, B. P. *J. Chem. Phys.* **1949**, *17(9)*, 782-796.

[19] Dailey, B. P.; Townes, C. H. *J. Chem. Phys.*, **1955**, *23(1)*, 118-123.

[20] Glendening, E. D.; Landis, C. R.; Weinhold, F. *Wiley interdisciplinary reviews: computational molecular science*. **2012**, *2(1)*, 1-42.

[21] Tang, J. A.; Masuda, J. D.; Boyle, T. J.; Schurko, R. W. *ChemPhysChem.* **2006**, *7*, 117-130.

[22] Schwartz, J.; Labinger, J. A. *Angew. Chem., Int. Ed. Engl.* **1976**, *15*, 333–340

[23] Hart, D. W.; Schwartz, J. *J. Am. Chem. Soc.* **1974**, *96*, 8115–8116

[24] Wipf, P.; Nunes, R. L. *Tetrahedron* **2004**, *60*, 1269–1279.

[25] Rossini, A. J.; Mills, R. W.; Briscoe, G. A.; Norton, E. L.; Gaeir, S. J.; Hung, I.; Zheng, S.; Autschbach, J.; Schurko, R. W. *J. Am. Chem. Soc.* **2009**, *131*, 3317-3330.

[26] James, B. D.; Nanda, R. K..; Wallbridge, M. G. H. *Inorg. Chem.* **1967**, *11(6)*, 1979-1983.

[27] Jones, S. B.; Petersen, J. L. *Inorg. Chem.* **1981**, *20*, 2889-2894.

[28] Erker, G.; Kropp, K. Atwood, J. L.; Hunter, W. E.; *Organometallics*, **1983**, *2*, 1555-1561.

[29] Wailes, P. C.; Weigold, H. *J. Organomet. Chem.* **1970**, *24*, 405-411.

[30] **a)** Jones, C. G.; Asay, M.; Kim, L. J.; Kleinsasser, J. F.; Saha, A.; Fulton, T. J.; Berkley, K. R.; Cascio, D.; Malyutin, A. G.; Conley, M. P.; Stoltz, B. M.; Lavallo, V.; Rodriguez, J. A.; Nelson, H. M. *ACS Cent. Sci.* **2019**, *5*, 1507-1513. **b)** https://pubs.acs.org/doi/10.1021/acscentsci.9b00403 c) MicroED structure reproduced with permission. Further permissions for reproduction must be directed to ACS.

[31] Hunter, W. E.; Hrncir, D. C.; Bynum, R. V.; Penttila, R. A.; Atwood, J. L. *Organometallics*, **1983**, *2(6)*, 750-755.

[32] Harlan, C. J.; Bott, S. G.; Barron, A. R. *J. Chem. Soc., Dalton Trans.*, **1997**, 637-641.

[33] Balasubramani, S. G.; Chen, G. P.; Coriani, S.; Diedenhofen, M.; Frank, M. S.; Franzke, Y. J.; Furche, F.; Grotjahn, R.; Harding, M. E.; Hattig, C.; Hellweg, A.; Helmich-Paris, B.; Holzer, C.; Huniar, U.; Kaupp, M.; Khah, A. M.; Khani, S. K.; Muller, T.; Mack, F.; Nguyen, B. D.; Parker, S. M.; Perlt, E; Rappoport, D.; Reiter, K.; Roy, S.; Ruckert, M.; Schmitz, G.; Sierka, M.; Tapavicza, E.; Tew, D. P.; van Wullen, C.; Voora, V. K.; Weigend, F.; Wodynski, A.; Yu, J. M. *J. Chem. Phys.* **2020**, *152*, 184107.

[34] Neese, F.; *Wiley Interdisciplinary Reviews: Computational Molecular Science*, **2012**, *2(1)*, 73-78.

[35] Gaussian 16, Revision C.01, Frisch, M. J.; Trucks, G. W.; Schlegel, H. B.; Scuseria, G. E.; Robb, M. A.; Cheeseman, J. R.; Scalmani, G.; Barone, V.; Petersson, G. A.; Nakatsuji, H.; Li, X.; Caricato, M.; Marenich, A. V.; Bloino, J.; Janesko, B. G.; Gomperts, R.; Mennucci, B.; Hratchian, H. P.; Ortiz, J. V.; Izmaylov, A. F.; Sonnenberg, J. L.; Williams-Young, D.; Ding, F.; Lipparini, F.; Egidi, F.; Goings, J.; Peng, B.; Petrone, A.; Henderson, T.; Ranasinghe, D.; Zakrzewski, V. G.; Gao, J.; Rega, N.; Zheng, G.; Liang, W.; Hada, M.; Ehara, M.; Toyota, K.; Fukuda, R.; Hasegawa, J.; Ishida, M.; Nakajima, T.; Honda, Y.; Kitao, O.; Nakai, H.; Vreven, T.; Throssell, K.;

Montgomery, J. A., Jr.; Peralta, J. E.; Ogliaro, F.; Bearpark, M. J.; Heyd, J. J.; Brothers, E. N.; Kudin, K. N.; Staroverov, V. N.; Keith, T. A.; Kobayashi, R.; Normand, J.; Raghavachari, K.; Rendell, A. P.; Burant, J. C.; Iyengar, S. S.; Tomasi, J.; Cossi, M.; Millam, J. M.; Klene, M.; Adamo, C.; Cammi, R.; Ochterski, J. W.; Martin, R. L.; Morokuma, K.; Farkas, O.; Foresman, J. B.; Fox, D. J. Gaussian, Inc., Wallingford CT, 2016.

[36] te Velde, G.; Bickelhaupt, F. M.; Baerends, E. J.; Guerra, C. F.; van Gisbergen, S. J. A.; Snijders, J. G.; Ziegler, T. *J. Comp. Chem.* **2001**, *22*, 931.

[37] Zurek, E.; Pickard, C.; Autschbach, J. *J. Phys. Chem. C* **2008**, *112*, 11744-11750.

[38] Young, R. P.; Lewis, C. R.; Yang, C.; Wang, Y. L.; Harper, J. K.; Mueller, L. J. *Magn. Res.Chem.* **2019**, *57*, 211-223.

CHAPTER 2

The Beta-Agostic Structure in $(C_5Me_5)_2ScCH_2CH_3$ – Solid-State NMR Studies of $(C_5Me_5)_2Sc$-R (R = Me, Ph, Et)

2.1 Abstract:

Solid-state ^{45}Sc NMR studies of Cp^*_2Sc-R ($Cp^* = C_5Me_5$, R = Me, Ph, Et) and density functional (DFT) calculations show that the quadrupolar coupling constants (C_Q) in this series of permethylscandocene hydrocarbyls follow the trend Ph ≈ Me > Et. This indicates that the bonding interaction in Sc-R for R = Ph, Me are similar but is different for Sc-Et. The solid-state ^{13}C NMR studies and DFT calculations of Cp^*_2Sc-Et reveals that there is an additional β-agostic CH interaction with scandium that is not present for Cp^*_2Sc-R for R = Ph, Me. An analysis of the chemical shielding tensor shows that this additional interaction is deshielding from the coupling of the occupied σ(C-C) orbital to the unoccupied $\pi^*(Sc\ldots HC_\beta)$ orbital.

2.2 Introduction:

The activation of C-H bonds by transition metals is important in the catalytic cycles of hydrocarbon polymerizations and organic molecule derivatization. While the C-H bonds of ligands are generally considered chemically inert, early crystal structures of some complexes reported by Brookhart, Green, and references therein provide evidence for a C-H bond interacting with a metal center.[1-3] (Figure 2.1) Brookhart and Green coined the term "agostic" to describe situations where a hydrogen is simultaneously interacting with carbon and a transition metal atom. These interactions feature an acute M…H-C bond angle, a

close M…H interaction smaller than the sum of their van der Waal radii, and a three-center two-electron bonding interaction between M…H-C.

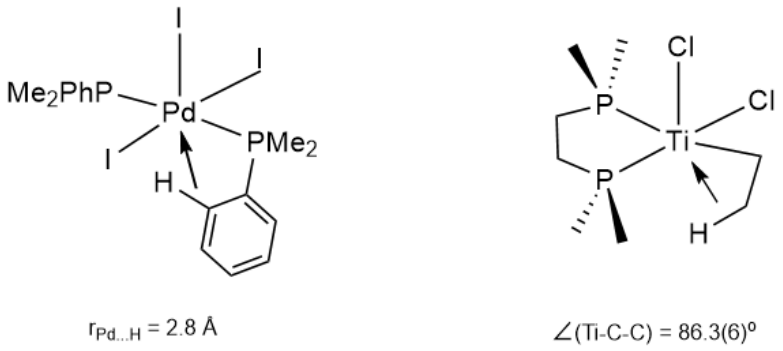

Figure 2.1. Example of C-H agostic interactions characterized by small M-C-C angles and short M…H distances, where M is a metal.

Agostic interactions are proposed to be responsible for stereoselective olefin insertion reactions and for stabilizing a *syn*-alkylidene complex over its *anti*- isomer. [4,5] In 1987, Bercaw and coworkers prepared a series of Cp^*_2Sc-R compounds, including but not limited to R = Cl, I, Me, Et, Pr, Ph towards the goal of understanding the mechanism for transition metal C-H bond activation.[6] Of these compounds, Cp^*_2Sc-Et was unusual in that although the crystal structure was highly disordered, the carbons of the ethyl group were equidistant from scandium. (Figure 2.2)

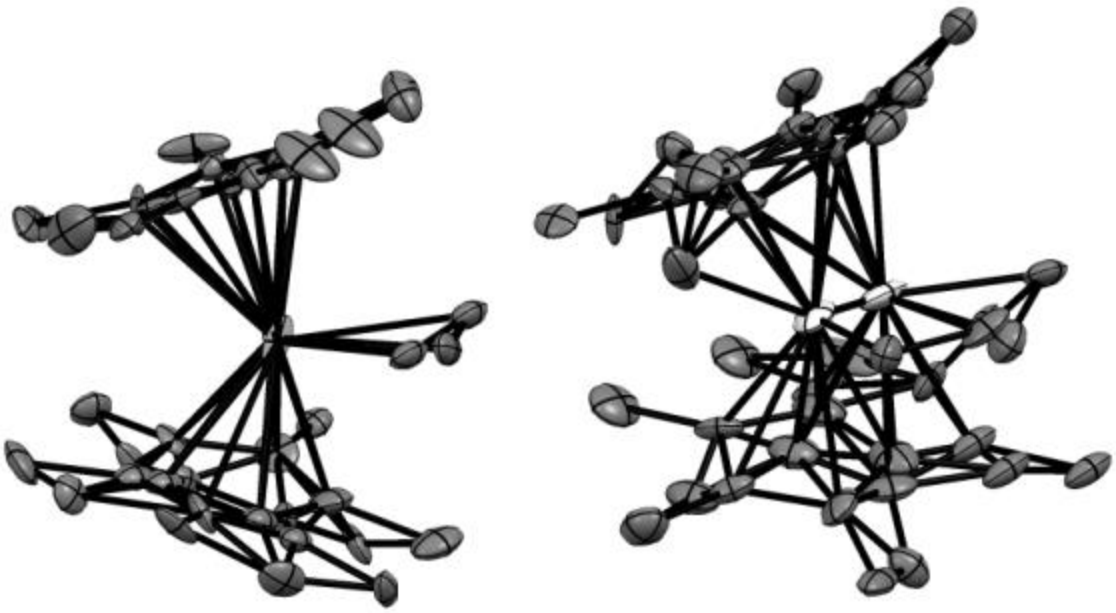

Figure 2.2. X-ray crystal structure of Cp^*_2Sc-Et. Two independent sites are present in the unit cell, both of which are highly disordered.

Table 2.1. Kinetic studies of ethylene oligomerization from ref. 7.

Species	Rate of ethylene insertion
Cp^*_2Sc-CH_3	8.1(2) x 10^{-4}
Cp*2Sc-CH_2CH_3	4.4(2) x 10^{-4}
Cp*2Sc-$CH_2CH_2CH_3$	6.1(2) x 10^{-3}

Three years later in 1990, Bercaw and coworkers conducted kinetic studies via ethylene insertion for Cp^*_2Sc-R (R = Me, Et, Pr), and their results show that the rates decrease from Me > Pr > Et.[7](Table 2.1) The rates are attributed to that for Cp^*_2Sc-Et, a β-CH agostic is electronically favorable, but for Cp^*_2Sc-Pr a β-CH agostic is electronically favorable but would be sterically unfavorable because of steric interactions with the Cp* rings. Their crystal structure, infrared spectroscopy and kinetics experiment data suggest that Cp^*_2Sc-Et contains β-CH agostic interaction, but their ^1H and ^{13}C NMR data do not unambiguously identify a β-CH agostic interaction for Cp^*_2Sc-Et. In particular, the crystal structure that they obtained exhibited disorder. (Figure 2.2)

In 2015, a similar complex Cp^*_2Y-Et was prepared and isolated by Evans et al.[8] The crystal structure of Cp^*_2Y-Et is unambiguous and features a β-CH agostic interaction with an acute M…H-C angle and a M…H distance that is smaller than the sum of their van der Waal radii. The IR spectra for Cp^*_2Y-Et has three noticeably low frequency ν(C-H) bands between 2400-2600 cm^{-1}, which is significantly lower than the 2900-3100 cm^{-1} that is expected for CH_2 and CH_3 groups. However, these stretching frequencies are consistent with those reported by Bercaw et al., further suggesting that Cp^*_2Sc-Et contains a β-CH agostic interaction.

This chapter revisits the structure of Cp^*_2Sc-Et from an NMR perspective and explores a combined solid-state NMR and density functional theory approach to elucidating the β-CH agostic interaction in Cp^*_2Sc-Et. A comparison of ^{45}Sc C_Q in Cp^*_2Sc-R (R = Me, Et, Ph) is presented to further emphasize the difference in coordination environment between Cp^*_2Sc-Et and Cp^*_2Sc-R (R=Me, Ph). The crystal structure and

solid-state ^{45}Sc NMR spectra are reported for each compound. For Cp*$_2$Sc-Et, the solid-state ^{13}C NMR spectra were recorded, and a thorough analysis of the chemical shielding tensor via DFT unambiguously assigns the β-CH agostic interaction in Cp*$_2$Sc-Et.

2.3 Results and Discussion

The room temperature static solid-state ^{45}Sc NMR spectra recorded at 14.1T for Cp*$_2$Sc-R (R = Me, Ph, Et) are shown above in Figure 2.3. The bonding environment around scandium for Cp*$_2$Sc-R (R = Me, Ph) are expected to be similar, where R is solely a σ-donor ligand with no additional π-donation or secondary interactions. As a result, the C_Q's for both should be similar. Indeed, the solid-state ^{45}Sc NMR spectra are consistent with this expectation, and their C_Q's are 36.2(1) MHz for Cp*$_2$Sc-Me and 38.6(1) MHz for Cp*$_2$Sc-Ph. In contrast, the room temperature solid-state ^{45}Sc NMR spectra of Cp*$_2$Sc-Et spectra is narrower and weaker. Triple quantum MAS (3QMAS) experiments for Cp*$_2$Sc-Et reveal three distinct Sc sites, which is consistent with the disordered crystal structure. (Figure 2.4) However, the C_Q of these sites are between 9.5-12.0 MHz, which is inconsistent with the DFT results of 28.2 MHz. (Table 2.3, page 27)

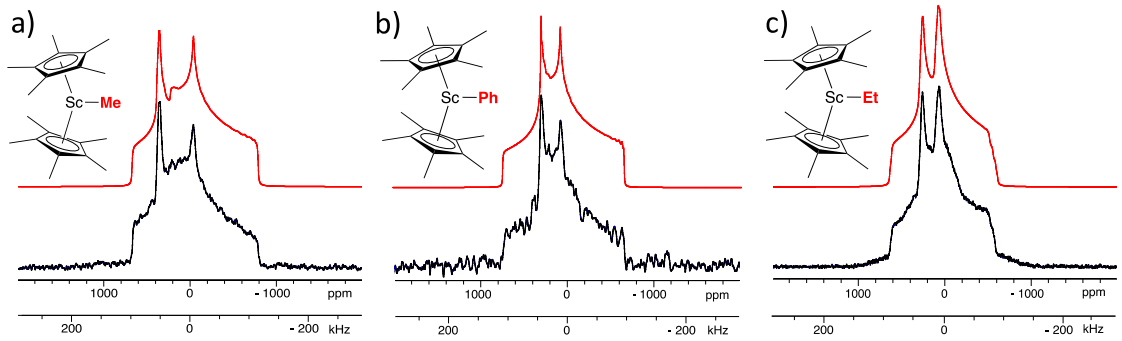

Figure 2.3. Room temperature static ^{45}Sc{1H} NMR of Cp*$_2$Sc-Me (a) and Cp*$_2$Sc-Ph (b). Static ^{45}Sc{^{1}H} NMR spectra of Cp*2Sc-Et recorded at 170K. Experimental spectra are in black, and simulations are shown in red. All spectra were recorded at 14.1 T.

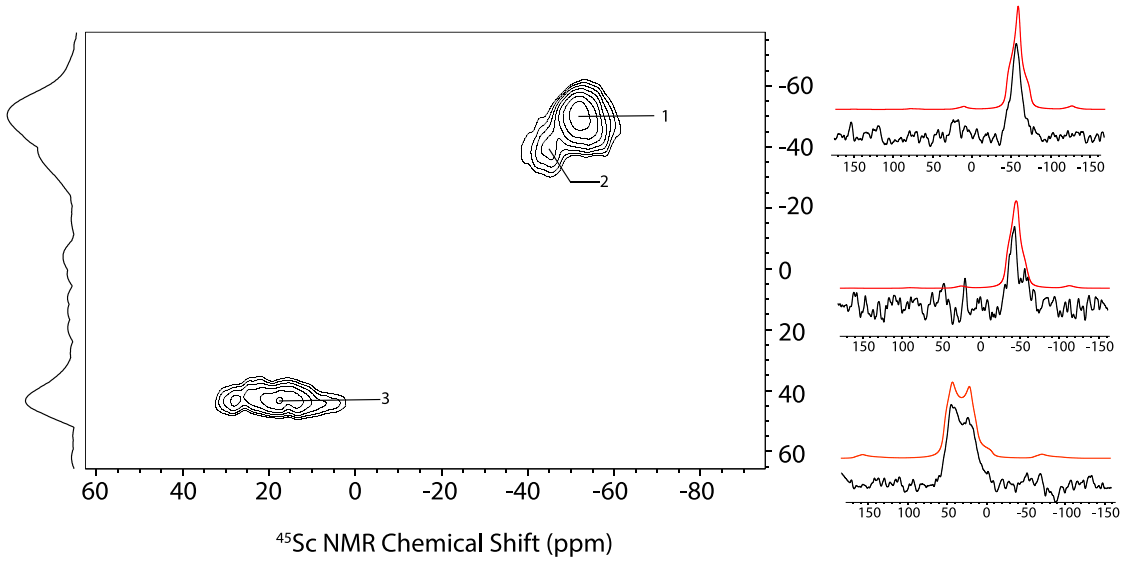

Figure 2.4. 3QMAS ^{45}Sc{^{1}H} NMR spectrum of Cp$^*_2$ScEt at 10 kHz and 0 ^{o}C, 14.1 T. 3QMAS spectrum of Cp*$_2$Sc–Et and extracted slices for contour 1 (top), contour 2 (middle) and contour 3 (bottom). Experimental spectra are shown in black, and simulated spectra are shown in red.

Because the crystal structure of Cp*$_2$Sc-Et is highly disordered, slowing down the molecular dynamics by cooling may result in a spectra that is consistent with typical quadrupolar powder patterns. The solid-state ^{45}Sc spectrum of Cp*$_2$Sc-Et was collected

again at 170K, and at this temperature, the dynamics are suppressed and reveal a noticeably smaller C_Q of 30.1 MHz. The reduced ^{45}Sc C_Q value for Cp^*_2Sc-Et compared to Cp^*_2ScMe and Cp^*_2Sc-Ph indicate that the ethyl fragment is contributing more electron density to scandium that a normal σ-donor ligand that is expected for methyl and phenyl ligands.

The ^{13}C CPMAS spectra of Cp^*_2Sc-Et was also recorded (Figure 2.5-2.7), and the spectra was simulated to extrapolate the CST. (Table 2.2) The simulated spectra reveal a narrow span for the $C_5\mathbf{Me}_5$ (Cp*) ligand but a large span for C_α and C_β. The narrow span of 8ppm on $C_5\mathbf{Me}_5$ is attributed to the low degree of overlap between the methyl C-H bonds with each other and the C-C_{ring} bond.[9] In contrast, the span is large for C_α (Ω = 78ppm) because of the anisotropy created by the σ(Sc-C) bond and is consistent with Cp^*_2Ti-($\mathbf{C}H_3)_2$ (Ω = 78ppm).[10] The span of C_β which could be considered a C-$\mathbf{C}H_3$ is rather large at 39ppm when compared to the $C_5\mathbf{Me}_5$ ring, which suggests that there is likely a secondary interaction between the C_β-H bond and the transition metal center.

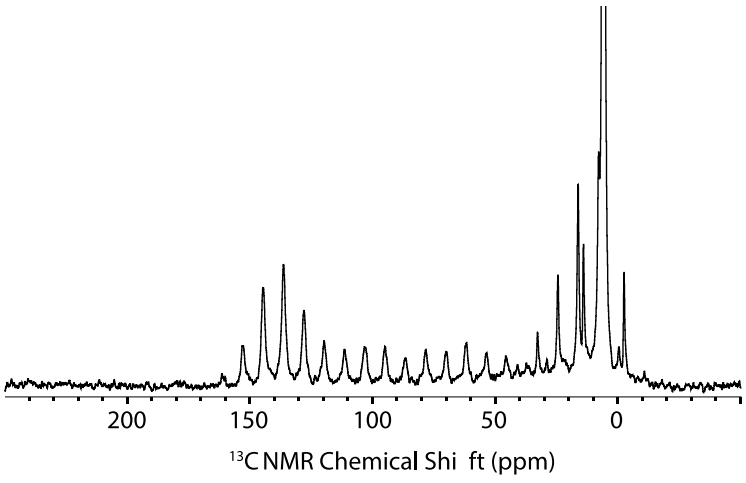

Figure 2.5. $^{13}C\{^1H\}$ CP-MAS NMR spectrum of $Cp^*_2ScCH_2CH_3$ spinning at 1.25 kHz.

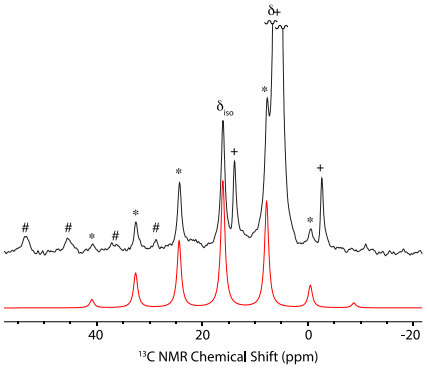

Figure 2.6. ^{13}C solid-state CPMAS spectra of Cp^*_2Sc-Et at 1.25 kHz spinning speed. (δ_{iso} = isotropic chemical shift of Sc-CH_2CH_3; * = spinning side band, # = spinning side band of Cp* carbons; δ+ = isotropic chemical shift of Cp-Me; + = spinning side band of Cp-Me). The experimental spectra is shown in black, and the simulated spectrum for C_β for Sc-CH_2CH_3 is shown in red.

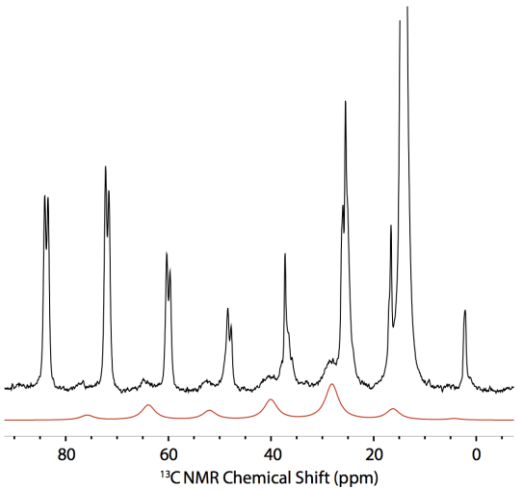

Figure 2.7. ^{13}C CPMAS NMR spectra of Cp^*_2Sc–Et at 1.8 kHz spinning speed. The experimental spectrum is shown in black, and the simulated spectrum for C_α in Sc–CH_2CH_3 is shown in red.

Table 2.2. CSA tensor parameters from the ^{13}C CPMAS spectrum of Cp^*_2Sc-Et.

Carbon	δ_{11}	δ_{22}	δ_{33}	Ω	κ
Sc-**C**H_2CH_3	93	14	14	79	-1.0
Sc-CH_2**C**H_3	42	15	3	39	-0.79
C_5***Me***$_5$	13	10	5	8	0.18

To gain a better understanding of how the ethyl fragment is interacting with scandium, the structure and NMR properties of Cp^*_2Sc-R(Me, Ph, Et) was calculated at the B3LYP-GD3BJ (Sc/6-311G**, C,H/6-31G**) level of theory. The optimized structure for Cp*2Sc-Me and Ph agrees well with the crystal structure, and the C_Q calculations also agree well with experimental values. (Table 2.3) At this level of theory, the C_Q for Cp^*_2Sc-Me is 36.6 MHz, for Cp^*_2Sc-Ph is 36.9 MHz, and for Cp^*_2Sc-Et is 28.2 MHz. The optimized geometry of Cp^*_2Sc-Et contains a short Sc-C_α-C_β angle of 85.6°, a short Sc…H-C_β distance of 2.16Å, and a Sc-C_α-C_β-H dihedral angle of 6°, all of which are consistent with a β-CH agostic interaction.[11]

Table 2.3. C_Q values for Cp^*_2Sc-R (R = Me, Ph, Et). All calculations were performed in Gaussian 09 at the B3LYP-GD3BJ, Sc/6-31++G**, C,H/6-31G** level of theory.

Compound	Experimental C_Q (MHz)	Calculated C_Q (MHz)
Cp^*_2Sc-Me	36.1	36.6
Cp^*_2Sc-Ph	38.6	36.9
Cp^*_2Sc-Et	28.2	28.2

At this same level of theory, the Ω and C_Q vary with the Sc-C_α-C_β angle in Cp*$_2$Sc-Et. Strengthening the β-CH agostic interaction by compressing the angle to 80^o reduces the C_Q to 25.7 MHz and increases the Ω (C_α = 92 ppm; C_β = 55 ppm). In contrast, weakening the β-CH agostic interaction by widening this angle to 95^o increases the C_Q to 31.5 MHz and enlarges the Ω (C_α = 66 ppm; C_β = 25 ppm). (Figure 2.8) The results indicate that both C_Q and Ω are sensitive to the presence of a β-CH agostic interaction, and the agreement between the experimentally recorded solid-state NMR parameters and DFT optimized structures and NMR calculations assign a β-CH agostic interaction for Cp*$_2$Sc-Et.

The NLMO analysis of the ethyl fragment provides insight into the deshielding that is present in C_β. The Natural Chemical Shielding analysis reveals that the major deshielding δ_{11}^{p} for C_β in Cp*$_2$Sc-Et originates from the coupling of the occupied σ(C_α – C_β) and the vacant $\pi^*_{Sc\ldots HC_\beta}$ orbital through the $\widehat{L_{11}}$ operator. (Figure 2.9, page 29) The orientation of the CST is shown in Figure 2.9b, and the consequence of deshielding can primarily be analyzed via δ_{11}. For C_α, the major deshielding arises from the occupied σ(C_α – Sc) coupling to the unoccupied π*(C_α – Sc). (Figure 2.9c) For C_β, the major deshielding couples the σ(C_β –C_α) to π*(Sc…HC_β). (Figure 2.9d) The differences in chemical environments lead to different δ_{iso}(^{13}C) in C_α and C_β that is observed in the ^{13}C CPMAS NMR. These results are consistent with the original assignment of the β-CH agostic structure proposed by Bercaw and co-workers in 1987.

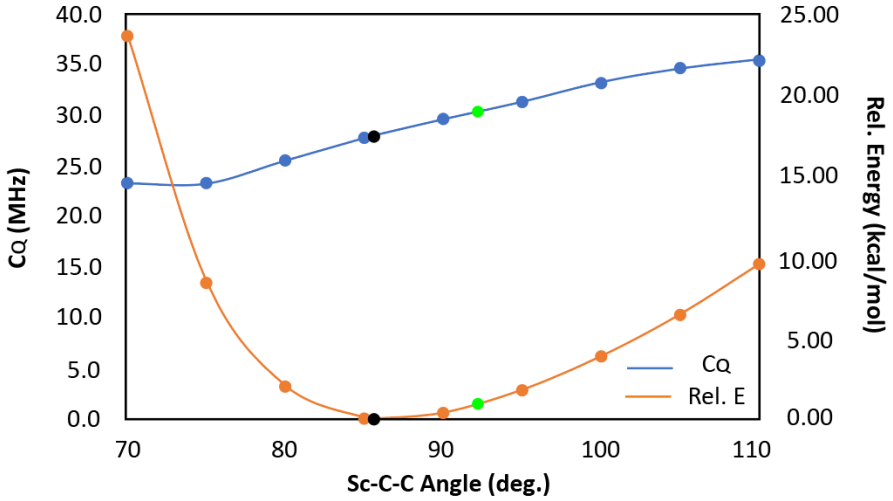

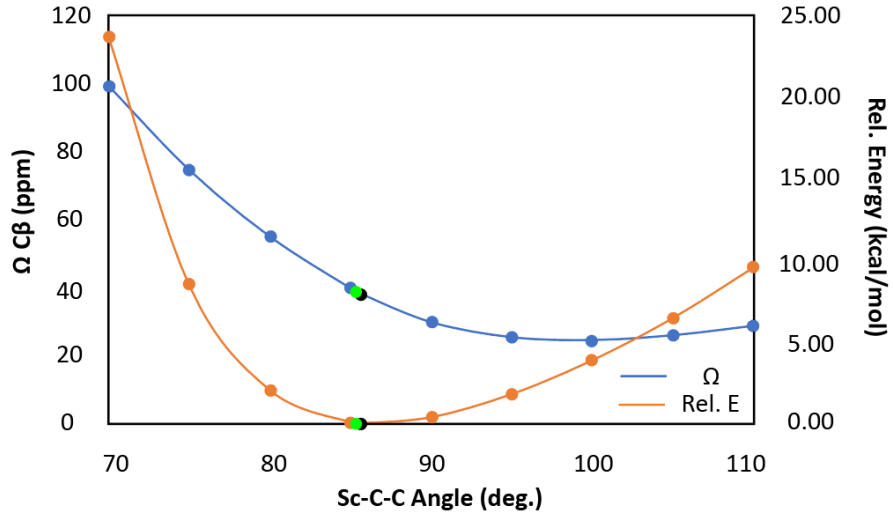

Figure 2.8. Plot of C_Q (top) and span of C_β (bottom) with respect to Sc-C_α-C_β angle and relative SCF energy. C_Q is plotted in absolute value. Black dots indicate optimized geometry and green dots indicate experimental C_Q and span.

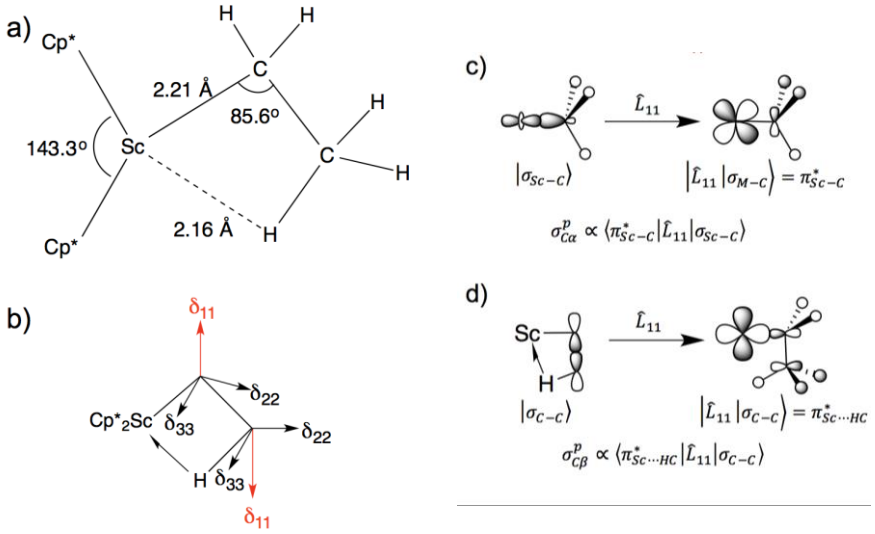

Figure 2.9. Important bond angles and distances for Cp*2Sc-Et from DFT optimization (a). Orientation of the CST for the Sc-CH_2CH_3 fragment (b) and contributions to σ^p from Natural Chemical Shielding analysis for C_α (c) and C_β (d).

2.4 Conclusion

The experimental solid-state ^{45}Sc NMR spectra and computational DFT calculations of Cp*$_2$Sc-R (R = Me, Et, Ph) are in agreement that the C_Q reveals bonding in Cp*$_2$Sc-Me and Cp*$_2$Sc-Ph to be similar, where both methyl and phenyl ligands act as pure σ-donors. In contrast while the ethyl group in Cp*$_2$Sc-Et has a σ-donating interaction with scandium, the ^{45}Sc C_Q and the solid-state ^{13}C CPMAS experiments show that there is an additional β-CH agostic interaction. The experimental observations are supported by DFT calculations which reveal that the origin of this interaction can be found in the coupling of the occupied σ(C_β – C_α) with the vacant $\pi^*_{Sc\ldots HC_\beta}$. Together, the solid-state NMR and DFT calculations in this chapter unambiguously characterize the structure of Cp*$_2$Sc-Et.

Cp^*_2Sc-Et does, in fact, contain a β-CH agostic interaction, as was originally suggested by Bercaw and coworkers in 1987.

2.5 Materials and Methods

The compounds Cp^*_2Sc-R (R = Me, Ph, Et) were synthesized according to literature methods.[6] The solution phase ^{l}H and $^{45}Sc\{^1H\}$ Hahn echo NMR spectra were recorded on an Avance Bruker 300 NMR spectrometer. The spectra are referenced to the NMR solvent residual peak for ^1H and for $^{45}Sc\{^1H\}$ NMR were referenced to an external standard of 0.11 M $ScCl_3$ in 0.1 M aqueous HCl. Solid-state NMR spectra were recorded in 4 mm zirconia rotors on either an Avance III Bruker 400 or Bruker Neo-600 NMR spectrometer. The ^{13}C CPMAS NMR spectra were recorded with a 2 μsec contact time, and a 3 sec relaxation delay. Static $^{45}Sc\{^1H\}$ NMR spectra were recorded with a Hahn-echo pulse sequence, with full echo detection ($\pi/2 - \tau - \pi - acq$).[12-13] Echo delays (τ) were set to 100 μsec. ^{45}Sc triple quantum (3Q-MAS)[3] 2D experiments were recorded using a *z*-filter sequence.[14] At 14.1 T, excitation and reconversion pulse widths were 1.8 and 4.5 ms, with a ν_{RF} = 35 kHz. The central selective $\pi/2$ pulse was ν_{RF} = 7 kHz. The recovery delay in all ^{45}Sc experiments was 0.25 s. During the 3QMAS experiment, the sample was cooled to ca. 0 ^oC to prevent decomposition. NMR spectra were referenced to external TMS (^{13}C) or 0.11 M $ScCl_3$ in 0.1 M aqueous HCl solution (^{45}Sc). All simulations of solid-state NMR spectra were performed in Topspin using the Sola line shape analysis feature.

The chemical shielding tensor (CST) of C_β in $Cp^*_2ScCH_2CH_3$ was calculated with the B3LYP-GD3BJ functional, TZ2P basis set on scandium, and DZ basis set on all other

atoms in ADF,[15-17] using the geometry optimized structure from Gaussian 09. The calculated Ω of 42 ppm for C_β and 84 ppm for C_α is in agreement with experimental span values. The CSTs are plotted in Figure 2.10 and indicate that the largest deshielding component (σ_{11}) is located perpendicular to σ(Sc-C_α) and σ(C_α-C_β). The CSTs were analyzed using NCS analysis in the Bond Orbital 6.0 package in ADF.[18-19] The results are shown in Table 2.4 and contributions to its most deshielded component σ_{11} plotted below in Figure 2.11 (page 33). The results indicate that the spin orbit contribution to $\sigma_{para+so}$ is negligible, so $\sigma_{para+so}$ will be interpreted as σ_{para}. The largest deshielding (σ_{11}) in σ_{para} is from the occupied σ(Sc-C) coupling to vacant π*(Sc-C) in C_α and from occupied σ(C-C) coupling to vacant π*(C-C) in C_β. The isotropic chemical shielding of C_β (181ppm) was also referenced to geometry optimized tetramethylsilane at the appropriate level of theory (202ppm).

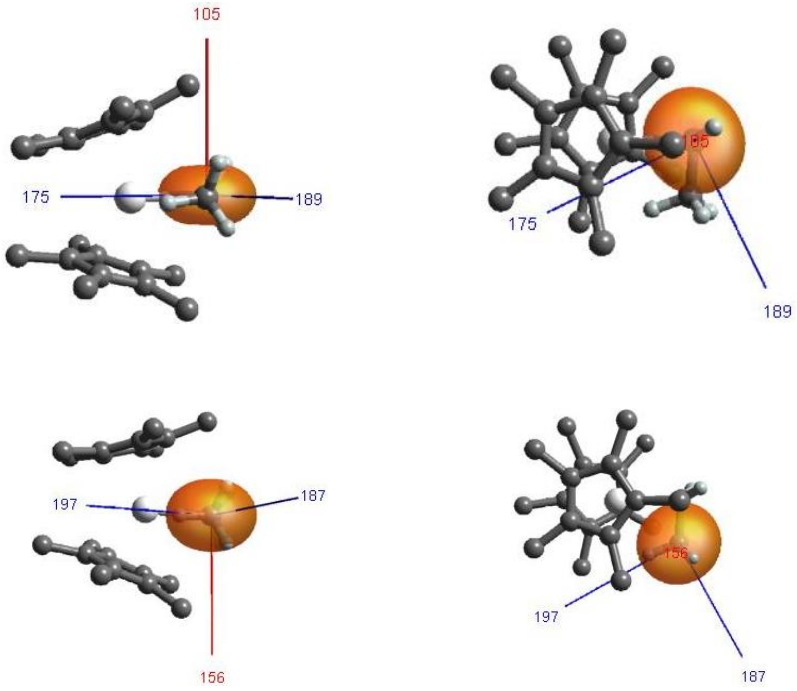

Figure 2.10. Chemical Shielding Tensor of C_{α} (top) C_{β} (bottom) in $Cp^*_2ScC_{\alpha}H_2C_{\beta}H_3$. Both the view along and perpendicular $\sigma(C_{\alpha}\text{-}C_{\beta})$ are shown.

Table 2.4. Natural Localized Molecular Orbital Contributions in $Cp^*_2ScC_\alpha H_2C_\beta H_3$. ^ values in parentheses are SO contributions.

	C_α			C_β		
	σ_{11}	σ_{22}	σ_{33}	σ_{11}	σ_{22}	σ_{33}
σ_{iso}	105	175	189	157	187	199
σ_{dia}	240	247	246	249	259	256
$\sigma_{para+SO}$^	-136 (-1)	-72 (0)	-66 (1)	-93 (1)	-70 (1)	-57 (1)
$\sigma(Sc\text{-}C_\alpha)$	-83	-22	-18	1	-2	1
$\sigma(C_\alpha\text{-}C_\beta)$	-41	-31	1	-55	-14	-10
$\sigma(C_\alpha\text{-}H^1)$	-4	-9	-21	0	0	-4
$\sigma(C_\alpha\text{-}H^2)$	-6	-8	-23	-1	1	-3
$\sigma(C_\beta\text{-}H)$	-3	1	-2	-23	-16	-21
$\sigma(C_\beta\text{-}H')$	-4	0	-2	-16	-23	-24
$\sigma(C_\beta\text{-}H_\beta)$	9	0	0	2	-18	2

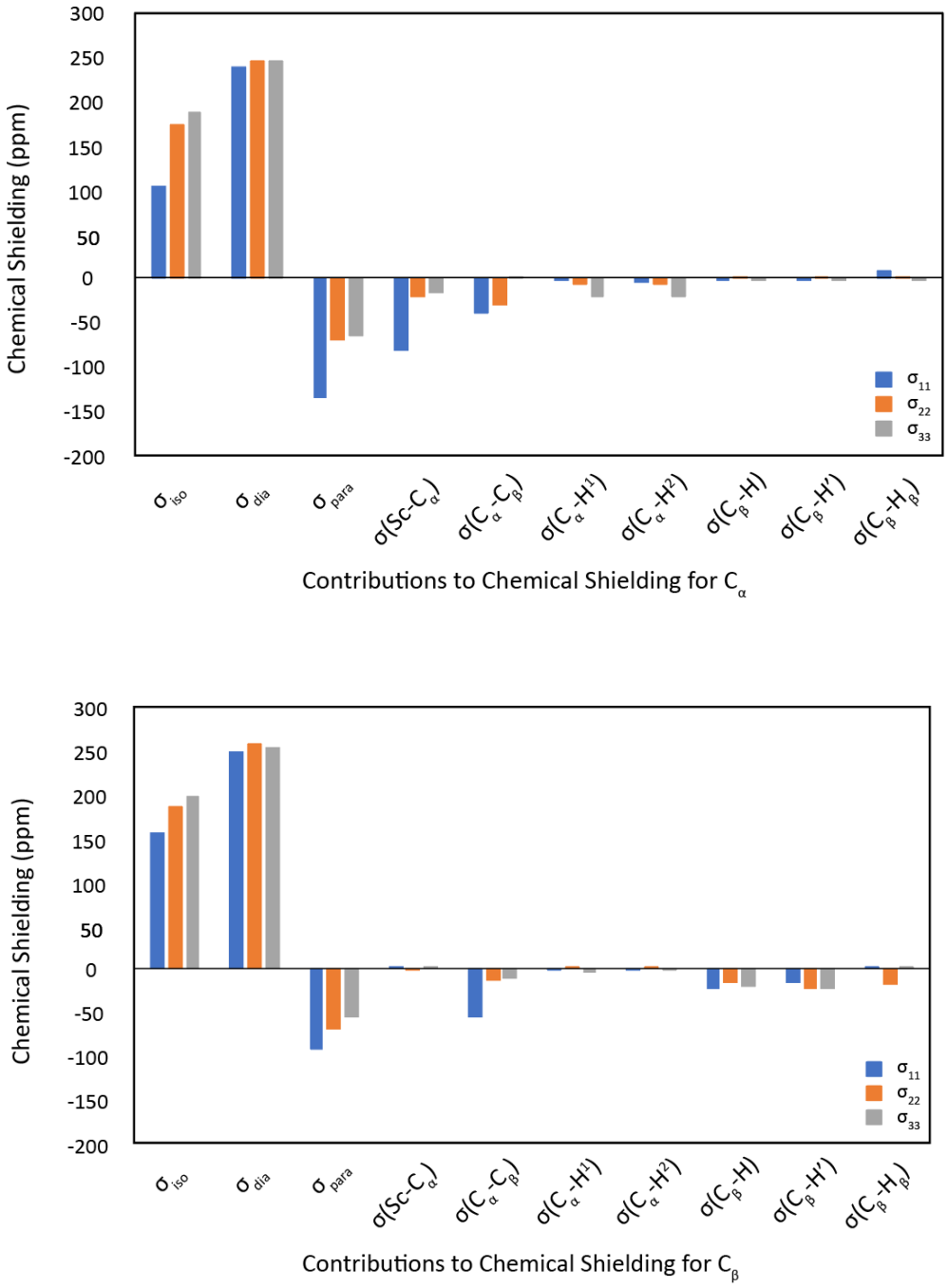

Figure 2.11. Natural Localized Molecular Orbital Contributions for C_{α} (top) and C_{β} (bottom) in $Cp^*_2ScC_{\alpha}H_2C_{\beta}H_3$.

2.6 References

[1] Brookhart, M. and Green, M. L. H. *J. Organomet. Chem.* **1983**, *250*, 395-408.

[2] Dawoodi, Z.; Green, M. L. H.; Prout, K.; Mtetwa, V. S. B.; Williams, J. M.; Schultz, A. J.; Koetzle, T. F. *J. Chem. Soc. Dalt. Trans.* **1986**, 1629-1637.

[3] Bailey, N. A; Jenkins, J. M.; Mason, R.; Shaw, B. L.; *J. Chem. Soc. Chem. Commun.* **1965**, 237.

[4] Grubbs, R. H.; Coates, G. W. *Acc. Chem. Res.* **1996**, *29*, 85-93.

[5] Schrock, R. R. *Chem. Rev.* **2009**, *109*, 3211-3226.

[6] Thompson, M. E.; Baxter, S. M.; Bulls, A. R.; Burger, B. J.; Nolan, M. C.; Santarsiero, B. D.; Schaefer, W. P.; Bercaw, J. E. *J. Am. Chem. Soc.* **1987**, *109*, 203-219.

[7] Burger, B. J.; Thompson, M. E.; Cotter, D. and Bercaw, J. E. *J. Am. Chem. Soc.* **1990**, *112*, 156-1577.

[8] Macdonald, M. R.; Langeslay, R. R. Ziller, J.W. and Evans,W. *J. Am. Chem. Soc.* **2015**, *137*, 14716-14725.

[9] Widdifield, C. M. and Schurko, R. W. *Conc. In Mag. Res. A* **2009**, *34A*, 91-123.

[10] Gordon, C. P.;Yamamoto, K.; Searles, K.; Shirase, S.; Andersen, R. A.; Eisenstein, O.; Coperet, C. *Chem. Sci.* **2018**, *9*, 1912.

[11] Brookhart, M.; Green, M. L. H. and Parkin, G. *PNAS.* **2007**, *104(17)* 6908-6914.

[12] Tang, J. A.; Masuda, J. D.; Boyle, T. J.; Schurko, R. W. *ChemPhysChem* **2006**, *7*, 117-130.

[13] Medek, A.; Harwood, J. S.; Frydman, L. *J. Am. Chem. Soc.*, **1995**, *117*, 12779-12787.

[14] Amoureux, J. P.; Fernandez, C.; Steurnagel, S. *J. Magn. Reson., Ser. A.* **1996**, *123*, 116-118.

[15] G.te Velde, F.M. Bickelhaupt, E.J. Baerends, C. Fonseca Guerra, S.J.A. van Gisbergen, J.G. Snijders and T. Ziegler, Chemistry with ADF, Journal of Computational Chemistry 22, 931 (2001)

[16] C.Fonseca Guerra, J.G. Snijders, G. te Velde and E.J. Baerends, *Theor. Chem. Acc.* **1998**, *99*, 391.

[17] ADF2017, SCM, Theoretical Chemistry, Vrije Universiteit, Amsterdam, The Netherlands, http://www.scm.com.

[18] Autschbach, J.; Zheng, S. *Magn. Res. Chem.* **2008**, *46*, S45.

[19] Autschbach, J. *J. Chem. Phys.* **2008**, *128*, 164112.

CHAPTER 3

Solid-state ^{45}Sc NMR Studies of Cp*$_2$Sc-X and Cp*$_2$ScX(THF)

3.1 Abstract:

Cp*$_2$Sc-X, where X is a halide, were synthesized, and their solid-state ^{45}Sc NMR were studied to determine how the ^{45}Sc quadrupolar coupling constant (C_Q) is affected by the Sc-X bond. The experimental coupling constants decrease from F > Br > Cl > I. The orbitals contributing to the C_Q(^{45}Sc) were also analyzed via DFT and reveal that the C_Q is related to core scandium orbitals, halide orbitals and polarizability, and the Sc-X bond distance. Cp*$_2$Sc-X(THF) were also synthesized and have much smaller C_Q values than Cp*$_2$Sc-X. The decrease in C_Q for the THF adducts is related to the change in structure and additional occupation of orbitals containing π-symmetry.

3.2 Introduction:

Solid-state ^{45}Sc NMR is a powerful technique that can be used to elucidate the bonding environment around scandium. Chapter 1 presented the characterization of Cp*$_2$Sc-R (R = Me, Ph, Et), which had a C_Q(^{45}Sc) trend of Ph ≈ Me > Et. With a combined solid-state ^{13}C NMR and DFT approach, analysis of the chemical shielding tensor allowed for the unambiguous assignment of a β-agostic CH interaction to Cp*$_2$Sc-Et. Formally, the structure of Cp*$_2$Sc-R all contained σ-bonding interactions between scandium and R. Specifically for Cp*2Sc-Et, the β-agostic interaction is a σ(C_β-H) donating into a π-orbital on scandium.[1]

This chapter addresses how the σ- and π-interactions on scandium affect its C_Q. The halides were chosen because previous EPR and UV-Vis studies of Cp^*_2Ti-X revealed that the Ti-X bond affects its spectroscopic properties, which resulted in a π-donor series (F > Cl > Br > I).[2] The C_Q of Cp^*_2Sc-X in this chapter show that the C_Q is mainly affected by the core orbitals on Sc and X as well as the σ(Sc-X) bond. The π-orbitals, in contrast, contribute only a minor amount to the C_Q. The addition of THF to Cp^*_2Sc-X results in the THF molecule occupying the LUMO at Cp*2Sc-X, which leads to a change in geometry at scandium. Consequently, the C_Q for Cp^*_2Sc-X(THF) are significantly smaller.

3.3 Results and Discussion

The synthesis of Cp^*_2Sc-X (X = Br, I) can be achieved via salt metathesis with Cp^*_2Sc-Cl[1] and LiX in toluene at 80 °C. (Scheme 3.1, page X) However, Cp^*_2Sc-F could not be prepared with salt metathesis with LiF or AgF. The reaction of Cp^*_2Sc-Cl with $[NMe_4][F]$ also led to intractable mixtures. However, Cp^*_2Sc-F can be prepared via the reaction of vinyl fluoride into Cp^*_2Sc-Me, releasing propylene and forming Cp^*_2Sc-F. This reaction likely proceeds via the insertion of vinyl fluoride into the Sc-Me bond, followed by β-F elimination, which is common in transition metal alkyl compounds.[4]

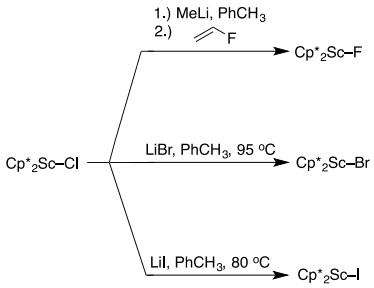

Scheme 3.1. Synthesis of Cp^*_2Sc–X.

The crystal structures of these compounds are shown in Figure 3.1, and these compounds crystallize with only one molecule per unit cell other than for Cp^*_2Sc-Cl, which crystallizes with four nearly identical molecules per unit cell. The structures of Cp^*_2Sc-X exhibit bent C_{2v} structures that are typical of d^0 metallocenes. The Sc-X bond lengths increase from F < Cl < Br < I, which is expected since the sum of the van der Waal radii also increase in that order (Table 3.1). The solid-state NMR spectra of Cp^*_2Sc-X exhibit broad powder patterns with a C_Q similar to those of Cp^*_2Sc-R (R = Me, Et, Ph). (Figure 3.2, Table 3.2).

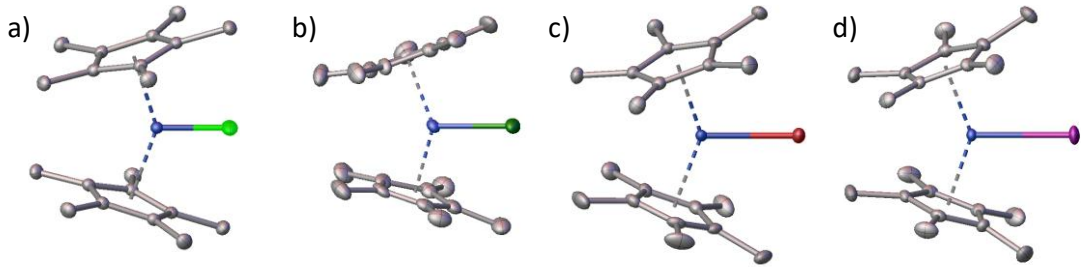

Figure 3.1. X-ray crystal structures of Cp^*_2Sc-F (a), Cp^*_2Sc-Cl (b), Cp^*_2Sc-Cl (c), Cp^*_2Sc-I (d).

Table 3.1. Selected distances and angles for Cp^*_2Sc-X.

X	Cp^*_a-Sc	Cp^*_b-Sc	Cp^*_a-Sc-Cp^*_b	Sc-X	Cp^*_a-Sc-X	Cp^*_b-Sc-X
Sc–F	2.1648(101) Å	2.1630(132) Å	145.492(53)°	1.9274(12) Å	108.30°	108.30°
Sc–Cl^	2.1517(115) Å	2.1624(115) Å	142.713(240)°	2.4175(16) Å	108.57°	109.45°
Sc–Br	2.1630(131) Å	2.1648(98) Å	142.329(77)°	2.5840(3) Å	108.97°	109.32°
Sc–I	2.1630(132) Å	2.1648(131) Å	140.511(77)°	2.8194(3) Å	108.91°	109.54°

^ – Average values for the four independent molecules in the unit cell.

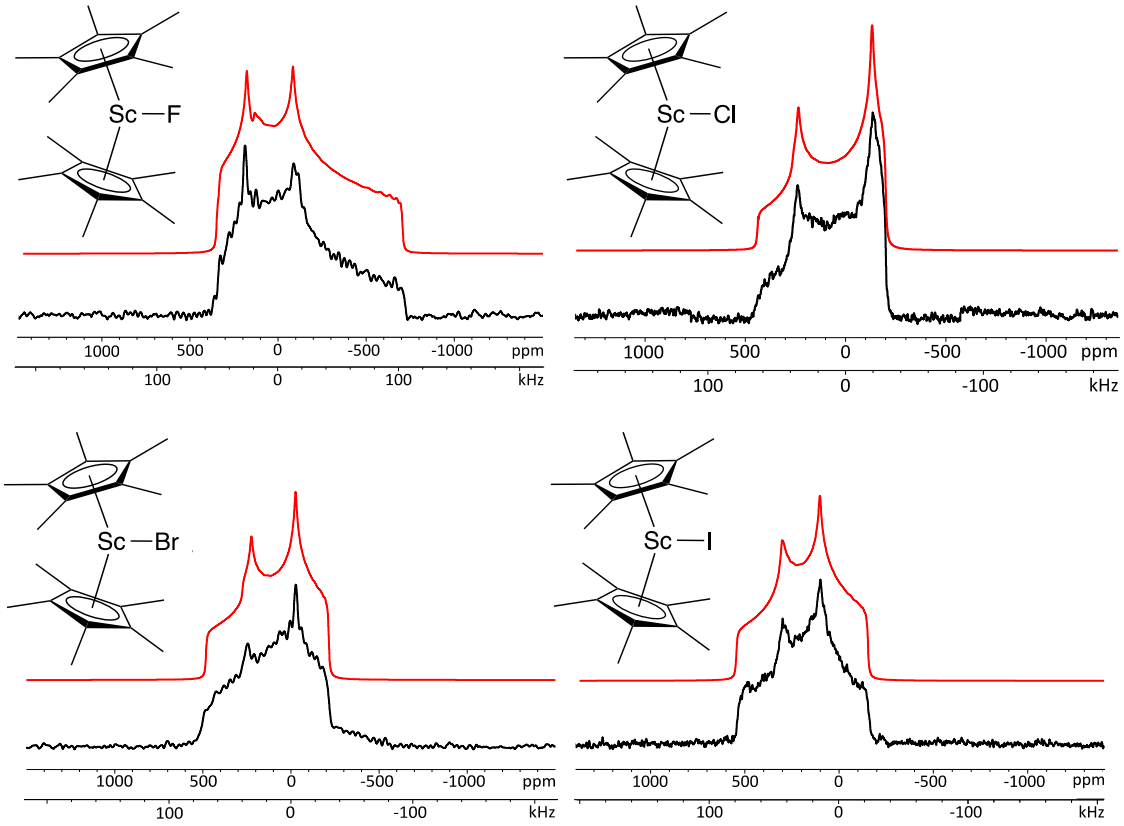

Figure 3.2. ^{45}Sc CT Solid-state NMR spectra of Cp*$_2$Sc–F (a); Cp*$_2$Sc–Cl (b); Cp*$_2$Sc–Br (c); Cp*$_2$Sc–I (d).

Table 3.2. ^{45}Sc NMR Parameters for Cp*$_2$ScX extracted from simulations in Figure 3.2.

X	δ_{iso} (ppm)	C_Q (MHz)	η	Ω (ppm)	κ	α (°)	β (°)	γ (°)
F	62	34.2	0.79	262	0.05	0	90	0
Cl	159	30.0	0.00	227	0.28	0	90	90
Br	201	29.2	0.11	235	0.88	0	90	0
I	266	27.4	0.29	176	0.44	0	90	0

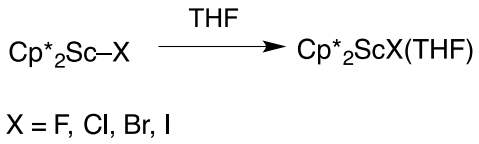

Scheme 3.2. Synthesis of Cp^*_2Sc-X(THF).

The addition of THF to each Cp^*_2Sc-X yields the THF adducts Cp^*_2Sc-X(THF). (Scheme 3.2) Attempts to recrystallize Cp^*_2Sc-X(THF), however, were unsuccessful. Dissolution of these compounds in hydrocarbon solvents yields Cp^*_2Sc-X and free THF. The geometry optimized structures for these compounds are shown given Figure 3.3. The solid-state NMR spectra of Cp^*_2Sc-X(THF) reveal that their C_Q are significantly smaller than their respective base-free Cp^*_2Sc-X. (Figure 3.3,3.5; Table 3.3)

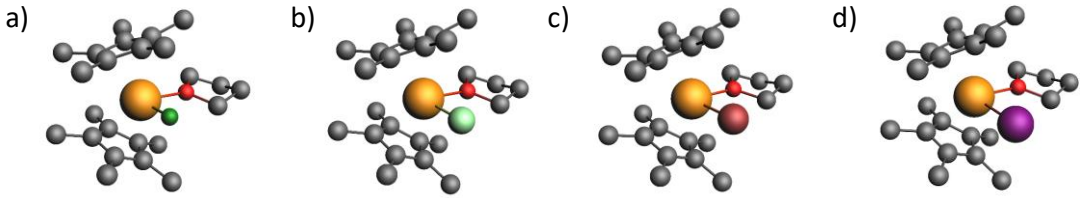

Figure 3.3. Optimized structures of $Cp^*_2ScF(THF)$ (a); $Cp^*_2ScCl(THF)$ (b); $Cp^*_2ScBr(THF)$ (c); $Cp^*_2ScI(THF)$ (d) at the B3LYP-GD3BJ/SDD(Sc,X)/6-31(d,p) level of theory in Gaussian 09.

Table 3.3. Calculated ^{45}Sc NMR Parameters for Cp^*_2ScX and for $Cp^*_2ScX(THF)$.

X	C_Q (MHz)	δ_{iso} (ppm)	η	Ω (ppm)	κ	α (°)	β (°)	γ (°)
F	-37.4	93	0.92	356	0.04	90	92	90
Cl	-30.8	207	0.17	316	0.17	90	91	90
Br	-29.5	224	0.13	255	0.26	82	91	91
I	-28.3	266	0.26	194	0.41	359	95	90
F(THF)	23.2	-30	0.10	139	-0.86	92	78	269
Cl(THF)	7.1	66	0.16	135	-0.43	28	95	92
Br(THF)	-5.9	83	0.20	122	0.04	150	89	265
I(THF)	-6.1	120	0.89	105	0.61	142	93	168

The geometries of Cp^*_2Sc-X and Cp^*_2Sc-X(THF) were calculated with B3LYP with Grimme's D3 dispersion with Beckie-Johnson damping (GD3BJ) at the SDD(Sc,X)/6-31G(d,p) level of theory and reproduce the experimental crystal structures of Cp^*_2Sc-X. (Figure 3.4, Table 3.4) The Cp^*_2Sc-X complexes all exhibit bent metallocene geometries that are typical of d^0 metals, with bond distances increasing in the expected order Sc-F < Sc-Cl < Sc-Br < Sc-I. Coordination of THF increases these bond distances. (Table 3.4-3.5).

To gain insight into the C_Q, the NMR calculations were performed on geometry-optimized Cp^*_2Sc-X and Cp^*_2Sc-X(THF). The predicted chemical shifts increase in the expected order F < Cl < Br < I, and the C_Q values decrease in the order F > Cl > Br > I, which agree with values observed experimentally. The calculations also reproduce smaller C_Q values for the THF adducts Cp^*_2Sc-X(THF) than the base free Cp^*_2Sc-X. (Table 3.3)

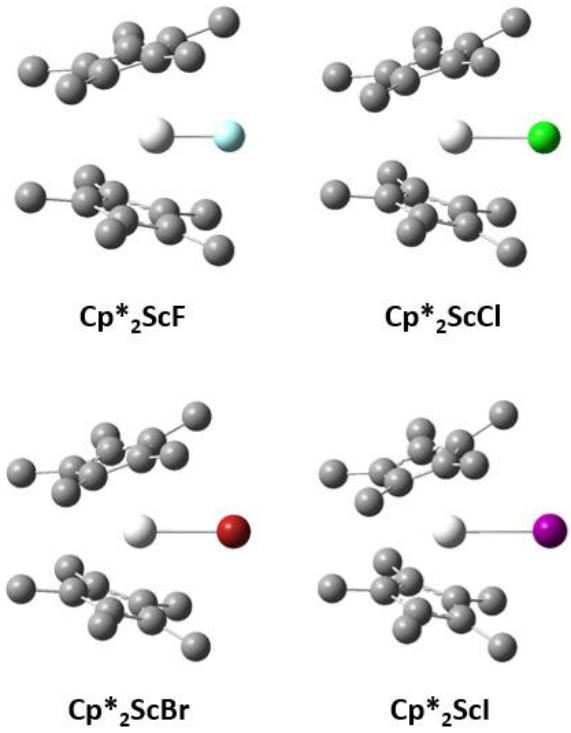

Figure 3.4. Geometry optimized structures of Cp*2Sc-X (X = F, Cl, Br, I) using B3LYP-GD3BJ, with SDD basis set for Sc, X and 6-31G(d,p) on C, H. Hydrogens omitted for clarity.

Table 3.4. Selected Geometry Optimized Parameters for Cp^*_2ScX (X = F, Cl, Br, I) from Figure 3.4.

	Cp^*_a-Sc	Cp^*_b-Sc	Cp^*_a-Sc-Cp^*_b	Sc-X	Cp^*_a-Sc-X	Cp^*_b-Sc-X
F	2.159 Å	2.159 Å	143.6°	1.917 Å	108.2°	108.2°
Cl	2.159 Å	2.159 Å	142.1°	2.435 Å	108.9°	108.9°
Br	2.161Å	2.162 Å	141.7°	2.604 Å	109.2°	109.1°
I	2.165 Å	2.166 Å	141.1°	2.840 Å	109.5°	109.5°

Table 3.5. Selected Geometry Optimized Parameters for Cp^*_2ScX(THF).

X	Cp^*_a-Sc	Cp^*_b-Sc	Cp^*_a-Sc-Cp^*_b	Sc-X	Sc-O	X-Sc-O
F	2.227 Å	2.227 Å	138.9°	1.931 Å	2.273 Å	83.7°
Cl	2.233 Å	2.234 Å	138.2°	2.475 Å	2.277 Å	87.7°
Br	2.233 Å	2.239 Å	137.5°	2.653 Å	2.286 Å	88.6°
I	2.237 Å	2.245 Å	137.4°	2.910 Å	2.293 Å	89.2°

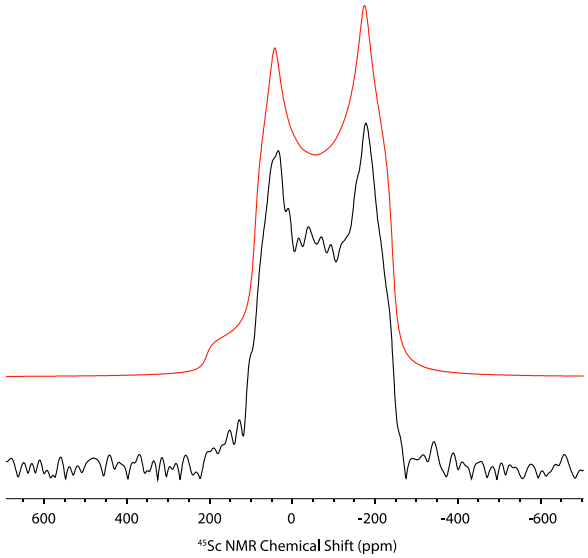

Figure 3.5a. Solid-state ^{45}Sc NMR of Cp*$_2$ScF(THF) (black) with a simulated spectrum (red).

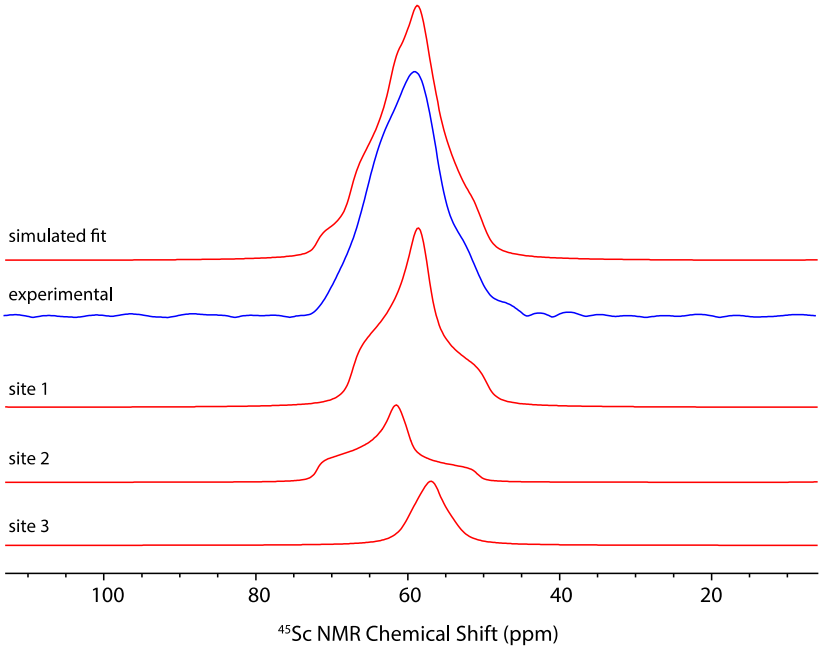

Figure 3.5b1. ^{45}Sc 1D MAS echo spectrum of Cp*$_2$ScCl(THF) at 14.1 T spinning at 9 kHz (blue). The simulated fit is obtained from the MQMAS experiment shown in Figure 3.5b2. Each site is shown below the experimental spectrum.

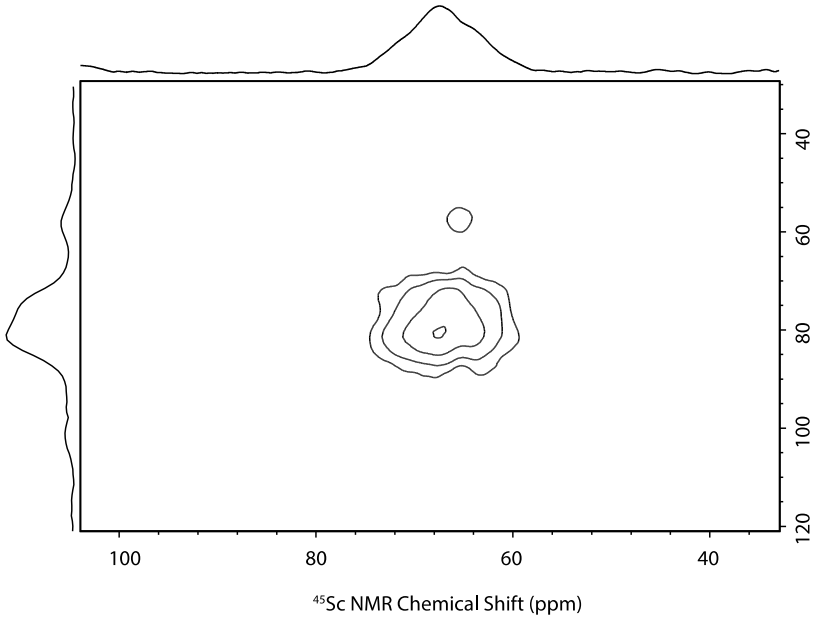

Figure 3.5b2. ^{45}Sc 3QMAS NMR of Cp*$_2$ScCl(THF) at 9.4 T.

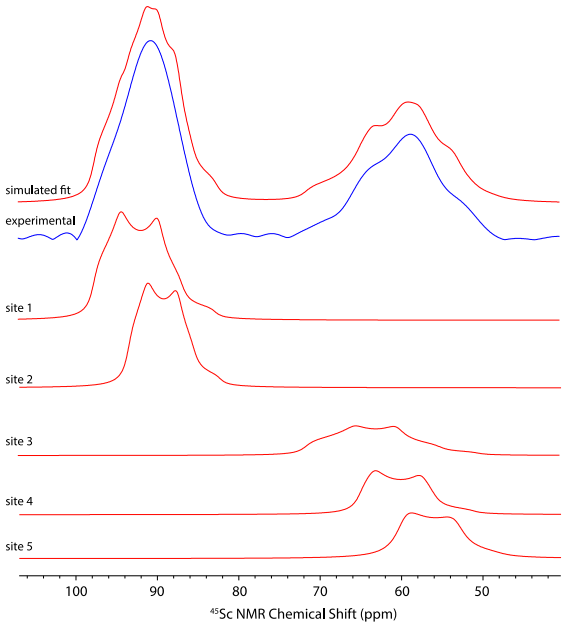

Figure 3.5c1. ^{45}Sc 1D MAS echo spectrum of Cp*$_2$ScBr(THF) at 14.1 T spinning at 9 kHz (blue). The simulated fit is obtained from the MQMAS experiment shown in Figure 3.5c2. Each site is shown below the experimental spectrum.

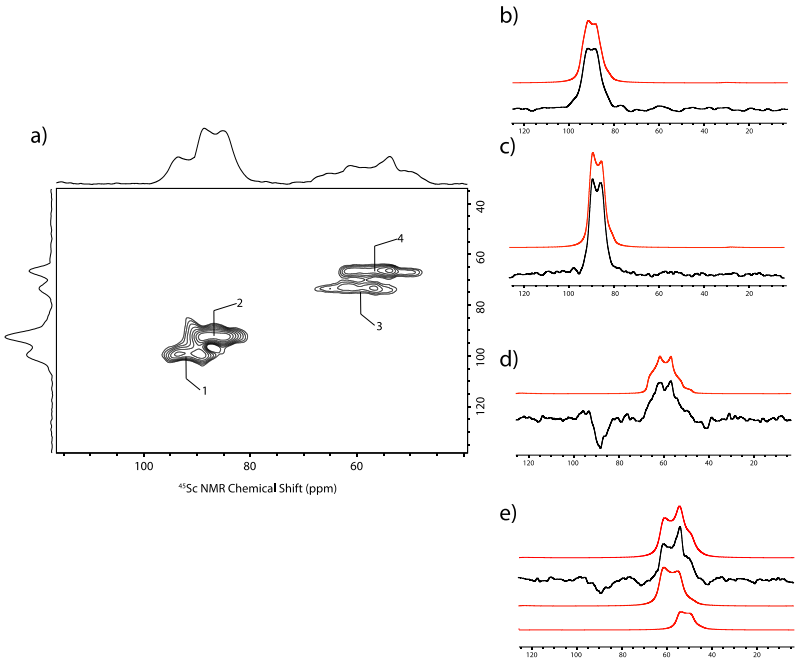

Figure 3.5c2. ^{45}Sc 3QMAS NMR of Cp*$_2$ScBr(THF) at 14.1 T (a). The 1D slices were extracted from the MQMAS spectrum in (a) and simulated using Topspin. Slice 1 fit (b), slice 2 fit (c), slice 3 fit (d), slice 4 fit (e).

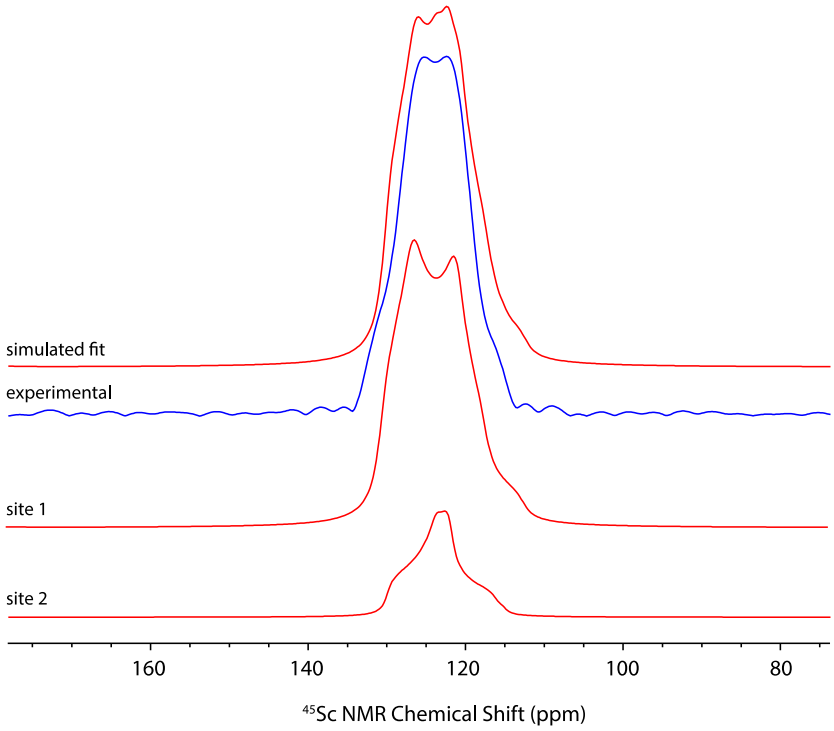

Figure 3.5d1. ^{45}Sc 1D MAS echo spectrum of Cp*$_2$ScI(THF) at 14.1 T spinning at 9 kHz (blue). The simulated fit is checked with the spectra recorded at 9.1T in Figure 3.5d2. The simulated sites are shown below the experimental spectrum.

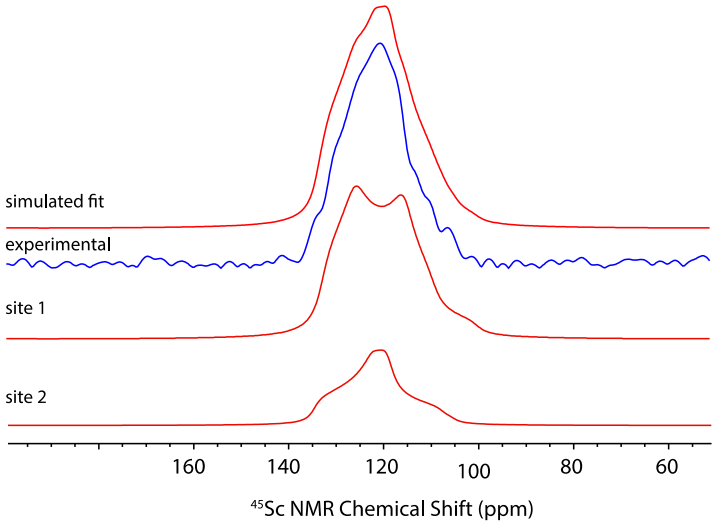

Figure 3.5d2. ^{45}Sc 1D MAS echo spectrum of Cp*$_2$ScI(THF) at 9.4 T spinning at 9 kHz (blue). The simulated fit is checked with the spectra recorded at 14.1T in Figure 3.5d1. The simulated sites are shown below the experimental spectrum.

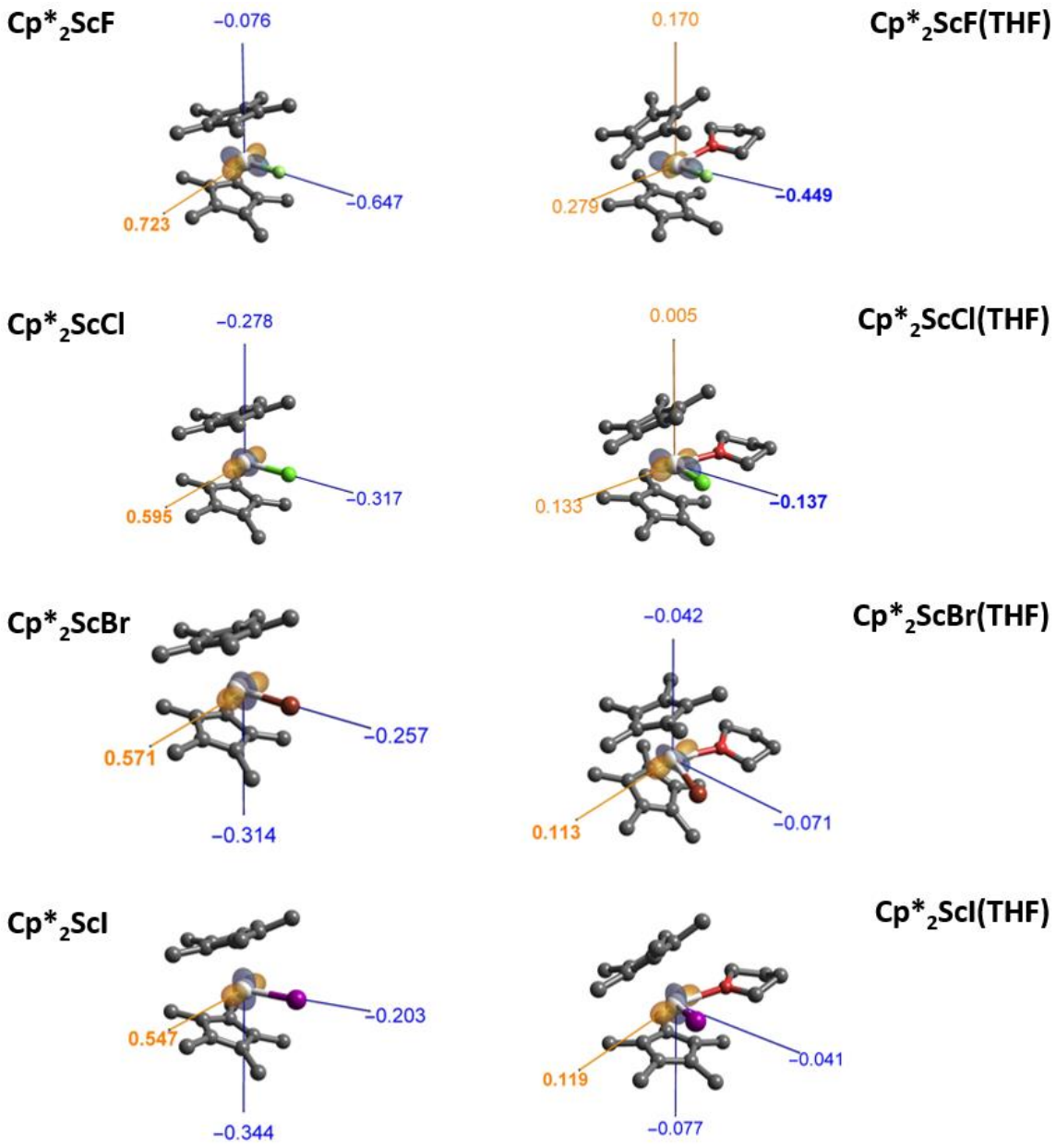

Figure 3.6. Calculated Electric Field Gradient Tensor Plots for Cp^*_2ScX and $Cp^*_2ScX(THF)$ for X = F, Cl, Br, I. All hydrogens were omitted for clarity. Sc-Br and Sc-I bond lengths were manipulated for display purposes only.

The orientation of the electric field gradient tensor and its principal axes are calculated and shown in Figure 3.6 on the previous page for Cp^*_2Sc-X and Cp^*_2Sc-X(THF). The V_{33} is responsible for the C_Q that is observed experimentally, and each point in the direction of the d_{z2} orbital. For Cp^*_2Sc-X, this orbital is perpendicular to the σ(Sc-X) bond. The donation of electron density from THF into this orbital results in a reduction of the C_Q, most prominent for Cp^*_2Sc-I and Cp^*_2Sc-I(THF).

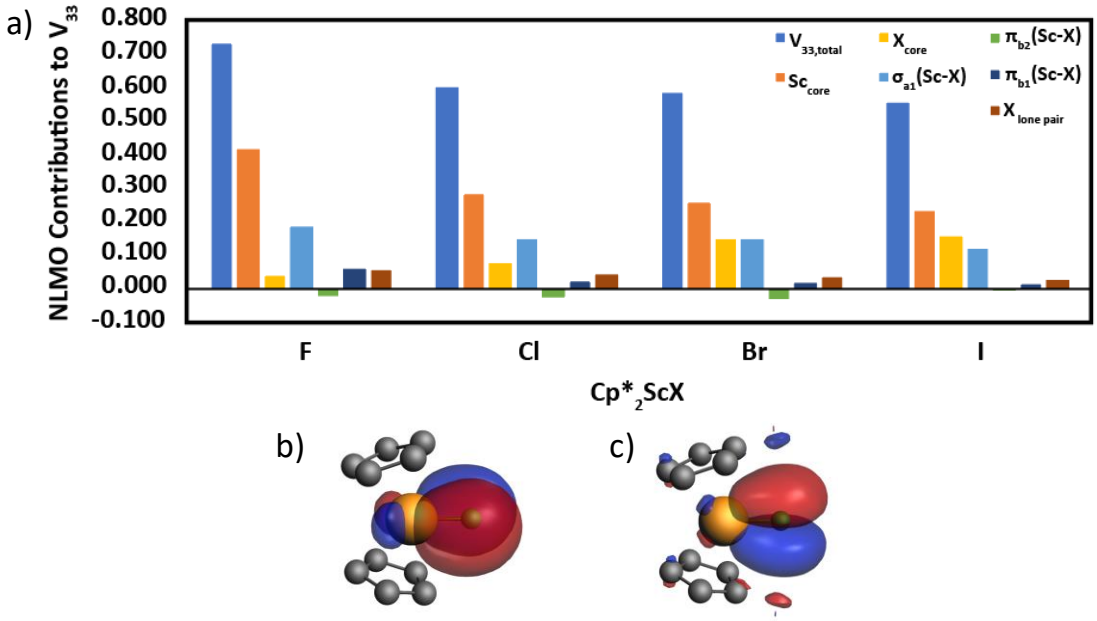

Figure 3.7. Contributions of NLMO to V_{33} in Cp^*_2Sc–X (a); π_{b2} (b) and π_{b1} (c) NLMO; isovalue = 0.01.

The Natural Localized Molecular Orbital (NLMO) analysis of V_{33} reveals that the largest contributor to C_Q is the core scandium orbitals, with the core halide orbitals playing a more significant role going down the halide series. (Figure 3.7a) The largest valence contributor to V_{33} is the Sc-X bond, decreasing in magnitude from fluoride to iodide. The

halide also contains two additional interactions which affect V_{33}, although to a much lesser extent. (Figure 3.7b)

Cp^*_2Sc-X react with THF to form Cp^*_2Sc-X(THF) via donation of electron density from THF into the empty d_{z^2} orbital. DFT calculations reveal that the geometry of Cp^*_2Sc-X(THF) is pseudotetrahedral and is typical of d^0 bent metallocenes. Increasing the spherical symmetry in this manner is expected to yield smaller C_Q values than the planar base-free Cp^*_2Sc-X. (Figure 3.8) A qualitative analysis of the orbitals responsible for this interaction are shown in Figure 3.9. Townes and Dailey's semi-empirical studies related the magnitude of C_Q the population of empty orbitals, and indeed in these compounds, occupation of the d_{z^2} LUMO results in a reduced C_Q. In these orbitals, the d_{z2} orbital ($1a_1$) is in fact the largest valence contributor to the C_Q in all Cp^*_2Sc-X.

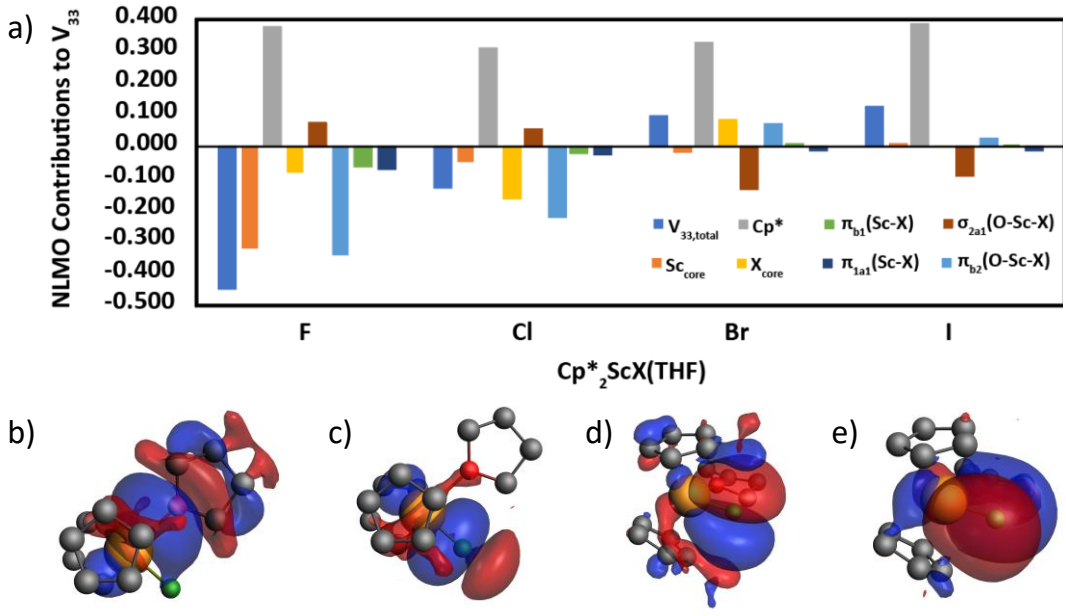

Figure 3.8. Contributions of NLMO to V_{33} in $Cp^*_2ScX(THF)$ (a); plots of valence NLMO σ_{1a1} (b), π_{b2} (c), π_{b1} (d) and π_{2a1} (e) for the fluoride; isovalue = 0.005.

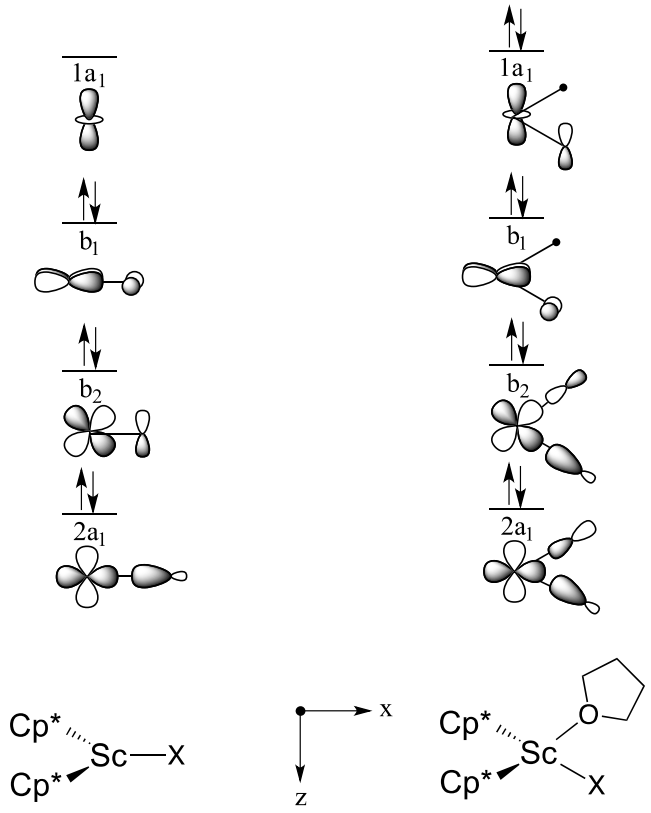

Figure 3.9. Qualitative molecular orbitals in $Cp^*_2Sc–X$ (left) and $Cp^*_2ScX(THF)$ (right).

3.4 Conclusion

The halides of Cp^*_2Sc-X and Cp^*_2Sc-X(THF) have been synthesized and studied via quadrupolar solid-state ^{45}Sc NMR and DFT methods. The results show that C_Q is a sensitive reporter of electronic structure since it relates the occupation of core and valence orbitals. In Cp^*_2Sc-X, the Sc-X π-bonds contribute relatively small values to the C_Q and therefore does not provide a good handle for measuring π-donation to scandium for the base-free compounds. The addition of THF to Cp^*_2Sc-X results in pseudotetrahedral Cp^*_2Sc-X(THF), which results in smaller C_Q values than those observed in base-free adducts. Although there are major core contributions from scandium and halide to the C_Q

in these compounds, there are more pronounced differences in the σ/π bonding interactions in their contributions to V_{33}. These results show that a combined solid-state NMR and DFT analysis of organoscandium complexes can provide valuable electronic and structural information.

3.5 Materials and Methods

All syntheses were performed under an atmosphere of argon. Benzene-d_6 was purchased from Cambridge Isotope Laboratories and dried over sodium and benzophenone, distilled under vacuum, and stored inside a glove box. All other solvents were purchased from Fischer Scientific. Pentane and toluene were dried with the same procedures as benzene-d_6, degassed, and distilled under vacuum. Lithium bromide was purchased from Sigma Aldrich and dried at 160 ^{o}C under high vacuum prior to use. Dry lithium iodide was purchased from Sigma Aldrich and used without further purification. Vinyl fluoride was obtained from PCR Research Chemicals, Inc. The synthesis of Cp*$_2$ScCl, Cp*$_2$ScMe, and Cp*$_2$ScI was reported previously.[3]

Synthesis of Cp$_2$ScF:* Benzene (~10 mL) was condensed into a flask containing Cp*$_2$Sc–Me (500 mg, 1.5 mmol) by vacuum transfer at -196°C. The pale-yellow solution was warmed to room temperature, and the solution was exposed to 1 atm of vinyl fluoride (10 mmol). The reaction mixture evolves to a golden color. The mixture was stirred for 1 h at room temperature, and the volatiles were removed in vacuo. The yellow solid was extracted with pentane (10 mL), filtered, and recrystallized from concentrated pentane solution at -20 °C, yielding pale yellow crystals of Cp*2ScF (155 mg, 31 %). ^{1}H NMR

(C_6D_6, 300 MHz): 1.90 (s, 30H, C_5Me_5), $^{45}Sc\{^1H\}$ NMR (C_6D_6, 72.9 MHz): 65.7 ppm, ^{19}F NMR (C_6D_6, 282.4 MHz): 59 ppm. Anal. Calcd. For $C_{20}H_{30}ScF$: C, 71.82; H, 9.06. Found: C, 71.50; H, 8.74.

Synthesis of Cp$_2$ScBr:* Toluene (30 mL) was added by cannula to a Schlenk tube containing Cp*$_2$Sc–Cl (294 mg, 0.743 mmol) and LiBr (80.2 mg, 1.621 mmol, 2.2 eq.). The reaction mixture was heated to 95°C and stirred under argon for 22 h. The reaction mixture was cooled to room temperature and toluene was removed under vacuum. Pentane (20 mL) was added to the yellow solid to produce a yellow solution and a white solid, which was removed by filtration. The clear yellow pentane solution was concentrated to ~ 7 mL and stored at –20 °C. Cp*$_2$ScBr precipitates as yellow X-ray quality crystals (211 mg, 64%). ^1H NMR (C_6D_6, 300 MHz): 1.89 (s, 30H, C_5Me_5), $^{45}Sc\{^1H\}$ NMR (C_6D_6, 72.9 MHz): 203.3 ppm. Anal. Calcd. For $C_{20}H_{30}ScBr$: C, 60.75; H, 7.66. Found: C, 60.55; H, 7.49.

Synthesis of Cp$_2$ScI:* Toluene (20 mL) was added by cannula to a Schlenk tube containing Cp*$_2$ScCl (169 mg, 0.482 mmol) and LiI (80.2 mg, 0.6 mmol, 1.2 eq.). The reaction mixture was heated to 80°C and stirred under argon for 26 h. The reaction mixture was cooled to room temperature and toluene was removed in vacuo. Pentane (20 mL) was added to the yellow solid to produce a yellow solution and a white solid, which was removed by filtration. The clear yellow pentane solution was concentrated to ~ 7 mL and stored at –20 °C. Cp*$_2$ScI precipitates as yellow X-ray quality crystals (158 mg, 74%). ^1H NMR (C_6D_6, 300 MHz): 1.91 (s, 30H, C_5Me_5), $^{45}Sc\{^1H\}$ NMR (C_6D_6, 72.9 MHz): 256.9 ppm.

*General procedure for the synthesis of Cp*2ScX(THF):* A sample of $Cp^*_2Sc–X$ (100-200 mg) was weighed into a flask containing a Teflon tap. The flask was connected to a high vacuum line and evacuated. THF (~ 5 mL) was condensed to the flask at 77 K, and the mixture was warmed to room temperature. $Cp^*_2ScX(THF)$ precipitates from THF as beige powders. Excess THF was removed under vacuum and the solid was dried at room temperature. The yields are essentially quantitative. C_6D_6 solutions of $Cp^*_2ScX(THF)$ show signals for $Cp^*_2Sc–X$ and free THF in ^1H, ^{13}C, and ^{45}Sc NMR spectra.

NMR Experiments: Solution phase ^1H and $Sc\{^1H\}$ Hahn echo NMR spectroscopy were carried out on an Avance Bruker 300, and the spectra were referenced to the NMR solvent residual peak or an external standard of 0.11M $ScCl_3$ in 0.11 M aqueous HCl solution (0.00 ppm) respectively. Solid state NMR spectra were recorded in 4 mm zirconia rotors on 14.1 T Bruker Neo-600 NMR or 9.4 T Bruker Avance III spectrometers. Static $^{45}Sc\{^1H\}$ NMR spectra were recorded with a Hahn-echo pulse sequence, with full echo detection ($\pi/2 – \tau – \pi –$ acq), using frequency stepped acquisition at low ν_{RF} field strengths.[5] Echo delays (τ) were set to 100 – 250 μsec. All analytical simulations of solid state spectra were performed in Topspin using Sola line shape analysis. 3QMAS NMR spectra were acquired using a z-filtered pulse sequence,[6] and processed using the shearing function in Topspin. 1D slices were extracted in Topspin and fit using Sola lineshape analysis.

DFT Calculations: The geometries of $Cp^*_2Sc–X$ (X = F, Cl, Br, I) were optimized with Gaussian 09 using the B3LYP functional[7] containing Grimme's D3 dispersion with Becke-Johnson damping.[8] Sc and X were described with the SDD basis set,[9] and all other atoms

were represented with the 6-31G(d,p) basis set. $Cp^*_2ScX(THF)$ were optimized at the same level of theory. NMR parameters were calculated with the geometry-optimized structures using B3LYP/DZ in the Amsterdam Density Functional (ADF).[10] NMR shielding was calculated using the GIAO method.[11-12] Relativistic scalar two component zero order regular approximation (ZORA)[13-14] was included for Cp^*_2ScBr, Cp^*_2ScI, $Cp^*_2ScBr(THF)$ and $Cp^*_2ScI(THF)$.[15-17] The calculated isotropic chemical shift was referenced to geometry-optimized $Sc(H_2O)_6^{3+}$ at the same level of theory, which was used previously to reference ^{45}Sc chemical shift calculations.[17] Contributions of Naturalized Localized Molecular Orbitals (NLMO) to C_Q were calculated using the B3LYP/DZ level of theory in ADF, with scalar relativistic ZORA for complexes with bromine and iodine. This decomposition analysis provides key information on how the core and valence orbitals contribute to C_Q. A more detailed discussion of this technique was described previously.[18]

3.6 References

[1] Culver, D. B.; Huynh, W.; Tafazolian, H.; Ong, T. C.; Conley, M. P. *Angew. Chem. Int. Ed.* **2018**, *57*, 9250-9253.

[2] Lukens, W. W.; Smith, M. R.; and Andersen, R. A. *J. Am. Chem. Soc.* **1996**, *118*, 1719-1728.

[3] Thompson, M. E.; Baxter, S. M.; Bulls, A. R.; Burger, B. J.; Nolan, M. C.; Santarsiero, B. D.; Schaefer, W. P.; Bercaw, J. E. *J. Am. Chem. Soc.* **1987**, *109*, 203-219.

[4] Strazisar, S. A.; Wolczanski, P. T.; *J. Am. Chem. Soc.* **2001**, *123*, 4728-4740.

[5] Medek, A.; Frydman, V.; Frydman, L. *J. Phys. Chem. A*, **1999**, *103*, 4830-4835.

[6] Amoureux, J.-P.; Fernandez, C.; Steuernagel, S. *J. Magn. Reson. Ser. A*, **1996**, *123*, 116-118.

[7] M. J. Frisch, G. W. Trucks, H. B. Schlegel, G. E. Scuseria, M. A. Robb, J. R. Cheeseman, G. Scalmani, V. Barone, G. A. Petersson, H. Nakatsuji, X. Li, M. Caricato, A. Marenich, J. Bloino, B. G. Janesko, R. Gomperts, B. Mennucci, H. P. Hratchian, J. V. Ortiz, A. F. Izmaylov, J. L. Sonnenberg, D. Williams-Young, F. Ding, F. Lipparini, F. Egidi, J. Goings, B. Peng, A. Petrone, T. Henderson, D. Ranasinghe, V. G. Zakrzewski, J. Gao, N. Rega, G. Zheng, W. Liang, M. Hada, M. Ehara, K. Toyota, R. Fukuda, J. Hasegawa, M. Ishida, T. Nakajima, Y. Honda, O. Kitao, H. Nakai, T. Vreven, K. Throssell, J. A. Montgomery Jr., J. E. Peralta, F. Ogliaro, M. Bearpark, J. J. Heyd, E. Brothers, K. N. Kudin, V. N. Staroverov, T. Keith, R. Kobayashi, J. Normand, K. Raghavachari, A. Rendell, J. C. Burant, S. S. Iyengar, J. Tomasi, M. Cossi, J. M. Millam, M. Klene, C. Adamo, R. Cammi, J. W. Ochterski, R. L. Martin, K. Morokuma, O. Farkas, J. B. Foresman and D. J. Fox, Gaussian 09, 2016.

[8] Stefan, G.; Stephan, E.; Lars, G. *J. Comput. Chem.* **2011**, *32*, 1456-1465.

[9] T. H. Dunning Jr. and P. J. Hay, in Mondern Theoretical Chemistry, ed. H. F. Schaefer III, Plenum, New York, 1977, vol. 3, pp. 1–28.

[10] te Velde, G.; Bickelhaupt, F. M.; Baerends, E. J.; Guerra, C. F.; van Gisbergen, S. J. A.; Snijders, J. G.; Ziegler, T. *J. Comp. Chem.* **2001**, *22*, 931.

[11] Schreckenbach, G.; Ziegler, T. J. Phys. Chem. 1995, 99, 606-611.

[12] Krykunov, M.; Ziegler, T.; Van Lengthe, E.; *Int. J. Quant. Chem.*, **2009**, *109*, 1676-1683.

[13] E. van Lenthe, E. J. Baerends and J. G. Snijders, *J. Chem. Phys.*, **1996**, *105*, 6505–6516;

[14] E. van Lenthe, E. J. Baerends and J. G. Snijders, *J. Chem. Phys.*, **1994**, *101*, 9783–9792;

[15] E. van Lenthe, E. J. Baerends and J. G. Snijders, *J. Chem. Phys.*, **1993**, *99*, 4597–4610.

[16] E. van lenthe, E. J. Baerends and J. G. Snijders, Relativistic, *J. Chem. Phys.*, **1994**, *101*, 9783–9792

[17] Rudolph, W. W.; Pye, C. C.. *J. Phys. Chem. A.* **2000**, *104*, 1627-1639.

[18] Autschbach, J.; Zheng, S.; Schurko, R. W. *Concepts Magn. Reson., Part A,* **2010**, *36A*, 84-126.

CHAPTER 4

Solid-state ^{45}Sc NMR Studies of Cp^*_2Sc-OR (R = CMe_2CF_3, $CMe(CF_3)_2$, $C(CF_3)_3$, $SiPh_3$) and Relationship to the Structure of Cp^*_2Sc-Sites Supported on Partially Dehydroxylated Silica

4.1 Abstract:

Cp^*_2Sc-OR (R = CMe_2CF_3, $CMe(CF_3)_2$, $C(CF_3)_3$, $SiPh_3$) were synthesized to determine how the electronics of each alkoxide is related to the C_Q obtained from solid-state ^{45}Sc NMR spectroscopy. Each are characterized by C_Q's larger than 29MHz, which are similar to those obtained from three-coordinate Cp^*_2Sc-R (R = Me, Et, Ph) and Cp^*_2Sc-X (X = F, Cl, Br, I) and significantly larger than those obtained for $Cp^*_2ScX(THF)$. The reaction of Cp^*_2Sc-Me with silica partially dehydroxylated at 700 ^oC releases methane and yields $Cp^*_2ScOSi{\equiv}$(**5a**) and $Cp^*_2Sc(OSi{\equiv})O(SiO_x)_2$ (**5b**). The solid-state ^{45}Sc NMR of **5a** is noticeably broader than **5b**, revealing a different coordination environment around scandium. The density functional theory (DFT) optimized structures of **5a** and **5b** follow the trends expected for this family of organoscandium complexes. Further analyses of the origin of the C_Q via DFT shows that the σ- and π- bonding orbitals from the Sc-O bond in Cp^*_2Sc-OR and 5a are major contributors to the C_Q, whereas different orbitals contribute to the C_Q in **5b**. These studies show that quadrupolar solid-state NMR spectroscopy and DFT together can be used to unambiguously distinguish between different surface sites on partially dehydroxylated silica.

4.2 Introduction:

Many large-scale reactions in industry employ heterogeneous catalysts. These catalysts usually contain organometallic intermediates, often tethered to a metal or an oxide surface.[1] Understanding the structure of these catalysts is difficult because of their low active site loadings, which complicate spectroscopic analysis. Obtaining a crystal structure is also unfeasible since the active sites are often anchored onto an amorphous surface support. One method to addressing this challenge is to tether an organometallic complex onto a partially dehydroxylated support. (Scheme 4.1).

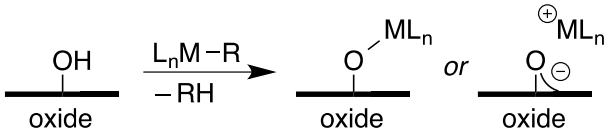

Scheme 4.1 Reaction of organometallic with surface oxide to form M-Ox or M---Ox ion pairs.

The grafting of an organometallic alkyl complex on a partially dehydroxylated surface results in the formation of an alkane and a well-defined supported organometallic that forms a covalent M-O_x (O_x = surface oxygen) bond or an electrophilic M---O_x ion pair. The ratio of M-O_x and M---O_x is controlled by the nature of the support. Neutral supports such as silica and alumina generally form M-O_x, and Bronsted acidic supports such as zeolites and sulfated oxides generally form M---O_x ion pairs.[2-5]

Solid-state NMR is the most common method to determining structure in well-defined organometallics supported on oxides. While solid-state NMR generally contains

signals broader than those obtained in solution-state spectra, the chemical shift anisotropy can be suppressed via magic angle spinning to reproduce isotropic chemical shifts with narrower patterns similar to those obtained in solution. The solid-state NMR of quadrupolar nuclei may distinguish between bonding environments, as shown in Chapter 2-3. Grafting a quadrupolar organometallic onto partially dehydroxylated silica is a strategy to developing a molecular understanding of the coordination environment of organometallics on partially dehydroxylated silica.

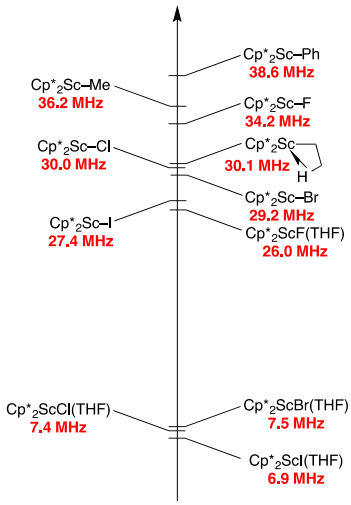

Figure 4.1. Summary of known ^{45}Sc quadrupolar coupling constants.

This chapter describes the synthesis of Cp*$_2$Sc-OR (R = CMe_2CF_3, $CMe(CF_3)_2$, $C(CF_3)_3$, $SiPh_3$) and the reaction of Cp*$_2$Sc-Me with partially dehydroxylated silica at 700 ^{o}C. As shown in Chapter 1-2, the ^{45}Sc quadrupolar coupling constant (C_Q) is sensitive to symmetry and the occupation of core and valence orbitals. The C_Q of the Cp*$_2$Sc-R (R = Me, Et, Ph), Cp*$_2$Sc-X (X = F, Cl, Br, I), and Cp*$_2$Sc-X(THF) synthesized in Chapter 1-2 are shown in Figure 4.1. The base-free Cp*$_2$Sc-R and Cp*$_2$Sc-X are characterized by

relatively large C_Q values >27 MHz. These values are larger than the scandium complexes that contain higher symmetry environments and crystalline porous materials[6-7] but smaller than the C_3 $Sc[N(SiMe_3)]_3$ amide (C_Q = 66.2 MHz). Figure 4.1 shows how the C_Q is sensitive to subtle changes in structure. For example, Cp^*_2Sc-Et contains a β-agostic CH, resulting in a smaller C_Q than Cp^*_2Sc-Me. The effect is even more noticeable in the base adducts of Cp^*_2Sc-X and $Cp^*_2ScX(THF)$. The DFT studies of the THF adducts reveal that the smaller C_Q values are due to higher symmetry at Sc, which results in the occupation of d_{z^2} orbitals that were otherwise unoccupied for Cp^*_2Sc-X.

The solid-state ^{45}Sc NMR data in Figure 4.1 will be an empirical aid for the interpretation of Cp^*_2Sc-Me supported on partially dehydroxylated silica. The formation of $Cp^*_2ScOSi\equiv$, a terminal siloxy surface species, should result in a large C_Q. In contrast, the formation of Cp*2ScOSi≡ and subsequent coordination to a siloxane bridge results in $Cp^*_2Sc(OSi\equiv)O(SiO_x)_2$ should result in smaller C_Q than Cp*2ScOSi≡.

DFT methods can accurately predict C_Q, and further analyses can decompose the C_Q into contributions from individual natural localized molecular orbitals (NLMOs). DFT descriptions of amorphous supports such as SiO_2 are complex, but a handful of studies show that small cluster models can predict C_Q values close to experimental values if the coordination environment is correct. Approximations as simple as replacing silica with $-OSi(OMe)_3$ have been shown to predict spectroscopic patterns of organometallic supported on silica.[8-11]

DFT calculations of the molecular alkoxides Cp*$_2$Sc-OR (R = CMe$_2$CF$_3$, CMe(CF$_3$)$_2$, C(CF$_3$)$_3$, SiPh$_3$) accurately reproduce the C_Q. These molecules serve as a benchmark for the reaction products of Cp*$_2$Sc-Me supported on silica. Indeed, the small cluster models of Cp*$_2$Sc(OSi≡)O(SiO$_x$)$_2$ and Cp*$_2$Sc-OSi≡ shown in Figure 4.2 and their calculated C_Q values reveal that they are the reaction products. The NLMO analyses of orbital contributions to the C_Q for the cluster shows that the geometry differences in the κ^1 and κ^2 coordination mode of -OSi(OMe)$_3$ are responsible for the different C_Q values.

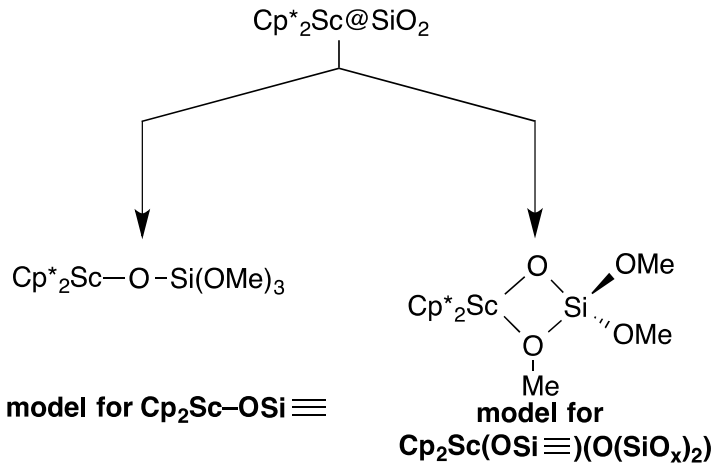

Figure 4.2. DFT models for Cp*$_2$ScOSi≡ and Cp*$_2$Sc(OSi≡)O(SiO$_x$)$_2$.

4.3 Results and Discussion

Cp*$_2$Sc-Me reacts with fluorinated alcohols and triphenylsilanol to form methane and Cp*$_2$Sc-OR (R = CMe$_2$CF$_3$ (**1**), CMe(CF$_3$)$_2$ (**2**), C(CF$_3$)$_3$ (**3**), SiPh$_3$ (**4**)). (Scheme 4.2). The products are crystalline (**1** and **3**) and microcrystalline (**2** and **4**). The X-ray crystal structures of **1** and **3** are shown in Figure 4.3. Both adopt bent C_{2v} structures typical of d^0

metallocenes. The Sc-O distance in **1** is 1.9481(8) Å, which is shorter than the Sc-O distance of 2.033(1) Å in **3**. The Cp*-Sc bond distances in **1** are 2.2031(6) and 2.2088(6) Å, and the Cp*-Sc-Cp* angle is 135.26(2)°. The Cp*-Sc-Cp* angle in **3** is 133.9(1)°, and the Cp*-Sc bond distances are 2.199(1) and 2.205(1) Å. These structural parameters are similar to known scandocene complexes including those presented in Chapter 2-3.

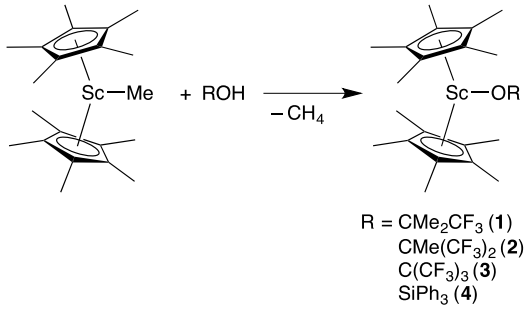

Scheme 4.2. Synthesis of $Cp^*_2Sc–OR$.

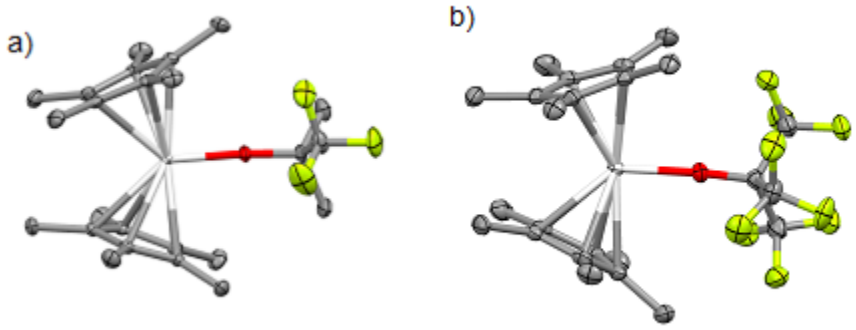

Figure 4.3 X-ray crystal structure of $Cp^*_2Sc\text{-}OCMe_2CF_3$ (a) and $Cp^*_2Sc\text{-}O(C(CF_3)_3$ (b), with hydrogen atoms hidden for clarity.

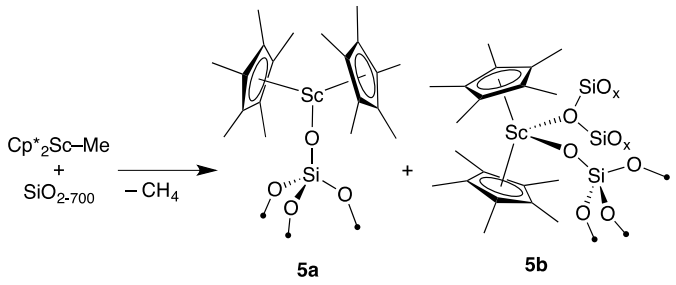

Scheme 4.3. Synthesis of $Cp^*_2ScOSi\equiv$ (**5a**) and $Cp^*_2Sc(OSi\equiv)O(SiO_x)_2$ (**5b**).

Similar to the syntheses of **1-4**, the reaction of Cp^*_2Sc-Me and $SiO_{2\text{-}700}$ forms methane but two organometallic products: $Cp^*_2ScOSi\equiv$ (**5a**) and $Cp^*_2Sc(OSi\equiv)O(SiO_x)_2$ (**5b**). (Scheme 4.3) $SiO_{2\text{-}700}$ contains and -OH loading of 0.26 mmol g^{-1}, and this reaction forms 0.23 mmol g^{-1} methane which is close to the expected yield. The FTIR spectrum of **5** contains the expected sp^3 ν_{CH} and sp^2 ν_{CC} stretches from the Cp* fragment. In addition, there is a significant decrease in the ν_{OH} band which indicates consumption of isolated and geminal silanols that are present on the $SiO_{2\text{-}700}$ surface. (Figure 4.4) The ^{13}C CPMAS contains only signals at 121.5 and 9.5 ppm that are expected for the Cp* ligand, and the ^{29}Si spectrum contains only signals for bulk SiO_2. (Figure 4.5) The ^{13}C and ^{29}Si NMR spectra do not distinguish **5a** and the proposed **5b**, but the results from Chapter 2-3 suggest that **5b** could be present as well.

The static $^{45}Sc\{^1H\}$ NMR spectrum of **1-5** is recorded on 14.1 and 9.4 T spectrometers, and selected spectra are shown in Figure 4.6, page 66. The spectra of **5** is more complicated than **1**-**4**. There are clear differences in **5** that suggest the presence of two sites, which is consistent with the presumption that the reaction forms **5a** and **5b**. The simulated parameters of these spectra are presented in Table 4.1 (page 67). The average C_Q

of **1-4** are all > 29 MHz, and the site that is simulated to an average C_Q of 35.4(4) MHz is assigned to **5a**. The second site contains a narrow signal with an average C_Q of 21.9(3) MHz and is assigned to **5b**. DFT calculations of **1-4** and small models of **5a** and **5b** will be discussed below support this characterization.

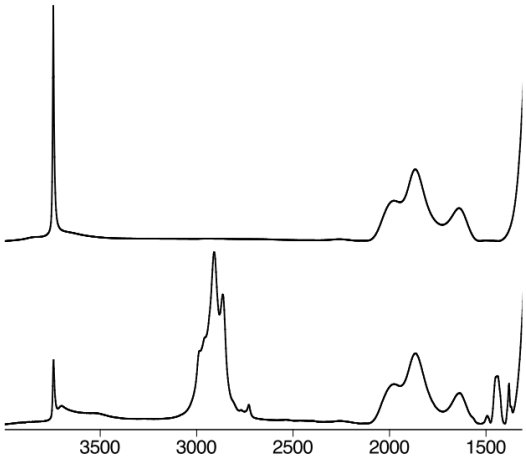

Figure 4.4 FTIR spectra of $SiO_{2\text{-}700}$ (top) and both $Cp^*_2ScOSi\equiv$ and $Cp^*_2Sc(OSi\equiv)O(SiO_x)_2$ (bottom).

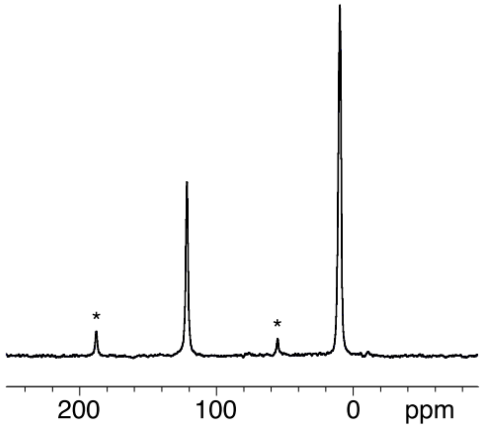

Figure 4.5. Solid-state $^{13}C\{^1H\}$ CPMAS NMR spectrum of 5 spinning at 10kHz, with * denoting spinning side bands.

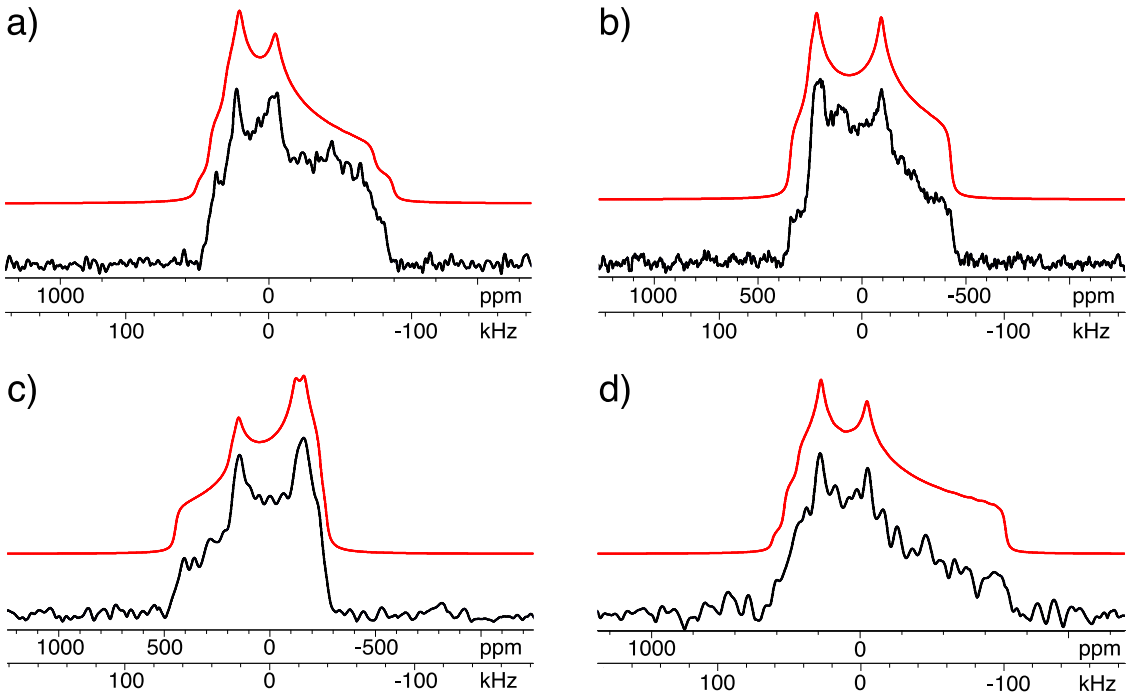

Figure 4.6. Static solid-state $^{45}Sc\{^{1}H\}$ NMR spectra of **1** (a), **2** (b), **3** (c), and **4** (d) acquired at 14.1 T. Experimental spectra is in black, and simulated spectra re in red.

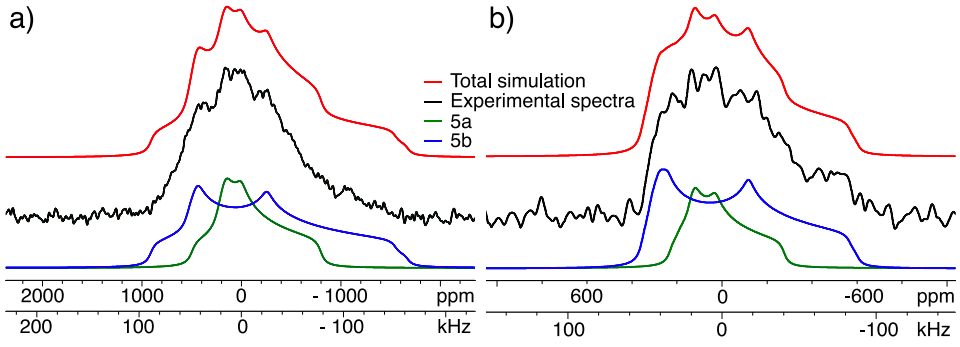

Figure 4.7. Static Static solid-state $^{45}Sc\{^{1}H\}$ NMR spectrum of 5 at 9.4T (a) and 14.1T (b). Experimental spectra is in black, and simulated spectra re in red. The simulation of **5a** is shown in blue and of **5b** is shown in green.

Table 4.1. ^{45}Sc NMR Parameters for 1-5 Extracted from Figure 4.6 and Figure 4.7. Values reported are average of simulations at 9.4 and 14.1T. Numbers in parentheses give the deviation from the average.

	δ_{iso} (ppm)	C_Q (MHz)	η	Ω (ppm)	κ	α (°)	β (°)	γ (°)
1	65(5)	31.6(1)	0.80(1)	290(20)	0.50(1)	95(5)	90(1)	90(1)
2	99(1)	30.5(1)	0.63(2)	270(10)	0.19(4)	106(4)	88(2)	88(3)
3	133(1)	29.2(2)	0.33(1)	375(3)	0.25(5)	103(2)	96(6)	78(3)
4	94(2)	35.1(1)	0.77(1)	239(3)	0.5(1)	108(5)	89(2)	90(1)
5a	135(15)	35.4(4)	0.60(5)	315(20)	0.90(8)	90(1)	90(1)	90(1)
5b	95(5)	21.9(3)	0.77(3)	150(15)	0.65(9)	90(1)	90(1)	90(1)

The structures of **1-4** were optimized with the B3LYP functional at the 6-31G**(Sc)/6-31G*(C, H, O, F, Si) level of theory. The structural parameters obtained from these optimizations are given in Table 4.2, and the values of **1** and **3** agree well with the X-ray crystal structures. The structures of **2** and **4** are qualitatively similar, adopting the C_{2v} bent metallocene with Sc-O-C or Sc-O-Si bond angles that are nearly linear. In order to model **5a** and **5b**, the smaller trimethoxysilyl group was used to model $SiO_{2\text{-}700}$. $Cp^*_2Sc(\kappa^1\text{-}OSi(OMe)_3)$ (**6a**) and $Cp^*_2Sc(\kappa^2\text{-}OSi(OMe)_3)$ (**6b**) contain structural parameters that are similar to **1-4**. (Table 4.2) The Sc-O distance in **6a** is 1.97 Å, which is shorter than the Sc-O distance in **6b** (2.04 Å). The Sc-O-Si bond angle in **6a** is 160.7° which is smaller than the Sc-O-C or Sc-O-Si bond angle for **1-4**. The κ^2 structure has a smaller Sc-O-Si bond angle of 106.1° which is expected from scandium in a four-coordinate environment.

Table 4.2. Geometrical Parameters from DFT optimized structures of $Cp^*_2Sc–OR$.

Compound	Cp^*_a-Sc (Å)	Cp^*_b-Sc (Å)	Cp^*_a-Sc-Cp^*_b (°)	Sc-O (Å)	Cp^*_a-Sc-O (°)	Cp^*_b-Sc-O (°)	Sc-O-C (°)
2	2.23	2.23	135.0	1.94	111.9	113.1	175.5
1	2.22	2.23	134.3	1.98	111.4	114.4	172.3
3	2.21	2.22	134.4	2.02	111.5	114.1	175.4
4	2.21	2.21	137.8	1.96	110.2	112.0	174.0
6a	2.20	2.20	140.5	1.97	109.3	110.2	160.7
6b	2.24	2.24	138.4	2.04	106.9	109.0	106.1

The ^{45}Sc NMR parameters are calculated at the B3LYP/DZ level of theory in Amsterdam Density Functional[12] presented in Table 4.3 and agree well to the experimental values for **1-4**. The calculated C_Q values for **6a** and **6b** are -36.6 MHz and 25.8 MHz, respectively, which are close to the experimental values obtained for **5a** and **5b**. The smaller C_Q in the κ^2 (**5b**, **6b**) than in the κ^1 (**5a**, **6a**) is similar to the trend in the three-coordinate Cp^*_2Sc-X (X = F, Cl, Br, I) versus the four-coordinate Cp^*_2Sc-X(THF) discussed in Chapter 3. The decrease in C_Q is a consequence of scandium being in a more tetrahedral environment, resulting in π-overlap between fragment orbitals. This overlap is absent in solvent-free Cp^*_2Sc-X. The results suggest that the difference in C_Q between the **6a** and **6b** may arise from a similar consequence.

Table 4.3. Calculated NMR Parameters for **1-4** and **6**.

R	δ_{iso} (ppm)	C_Q (MHz)	η	Ω (ppm)	κ
1	81	-32.8	1.0	288	0.09
2	108	-31.2	0.75	395	0.06
3	139	-30.3	0.46	520	0.11
4	93	35.4	0.99	270	0.05
6a	90	-36.6	0.93	342	0.07
6b	48	25.8	0.84	238	0.70

The EFG tensors for **1-4** and **6a** and their orientations are similar shown in Figure 4.8. The magnitude of the C_Q is determined by V_{33} and is oriented perpendicular to the Sc-O bond and aligned with the LUMO of each compound for **1-4 and 5a**. The orientation of the EFG tensor in 6b is oriented along the Sc-O bond and correspond with the π*(Sc-O). The LUMO and EFG tensor orientation in **1-4** and **6a** are similar to Cp^*_2Sc-X, while the LUMO and EFG tensor orientation in **6b** is similar to Cp^*_2Sc-X(THF) (X = F, Cl, Br, I).

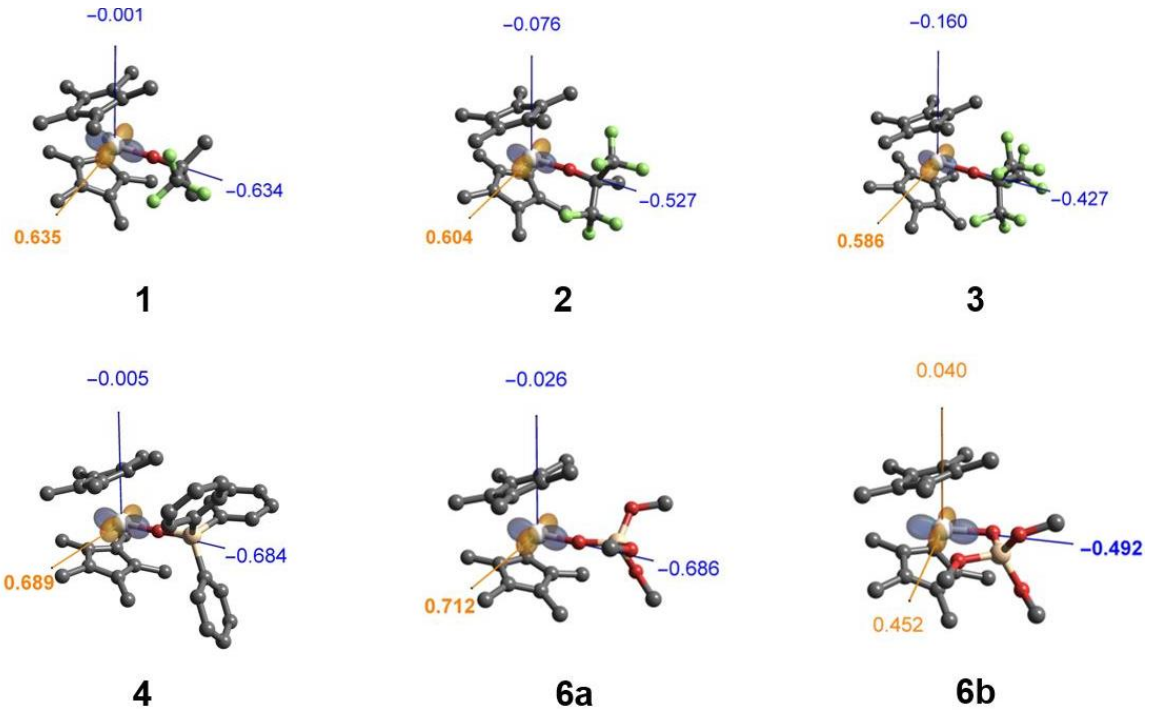

Figure 4.8 EFG tensor plots for 1-4, 6ab.

The natural localized molecular orbital (NLMO) decomposition of C_Q into individual orbital contributions provides an understanding of the ^{45}Sc C_Q for these compounds. Figure 4.9 shows that the major contributions to V_{33} are bonding orbitals

between scandium and the Cp* ligand as well as the σ- and π- bonding orbitals that describe the Sc-O bond. In 1-3, the scandium core orbitals contribute significantly to V_{33}. While filled orbitals are spherically symmetric and should have no contribution to V_{33}, the anisotropic distribution of charge in quadrupolar nuclei results in Sternheimer shielding.[13-14] Sternheimer shielding relates the anisotropic screening of nuclear charge by outer core orbitals from bonding partners and polarizability. The alkoxides also play a role in V_{33}, with electron-withdrawing alkoxide interactions with scandium (σ(Sc-O) (a_1)) contributing less to V_{33}.

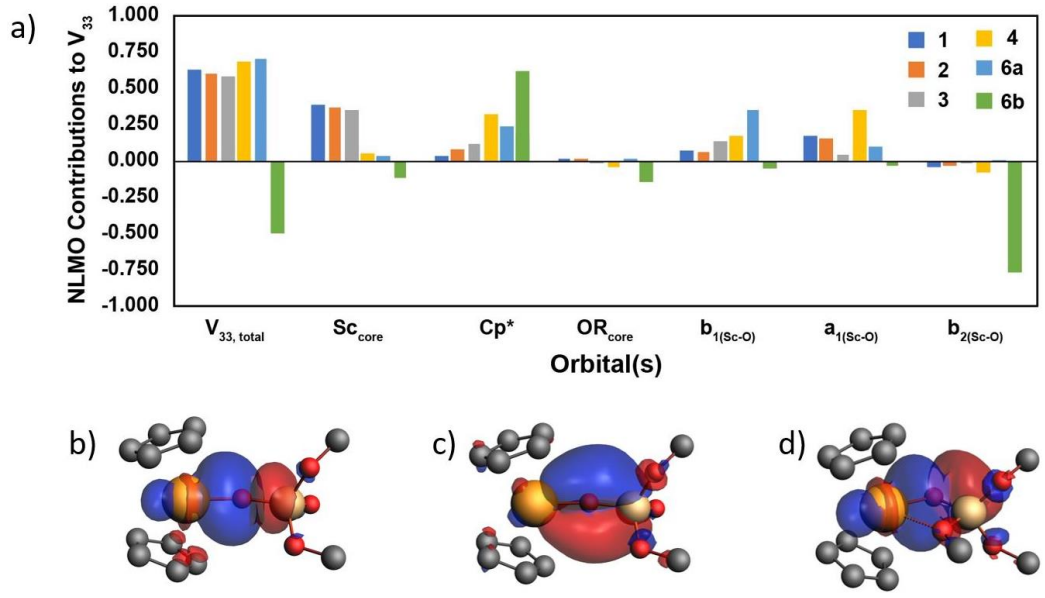

Figure 4.9. NLMO contributions to V_{33} for **1-4** and **6ab**.

Figure 4.9 shows that the major contributor to V_{33} for **4** and **6a** are closely related but are different than the contributions to V_{33} from **6b**. In **4** and **6a**¸ the major contributors are from the Cp*-Sc fragment and the σ(Si-O) and π(Si-O) (a_1 and b_1) bonding orbitals. However, the a_1 and b_1 orbitals in 6b are only minor contributors. Instead, the geometric

distortion leads to the b_2 orbital becoming the major contributor to V_{33} in **6b**. These results show that difference C_Q arises from the different bonding environments for κ^1 and κ^2 structures and that the geometric changes lead to different valence orbitals which affects the C_Q.

4.4 Conclusion

The reaction of Cp^*_2ScMe and $SiO_{2\text{-}700}$ form two species, $Cp^*_2ScOSi{\equiv}$(**5a**) and $Cp^*_2Sc(OSi{\equiv})O(SiO_x)_2$ (**5b**). The solid-state $^{45}Sc\{^1H\}$ NMR spectra of related compounds Cp^*_2Sc-OR (**1-4**), were important benchmarks that allowed for a comparison of C_Q in these permethylscandocene systems containing a single scandium-oxygen bond to **5a** and **5b**. DFT studies on small cluster models **6a** and **6b** for **5a** and **5b**, respectively, revealed the origin of the C_Q differences in **1-4** and **6ab**. The results show that the C_Q is sensitive to the primary coordination sphere on scandium and that quadrupolar solid-state NMR supplemented with computational chemistry can provide valuable information to surface-supported organometallic species.

4.5 Materials and Methods

General Considerations. All manipulations were performed under an inert atmosphere of dinitrogen or argon. Benzene-d_6 and cyclohexane-d_{12} were purchased from Cambridge Isotope Laboratories and dried over sodium/benzophenone, distilled under vacuum, and stored inside an inert atmosphere glovebox. Pentane and toluene were dried over sodium/benzophenone, degassed, and distilled under vacuum. Nonafluorotertbutanol, 1,1,1,-trifluoro-2-methyl-2-propanol, and 1,1,1,3,3,3-hexafluoro-2-methyl-2-propanol

were purchased from standard suppliers, dried over calcium hydride, and distilled under vacuum prior to use. Triphenylsilanol was sublimed under vacuum prior to use. Methyllithium in Et_2O was purchased from SigmaAldrich. Synthesis of Cp^*_2ScCl and Cp^*_2ScMe was reported previously.[15] Aerosil-200 was obtained from Degussa. Aerosil-200 dehydroxylated at 700 °C (SiO_{2-700}) was prepared by suspending the silica in excess water and drying the slurry under static air at 120 °C in an oven for 1 day. The resulting monolith was crushed and sieved to give 250−425 μM size silica aggregates. This material was loaded into a quartz tube containing an adapter with a Teflon stopcock to attach to a high vacuum line, placed in a tube furnace, heated under static air at 500 °C (5 °C min^{-1}) for 4 h, and placed under vacuum on a diffusion pump vacuum line for 12 h. While under vacuum, the temperature was increased to 700 °C (5 °C min^{-1}) and its temperature maintained for 4 h. After this time, the Teflon stopcock was sealed, and the tube was cooled to ambient temperature. The partially dehydroxylated silica was stored in an Ar filled glovebox and contains 0.26 mmol OH g^{-1}.

NMR Spectroscopy. Solution phase ^1H, $^{13}C\{^1H\}$, $^{19}F\{^1H\}$, and $^{45}Sc\{^1H\}$ NMR spectroscopy were acquired on a Bruker 300 Avance spectrometer, Varian 500, or Bruker 600 Avance spectrometer. ^1H and ^{13}C NMR spectra were referenced to the NMR solvent residual peak. ^{19}F NMR spectra were referenced to C_6F_6 (−163.9 ppm) external standard. ^{45}Sc NMR spectra were referenced to 0.11 M $ScCl_3$ in 0.1 M aqueous HCl solution (0.0 ppm).

Solid state NMR spectra were recorded in 4 mm zirconia rotors packed inside an inert atmosphere glovebox, and acquired on a Bruker 400 Avance III or a Bruker Neo-600

NMR spectrometer. The ^{13}C CPMAS NMR spectra were recorded with a 2 ms contact time and a 2 s relaxation delay. Static $^{45}Sc\{^{1}H\}$ NMR spectra were recorded with a Hahn-echo pulse sequence, with full echo detection ($\pi/2 - \tau - \pi -$ acq). Echo delays (τ) were 100−150 μs. All analytical simulations of solid-state spectra were performed in Topspin using Sola line shape analysis.

General Synthesis of Cp$_2$Sc−OR.* Cp*$_2$ScMe (200−500 mg, 0.6− 1.5 mmol) was dissolved in toluene (5−15 mL) and cooled to 0 °C. The alcohol (1.05−1.1 equiv) was added dropwise to the solution by syringe. After addition, the reaction was stirred at 0 °C for 10 min, then 20 min at room temperature. The volatiles were removed under vacuum, and a minimal amount of pentane was added by cannula to dissolve the residue. Recrystallization from pentane at −20 °C results in yellow crystals for compounds **1 − 3**. Yields and analytical data for the individual compounds are given below. The solid-state ^{45}Sc NMR data are given in below and summarized in Table 4.1. Results for C,H elemental analyses of **1−4** did not yield satisfactory results, possibly due to the sensitivity of these compounds.

Cp*$_2$Sc−OCMe$_2$CF$_3$ (**1**). Yield: 62%. ^{1}H NMR (C_6D_6, 300 MHz): δ 1.89 (s, 30 H, Cp*Me), 1.56 (q, 4 J_{HF} = 1 Hz, 6 H, OCMe$_2$CF$_3$). $^{13}C\{^{1}H\}$ NMR (C_6D_{12}, 151 MHz): 129.4 (q, 1 J_{CF} = 289 Hz, OCMe$_2$CF$_3$), 122.5 (CpMe), 78.7 (q, 2 J_{CF} = 27 Hz, CCF$_3$Me$_2$), 29.2 (OCMe$_2$CF$_3$), 12.6 (CpMe). $^{19}F\{^{1}H\}$ NMR (C_6D_6, 282 MHz): δ −82.0 (s). ^{45}Sc NMR (C_6D_6, 73 MHz): δ 70 (br,s).

Cp$_2$Sc−OCMe(CF$_3$)$_2$* (**2**). Yield: 10%. ^{1}H NMR (C_6D_6, 300 MHz): δ 1.83 (s, 30 H, Cp*Me), 1.78 (sept, 4 J_{HF} = 1.5 Hz, 6 H, OCMe(CF_3)$_2$). ^{13}C{^{1}H} NMR (C_6D_{12}, 126 MHz): 126.3 (q, 1 J_{CF} = 289 Hz, OCMe(CF_3)$_2$), 123.8 (Cp*Me), 82.9 (m, CCF_3Me_2), 23.2 (OCMe(CF_3)$_2$), 12.7 (bs, Cp*Me). ^{19}F{^{1}H} NMR (C_6D_6, 282 MHz): δ −77.5 (s). ^{45}Sc{^{1}H} NMR (C_6D_6, 73 MHz): δ 89. Cp*$_2$Sc−OC(CF_3)$_3$ (**3**). Yield: 26%. ^{1}H NMR (C_6D_6, 300 MHz): δ 1.79 (s, 30 H, Cp*Me). ^{13}C{^{1}H} NMR (C_6D_{12}, 151 MHz): δ 125.6 (s, Cp*Me), 123.7 (q, 1 J_{CF} = 295 Hz, OC(CF_3)$_3$), 86.6 (br m, OC(CF_3)$_3$), 12.4 (s, CpMe). ^{19}F{^{1}H} NMR (C_6D_6, 282 MHz): δ −73.2 (s). ^{45}Sc{^{1}H} NMR (C_6D_6, 73 MHz): δ 118 (br s).

Cp*$_2$Sc−OSiPh$_3$ (**4**). This compound was synthesized with a slight modification of the generally synthesis. Triphenylsilanol (1.05 equiv) was dissolved in toluene and added to Cp*$_2$ScMe by syringe. Yield: 48%. ^{1}H NMR (C_6D_6, 300 MHz): δ 7.28−7.31 (m, 6 H, ArH), 7.89− 7.92 (m, 9 H, ArH), 1.82 (s, 30 H, CpMe). ^{13}C{^{1}H} NMR (C_6D_6, 151 MHz): δ 142.1 (s, Ph), 137.2 (s, Ph), 129.7 (s, Ph), 128.3 (s, Ph), 122.7 (s, Cp*Me), 12.5 (s, Cp*Me). ^{45}Sc{^{1}H} NMR (C_6D_6, 73 MHz): δ 289 (br s).

*Synthesis of **5**.* SiO_{2-700} (0.2 g, 0.052 mmol OH) and Cp*$_2$ScMe (18 mg, 0.055 mmol) were loaded into a double Schlenk in an argon filled glovebox. The double Schlenk was connected to a high vacuum line, evacuated, and pentane (5 mL) was condensed onto the solids at 77 K. The slurry was warmed to room temperature and gently stirred for 1 h. Then the solution was filtered to the other arm of the double Schlenk. The derivatized silica was washed by condensing solvent from the other arm of the double Schlenk at 77 K, warming to room temperature, stirring for 2 min, and filtering the solvent back to the other side of the flask. This was repeated two times. The volatiles were transferred to a flask

containing a Teflon stopcock at 77 K. Analysis of the volatiles by gas chromatography shows that 0.23 mmol/g of CH_4 are released during the reaction. The pale yellow solid was dried under diffusion pump vacuum for 1 h and was stored in a glovebox freezer at −20 °C. Solid state NMR: ^{1}H MAS NMR (600 MHz): δ 2.9−2.5 (Cp*Me). 13C{^{1}H} CPMAS NMR (151 MHz): δ 121.5 (Cp*Me), 9.6 (Cp*Me); and ^{29}Si{^{1}H} CPMAS NMR (119 MHz): δ −106 (SiO_2) ppm. Elemental analysis for 5: C 5.61, H 0.49. ^{45}Sc NMR data are summarized in Table 4.1.

Computational Details. The geometries of **1−4**, **6a**, and **6b** were optimized with Gaussian 09 using the B3LYP functional and the 6- 311G** basis set on scandium and the 6-31G** basis set on all other atoms. Frequency calculations at the same level of theory produced no imaginary frequencies, indicating an energy minimum equilibrium structure. The NMR parameters of **1−4**, **6a**, and **6b** were modeled in the Amsterdam Density Functional suite of programs at the B3LYP/ DZ, Si(DZP) level of theory using the GIAO method. The calculated isotropic chemical shift was referenced to geometry-optimized $Sc(H2O)_6^{3+}$ at the same level of theory, which was used previously to reference ^{45}Sc chemical shift calculations.[6] Contributions of each natural localized molecular orbital (NLMO) to the C_Q were calculated at the same level of theory.[16] The EFG tensor plots were plotted using TensorView.[17]

4.6 References

[1] Handbook of Heterogeneous Catalysis, 1st ed.; *Wiley-VCH*, **1997**; p 2800.

[2] Kaphan, D. M.; Klet, R. C.; Perras, F. A.; Pruski, M.; Yang, C.; Kropf, A. J.; Delferro, M. *ACS Catal.* **2018**, *8*, 5363− 5373.

[3] Stalzer, M. M.; Nicholas, C. P.; Bhattacharyya, A.; Motta, A.; Delferro, M.; Marks, T. *J. Angew. Chem., Int. Ed.* **2016**, *55*, 5263−5267.

[4] Williams, L. A.; Marks, T. J. *ACS Catal.* **2011**, *1*, 238−245.

[5] Rodriguez, J.; Culver, D. B.; Conley, M. P. *J. Am. Chem. Soc.* **2019**, *141*, 1484−1488.

[6] Rossini, A. J.; Schurko, R. W. *J. Am. Chem. Soc*. **2006**, *128*, 10391−10402.

[7] Giovine, R.; Volkringer, C.; Ashbrook, S. E.; Trebosc, J.; McKay, D.; Loiseau, T.; Amoureux, J.-P.; Lafon, O.; Pourpoint, F. *Chem. - Eur. J.* **2017**, *23*, 9525−9534.

[8] Poater, A.; Solans-Monfort, X.; Clot, E.; Coperet, C.; Eisenstein, O. *J. Am. Chem. Soc.* **2007**, *129*, 8207−8216.

[9] Solans-Monfort, X.; Clot, E.; Coperet, C.; Eisenstein, O. *J. Am. Chem. Soc.* **2005**, *127*, 14015−14025.

[10] Estes, D. P.; Gordon, C. P.; Fedorov, A.; Liao, W. C.; Ehrhorn, H.; Bittner, C.; Zier, M. L.; Bockfeld, D.; Chan, K. W.; Eisenstein, O.; Raynaud, C.; Tamm, M.; Coperet, C. *J. Am. Chem. Soc.* **2017**, *139*, 17597− 17607

[11] Halbert, S.; Coperet, C.; Raynaud, C.; Eisenstein, O.; *J. Am. Chem. Soc.* **2016**, *138*, 2261−2272.

[12] te Velde, G.; Bickelhaupt, F. M.; Baerends, E. J.; Guerra, C. F.; van Gisbergen, S. J. A.; Snijders, J. G.; Ziegler, T. *J. Comp. Chem.* **2001**, *22*, 931.

[13] Lucken, E. A. C. Nuclear Quadrupole Coupling Constants; Academic Press, **1969**.

[14] Autschbach, J.; Zheng, S.; Schurko, R. W. *Concepts Magn. Reson., Part A* **2010**, *36A*, 84−126.

[15] Thompson, M. E.; Baxter, S. M.; Bulls, A. R.; Burger, B. J.; Nolan, M. C.; Santarsiero, B. D.; Schaefer, W. P.; Bercaw, J. E. *J. Am. Chem. Soc.* **1987**, *109*, 203-219.

[16] Srebro, M.; Autschbach, J. *Chem. Eur. J.* **2013**, *19*, 12018-12033.

[17] Young, R. P.; Lewis, C. R.; Yang, C.; Wang, Y. L.; Harper, J. K.; Mueller, L. J. *Magn. Res.Chem.* **2019**, *57*, 211-223.

CHAPTER 5

Solid-state ^{11}B NMR Studies of Coinage Metal Complexes Containing a Phosphine Substituted Diboraanthracene Ligand

5.1 Abstract:

Transition metal interactions with Lewis acids are fundamentally interesting, since metals by nature are also Lewis acids. The most common Lewis acid Z-type ligands contain boron, which contains the quadrupolar NMR active ^{11}B nucleus. The $^{11}B\{^1H\}$ NMR spectra of copper, silver, and gold complexes coordinated to the phosphine substituted 9,10-diboraanthracene ligand (B_2P_2) contain planar boron centers and weak M→BR_3 interactions. These compounds are $[(B_2P_2)M][BAr^F{}_4]$ (M = Cu (**1**), Ag(**2**), Au(**3**)) and are characterized by large quadrupolar coupling constants (C_Q ~ 4.4 – 4.7 MHz) and large span (Ω) values (93 – 139 ppm). In contrast, the solid-state $^{11}B\{^1H\}$ NMR spectrum of $K^+[Au(B_2P_2)]^-$ (**4**) contains tetrahedral boron environments and a narrower signal, characterized by small C_Q and Ω values. The DFT analyses of **1-4** shows that the C_Q and Ω are large for planar boron and are small for tetrahedral boron environments. These results show that solid-state $^{11}B\{^1H\}$ provides valuable spectroscopic information to characterize the presence of the M→B interaction.

5.2 Introduction:

The vast majority of transition metal chemistry is dominated by Lewis acid-base interactions, where the metal often serves as a Lewis acid and its ligands serve as a Lewis base. However, bonding environments where the transition metal serves as a Lewis base

have been known since the 1960s,[1-2] and since then, transition metal complexes featuring these Z-type ligands have been synthesized and characterized.[3-5] While an unsupported M→BR_3 has not yet been achieved, ligands containing a chelating borane backbone have been isolated. Examples of these include transition metal complexes containing tris(methimazolyl)borane, phosphinoborane, diphosphinoborane, and triphosphinoborane ligands.[6-10] (Figure 5.1a) These compounds contain short M-B distances and a pyramidalized boron ($\Sigma_{C\text{-}B\text{-}C} < 360^o$). However, the "soft" nature of the M → BR_3 interaction can complicate its structural analysis; for example, the X-ray crystal structure of a copper complex of a diphosphino ligand containing a borane chelate contains four independent molecules, with Cu-B varying by more than 0.1 Å.[11]

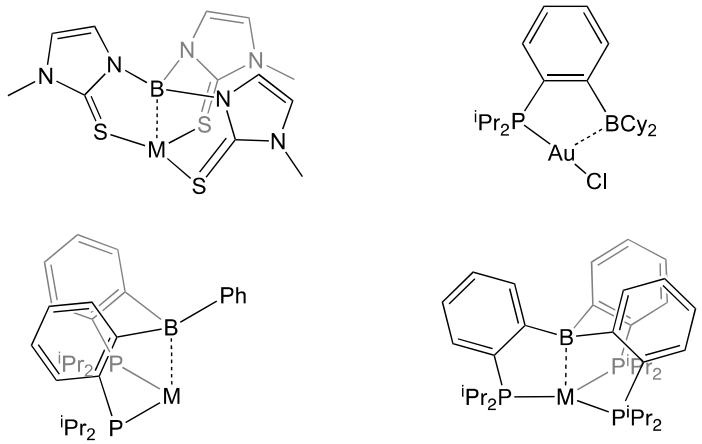

Figure 5.1. Selected transition metal compounds that contain Z-type ligands.

Borane complexes contain the NMR active ^{11}B nucleus (8.584 x 10^7 rad T^{-1} s^{-1}), which can serve as a spectroscopic handle for investigating these interactions. The $^{11}B\{^1H\}$ signals of molecules containing a M→BR_3 interaction appear within values associated with tetrahedral boron, which are generally more shielded than the free BR_3 ligand.[8,12-14] The

differences in shielding in these boron environments can be related to the orientation of the CST and the occupation of the orbitals related to chemical shielding. Figure 5.2 illustrates how the difference in geometry influences the shielding of the boron nucleus. In these molecules, the HOMO is coupled to the LUMO through the angular momentum operator, and the interaction is strongest for the planar boron than the tetrahedral boron. As a result, the planar boron nucleus is more deshielded than the tetrahedral boron.

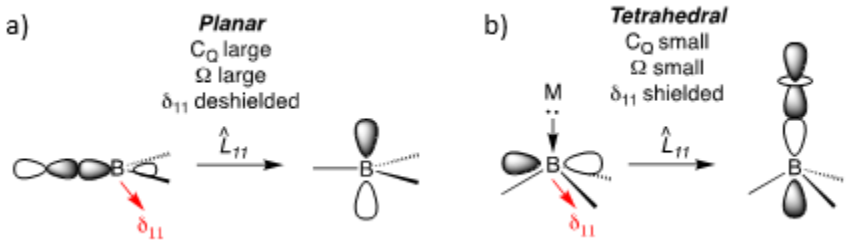

Figure 5.2 Predictions for main orbital responsible for deshielding in tricoordinate (a) and tetracoordinate boron (b) proposed in ref. 15.

Solid-state $^{11}B\{^1H\}$ NMR spectra often contain broad powder patterns as a result of the coupling of the electric field gradient (EFG) to the quadrupolar boron nucleus. Planar compounds such as Mes_3B (Mes = mesityl) contain a C_Q that is larger (4.8 MHz) compared to those of boronic acids or hexagonal boron nitrides (C_Q ~ 2.8 MHz) but smaller than that of two coordinate Mes_2B^+ (5.4 MHz).[16] In comparison, these C_Q values are all significantly larger than the tetrahedral boron environment that is observed in BO_4 sites of boron oxide (~ 0.4 MHz).[17]

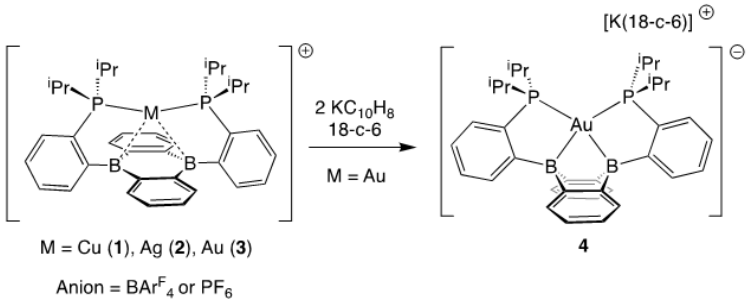

Figure 5.3 Coinage metal complexes of B_2P_2 and the reduction of **3** to **4**.

The phosphine substituted 9,10 diboranthracene ligand B_2P_2 in Figure 5.3 is an example of a Z-type ligand that reacts with coinage metals to form stable complexes of $[M(B_2P_2)][BAr^F{}_4]$.[18-19] $[M(B_2P_2)][BAr^F{}_4]$ (M = Cu(**1**), Ag(**2**), Au (**3**)) contain trigonal planar boron centers, as evidenced from X-ray crystal structures that contain $\sum_{C-B-C} \approx 360^o$. In contrast, reduction of 3 with 2 equiv. of potassium napthalenide results in [K(18-c-6)][Au(B_2P_2)] (**4)** that results in pyramidalization at boron ($\sum_{C-B-C} \approx 360^o$).

5.3 Results and Discussion

The static $^{11}B\{^1H\}$ NMR spectra of B_2P_2 is shown in Figure 5.4 and contains two sites. The NMR parameters extracted from the simulation of both sites are in Table 5.1, with the most notable differences between $\delta(^{11}B)$ and $C_Q(^{11}B)$ in site 1 and site 2. Site 1 features a deshielded boron nucleus at 63 ppm with a larger C_Q of 4.8 MHz, and site 2 features a more shielded boron nucleus at 9ppm with a smaller C_Q of 2.9 MHz. In contrast, the room temperature C_6D_6 solution spectrum of B_2P_2 contains only a single signal at 34ppm, which is near the average of the two peaks observed in the solid state. The presence of two signals in the solid state suggests that the $R_3P \rightarrow BR_3$ interactions are fluxional on

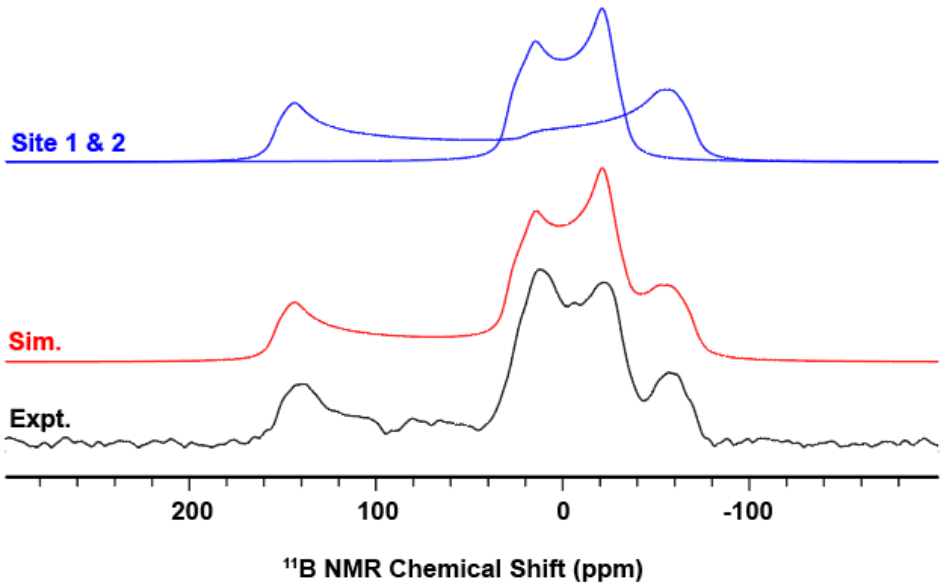

Figure 5.4. Static $^{11}B\{^{1}H\}$ NMR spectra of B_2P_2 acquired at 9.4 T. Experimental spectra are in black and the sum of the two simulated sites (blue) are in red.

Table 5.1. $^{11}B\{^{1}H\}$ NMR data extracted from solid-state NMR measurements of **B_2P_2**.[a]

	Site-1	**Site-2**
δ (ppm)[b]	63	9
C_Q (MHz)	4.8	2.9
η	0.05	0.02
Ω (ppm)	77	35
κ	0.6	-0.2
δ_{11}	93	28
δ_{22}	78	7
δ_{33}	17	-7
α	122	15
β	4	175
γ	272	200

[a] – data shown in the table are averages from simulations from data acquired at 9.4 T and 14.1 T

[b] – ^{11}B NMR chemical shift in C_6D_6 solution is 34 ppm, see ref 19.

the NMR time scale in solution but not in the solid state. This phenomenon was recently observed in a tri-phosphinoborane ligand.[20] The deshielded boron with a large C_Q for site 1 can be attributed to a planar tri-coordinate boron. In contrast, the shielded boron peak with a small C_Q for site 2 suggests that it is a distorted tetrahedral boron containing a $R_3P \rightarrow BR_3$ interaction.

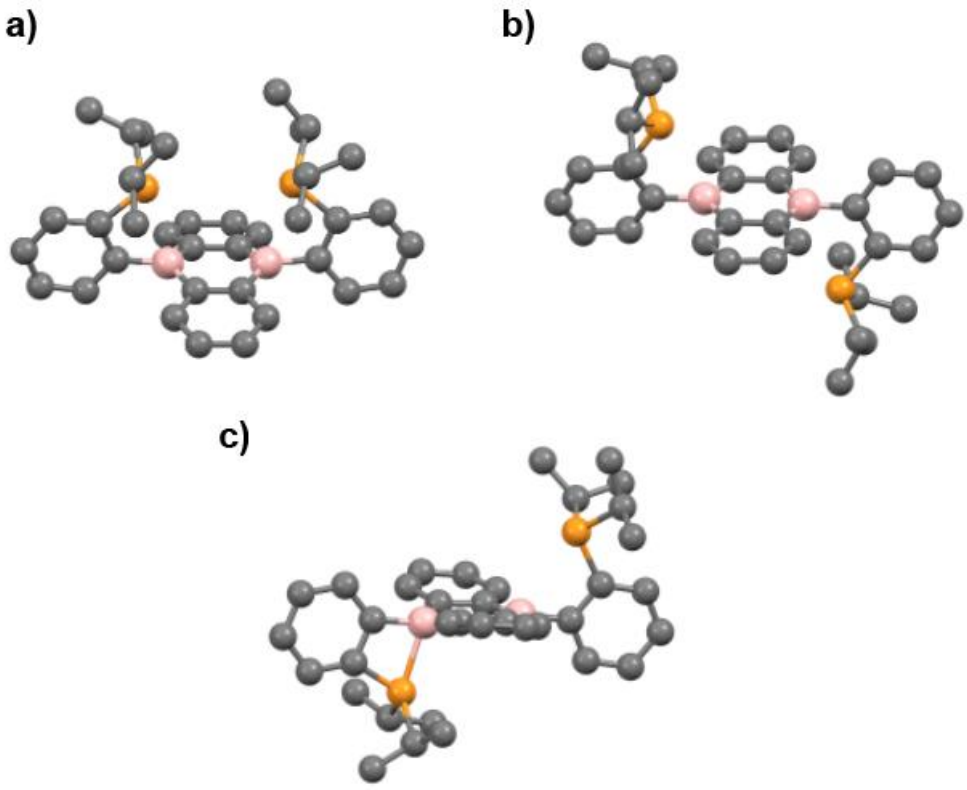

Figure 5.5 Calculated structures of *syn*-B_2P_2 (a), *anti*-B_2P_2-**1** which lacks a $R_3P \rightarrow BR_3$ interaction (b), and *anti*-B_2P_2-**2** which contains a $R_3P \rightarrow BR_3$ interaction.

The geometries of B_2P_2 were optimized in Gaussian 09 with the PBE functional and the 6-31G(d,p) basis set for both the *syn*- and *anti*- conformations. (Figure 5.5). The relative energies are *syn*-B_2P_2 (0.0 kcal mol $^{-1}$), *anti*-B_2P_2-**1** (3.6 kcal mol $^{-1}$), and

anti-B_2P_2-**2** (3.0 kcal mol $^{-1}$). The *anti*-B_2P_2-**1** lacks the secondary $R_3P \rightarrow BR_3$ interaction, and *anti*-B_2P_2-**2** contains the secondary $R_3P \rightarrow BR_3$ interaction. The B-P distance in *syn*-B_2P_2 is 2.80 Å, and in *anti*-B_2P_2-**1** are 3.01 Å and 3.08 Å. These distances are longer than the sum of the covalent radii (1.91 Å), and both molecules contain $\Sigma_{\angle C-B-C}$ that is ≈ 360º. These structural parameters suggest indicate that the boron is planar, and there are no significant $R_3P \rightarrow BR_3$interactions. In contrast, *anti*-B_2P_2-**2** contains one planar boron ($\sum_{C-B-C} = 360^o$) with a long B-P distance (3.06 Å) and one distorted tetrahedral boron ($\sum_{C-B-C} = 354^o$) with a short B-P distance (2.25 Å) and a $R_3P \rightarrow BR_3$ interaction. This conformer is 0.61 kcal mol^{-1} more stable than anti-B_2P_2-**1** – which lacks a $R_3P \rightarrow BR_3$ interaction – at this level of theory.

The solid-state ^{11}B NMR spectra of B_2P_2 contains a trigonal planar boron with a large C_Q value of 4.7-4.9 MHz and a large span value of 85-105 ppm. In contrast, the distorted tetrahedral boron in B_2P_2 is characterized by a significantly smaller C_Q of 2.8 MHz and a Ω of 33 ppm. The ^{11}B parameters for *syn*-B_2P_2, *anti*-B_2P_2-**1**, and *anti*-B_2P_2-**2** are calculated at the PBE/QZ4P(B)/DZ(P,C,H) level of theory and provided in Table 5.2. The calculated ^{11}B NMR parameters in *anti*-B_2P_2-**1** contains two borons with large C_Q values and that lack significant $R_3P \rightarrow BR_3$ interactions. In contrast, those for *anti*-B_2P_2-**2** contain two distinct boron C_Q with a large (4.77 MHz) and small (3.26 MHz) value that agree with those obtained experimentally. Additionally, the calculated Ω are 102 ppm for the large C_Q site and 38 ppm for the small C_Q site, which agree with experimental trends. These results show that the solid-state ^{11}B parameters are sensitive to the minor perturbations to the coordination environment around boron.

Table 5.2. Calculated $^{11}B\{^1H\}$ NMR data for the structures of **B_2P_2** shown in Figure 5.5.[a]

	syn-B_2P_2	*anti*-B_2P_2-**1**	*anti*-B_2P_2-**2**[b]	*anti*-B_2P_2-**2**[c]
δ (ppm)	47	56	55	9
C_Q (MHz)	4.7	4.9	4.77	3.26
η	0.07	0.06	0.07	0.13
Ω (ppm)	96	105	102	38
κ	0.2	0.2	0.24	0.22
δ_{11}	92	105	102	26
δ_{22}	53	63	63	12
δ_{33}	-4	0	0	-11
α	90	80	90	85
β	163	4	163	12
γ	270	275	281	272

[a] – Individual boron sites have slightly different NMR parameters, where they differ averages are given; [b] – values for the planar boron for the *anti*-B_2P_2-**2** shown in Figure 5.5c; [c] – values for the distorted tetrahedral boron for the *anti*-B_2P_2-**2** shown in Figure 5.5c.

The solid-state $^{11}B\{^1H\}$ NMR spectra obtained at 9.1T and 14.1 T for cationic $[M(B_2P_2)][B(Ar^F)_4]$ (M = Cu, Ag, Au) **1-3** are similar. (Figure 5.6-5.7, page 85-86) Each show two ^{11}B resonances: one broad signal which is indicative of a nearly planar boron and one narrow signal from the tetrahedral $[B(Ar^F)_4]$ anion at -11 ppm. These results are consistent with the X-ray crystal structures of **1-3**, which show that the environment around boron is planar in these structures.[18-19]

The ^{11}B NMR parameters extracted from simulations at both 14.1T and 9.1T are provided in Table 5.3 (page 86). The chemical shifts in the solid-state are noticeably more downfield than when measured in the CD_3CN solution and increase from **1** < **2** < **3**. This may be attributed to the coordination of CD_3CN to the diboraantracene ligand. However, the solid-state $\delta(^{11}B)$ values are uniformly higher than the solution-state $\delta(^{11}B)$ values.

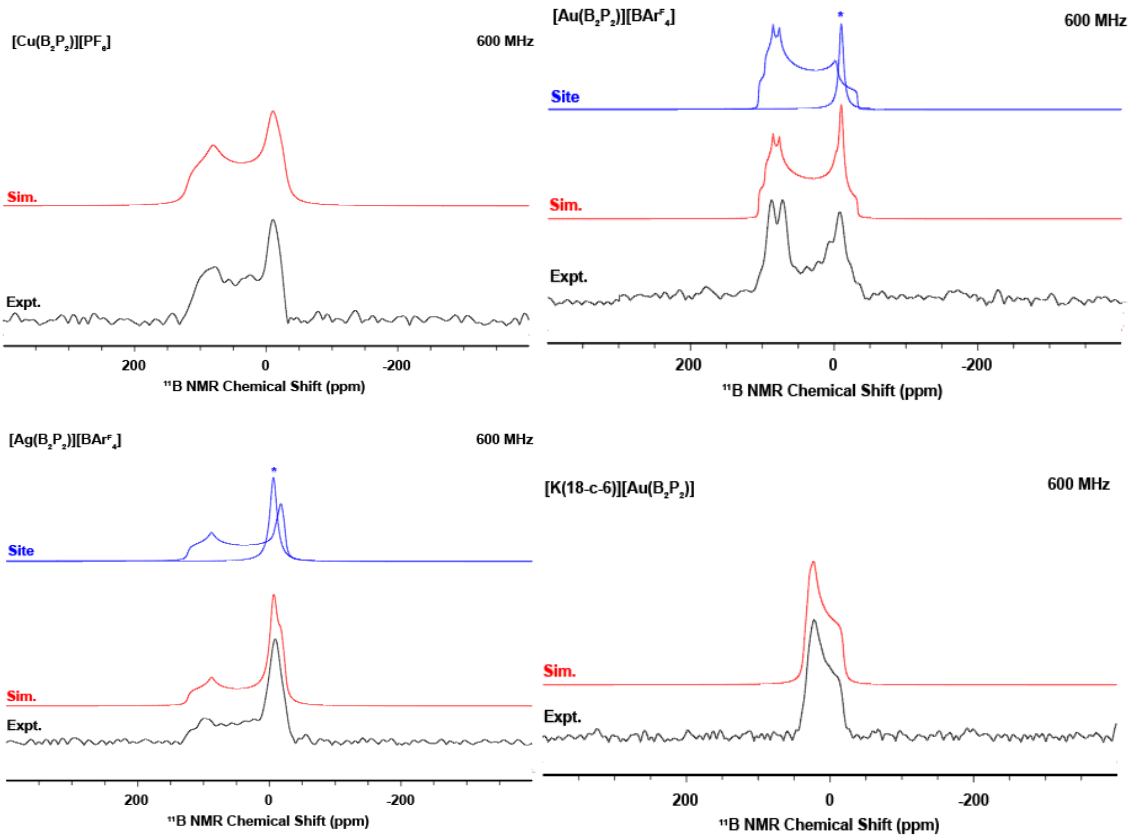

Figure 5.6 Solid-state $^{11}B\{^{1}H\}$ NMR spectra for **1-4** obtained at 14.1 T. * refers to $[\mathbf{B}ArF_4]^-$. Experimental spectra are in black, simulated spectra (red) are the sum of individual sites that are simulated in blue.

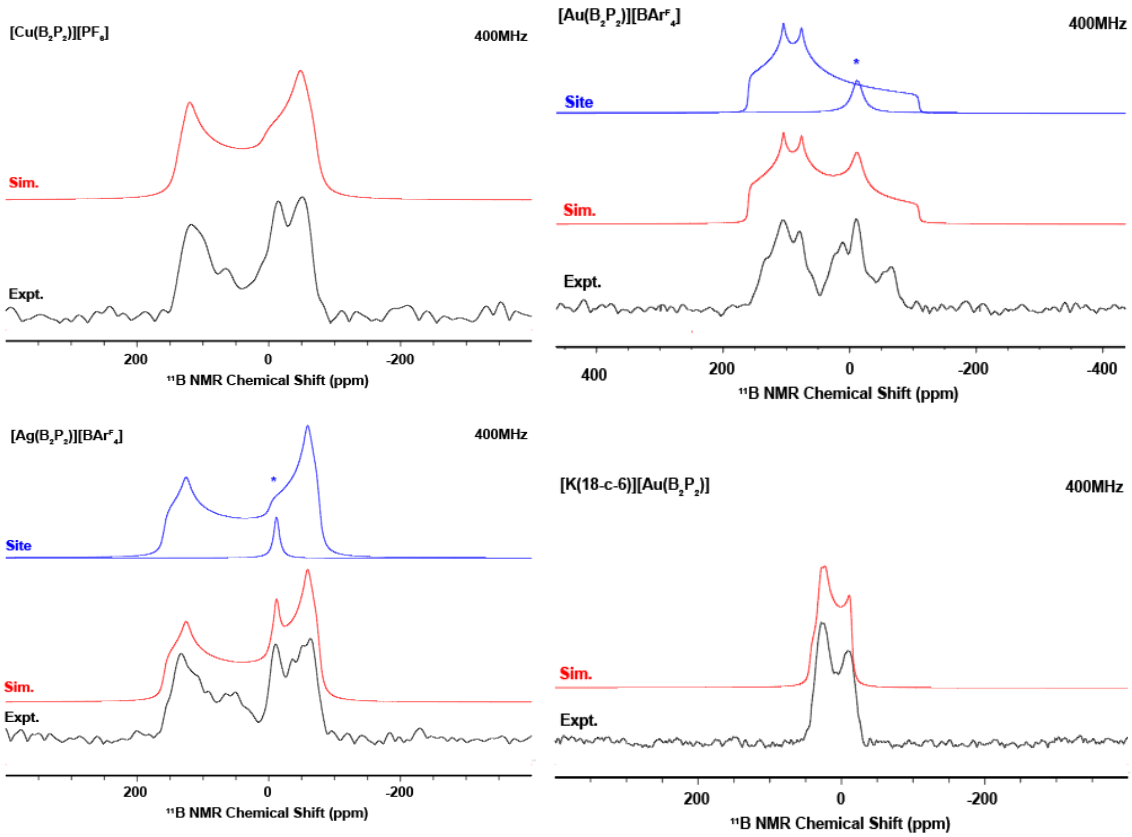

Figure 5.7 Solid-state $^{11}B\{^{1}H\}$ NMR spectra for **1-4** obtained at 9.1 T. * refers to [**B**ArF$_4$]$^-$. Experimental spectra are in black, simulated spectra (red) are the sum of individual sites that are simulated in blue.

Table 5.3. $^{11}B\{^{1}H\}$ NMR data extracted from solid-state NMR measurements of **1** – **4**.[a]

	1	**2**	**3**	**4**
δ (ppm)[b]	27[c]	29[d]	32[c]	11[e]
δ (ppm)[f]	51[g]	55	66	15
C_Q (MHz)	4.4	4.4	4.7	1.5
η	0.2	0.04	0.03	0.2
Ω (ppm)	93	105	139	56
κ	0.3	0.3	0.2	0.7
δ_{11}	93	102	131	36
δ_{22}	60	66	75	28
δ_{33}	-0.2	-3	-8	-20
α	180	275	178	60
β	0	180	126	90
γ	90	91	40	180

The $^{11}B\{^1H\}$ NMR spectra of **1-3** are consistent with a planar boron site in the B_2P_2 fragment with minimal interaction with the coinage metal. In these complexes, the C_Q (4.4 - 4.7 MHz) and Ω (93-139 ppm) values are both large and similar compared to the planar boron site in B_2P_2 (C_Q = 4.8 MHz, 77 ppm). In contrast, the $^{11}B\{^1H\}$ NMR spectrum of **4** is significantly different from **1-3**. This spectrum contains boron with $\delta(^{11}B)$ = 15ppm, a smaller C_Q of 1.5 MHz, and a smaller Ω of 56 ppm. These results are consistent with the expected M→BR_3 interaction in **4** that is also noticeable in the X-ray crystal structure. The data also indicate that the origin of the ^{11}B NMR properties is similar for **1-3** but different for **4**.

The geometries of **1-4** were optimized with Gaussian 09 using the PBE functional and SDD functional. The SDD basis set was used on the metal, and the 6-31G(d,p) basis set was used on all other atoms. This level of theory reproduces key structural parameters that are observed in the X-ray crystal structure. (Table 5.4-5.5) The NMR parameters were calculated in Amsterdam Density Functional with the PBE functional, the QZ4P basis set on boron, the TZ2P basis set on the metal, and the DZP basis set on all other atoms. (Table 5.6) The calculated ^{11}B NMR chemical shifts are shifted ~10 ppm more shielded than the experimental values. However, the C_Q and Ω values agree well with experimental trends. For **1-3**, the calculated C_Q are between 4.3 – 4.6 MHz and the calculated Ω are between 109 and 119 ppm and agrees with experimental data that Ω increases from **1** < **2** < **3**. The calculated ^{11}B NMR parameters for **4** also reveal a significantly smaller C_Q of 1.8 MHz and a smaller Ω of 58 ppm.

Table 5.4. Crystal structure parameters for $M[B_2P_2]^{+/-}$ compounds in Angstroms.

Crystal Structure	M-B1	M-B2	M-B avg	M-P1	M-P2	M-P avg	M-B-P	M-B-P	M-B-P avg
$[Cu(B_2P_2)]^+$ $[PF_6]^-$	2.33	2.36	**2.35**	2.28	2.29	2.29	78.18	78.64	78.41
$[Cu(B_2P_2)]^+$ $[BAr^F{}_4]^-$	2.34	2.40	**2.37**	2.30	2.29	2.29	77.47	78.54	78.01
$[Ag(B_2P_2)]^+$ $[BAr^F{}_4]^-$	2.54	2.59	**2.57**	2.42	2.41	2.41	75.33	76.37	75.85
$[Au(B_2P_2)]^+$ $[BAr^F{}_4]^-$	2.68	2.61	**2.64**	2.34	2.33	2.33	74.63	75.90	75.27
$[Au(B_2P_2)]^-$ $[K(18\text{-}c\text{-}6)]^+$	2.24	2.24	**2.24**	2.38	2.37	2.38	84.54	84.99	84.77

Table 5.5. DFT calculated parameters for $M[B_2P_2]^{+/-}$ compounds in Angstroms.

PBE/M(SDD)	M-B1	M-B2	M-B avg	M-P1	M-P2	M-P avg	M-B-P	M-B-P	M-B-P avg
$[Cu(B_2P_2)]^+$	2.37	2.36	**2.37**	2.33	2.33	2.33	78.14	78.18	78.16
$[Ag(B_2P_2)]^+$	2.56	2.56	**2.56**	2.45	2.45	2.45	76.18	76.16	76.17
$[Au(B_2P_2)]^+$	2.71	2.71	**2.71**	2.39	2.39	2.39	74.83	74.83	74.83
$[Au(B_2P_2)]^-$	2.27	2.27	**2.27**	2.48	2.48	2.48	84.24	84.25	84.25

Table 5.6. Calculated $^{11}B\{^1H\}$ NMR parameters for **1** – **4**

	1	**2**	**3**	**4**
δ (ppm)	41	47	49	5
C_Q (MHz)	4.3	4.5	4.6	1.8
η	0.02	0.03	0.05	0.2
Ω (ppm)	109	116	119	56
κ	0.7	0.1	0.1	0.2
δ_{11}	94	103	106	31
δ_{22}	44	51	53	9
δ_{33}	-15	-13	-13	-25
α	118	255	278	88
β	4	151	148	89
γ	85	90	89	102

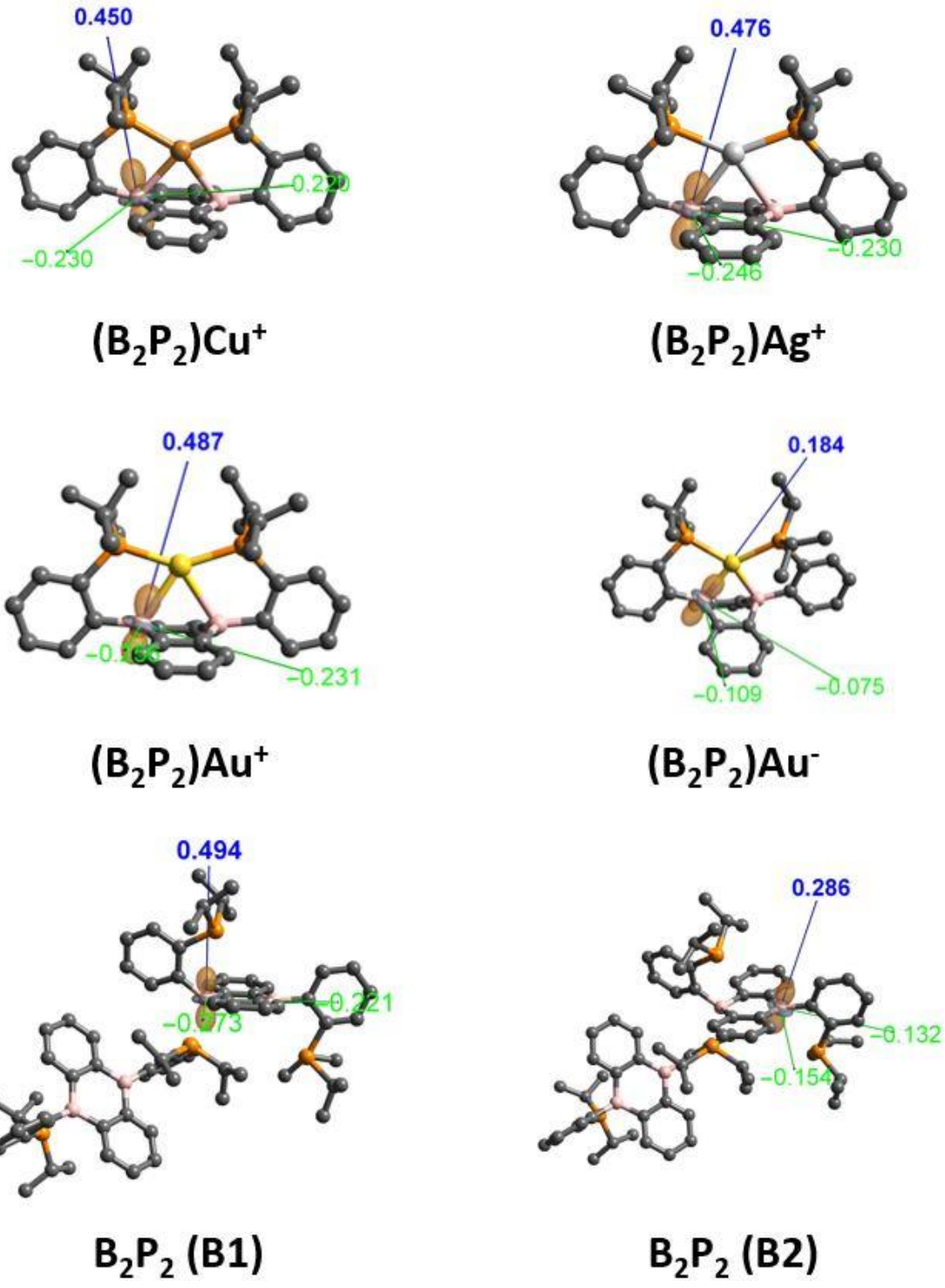

Figure 5.8 Calculated EFG tensor plots of **1-4** and B_2P_2 in TensorView 1.4.

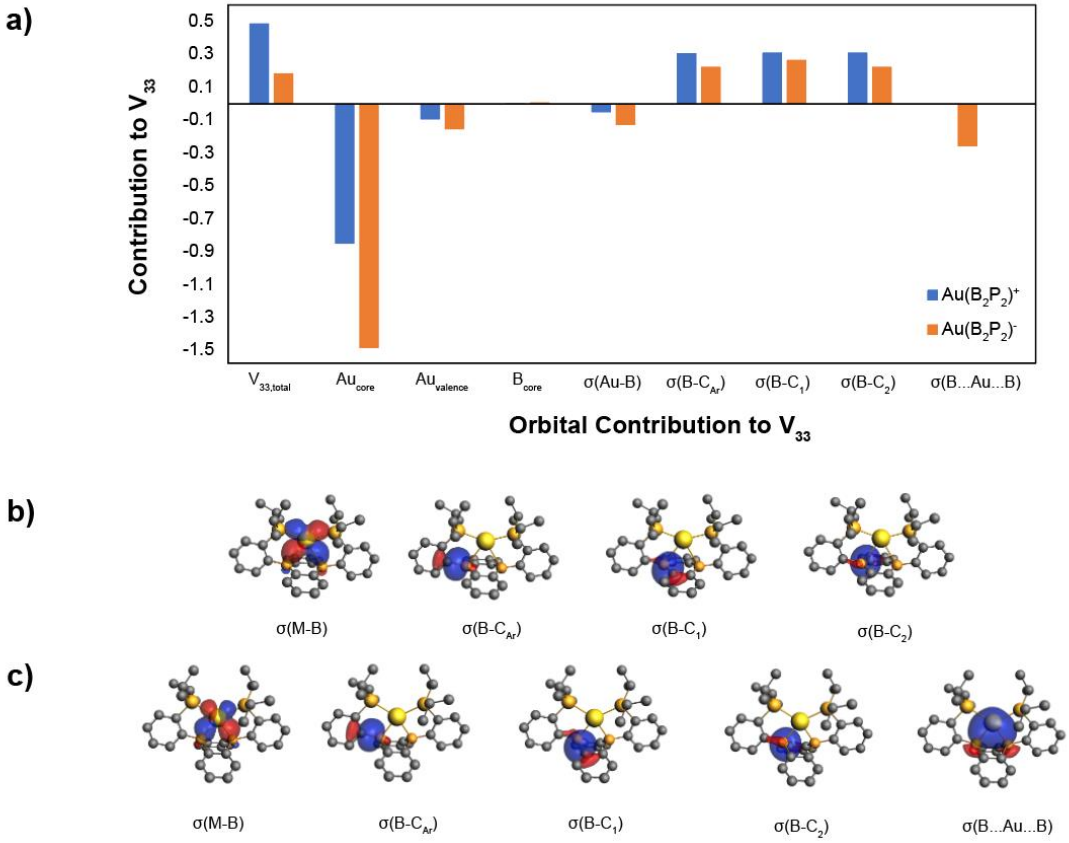

Figure 5.9. NLMO contributions to V_{33} in **3** (blue) and **4** (orange) (a). Plots of NLMOs for **3** (b) and **4** (c) with isovalue = 0.03.

The EFG tensors for **1-3** are oriented perpendicular to the plane defined by the three B-C bonds, while the EFG tensor of **4** is oriented along the B-Au axis. (Figure 5.8) Figure 5.9 shows the natural localized molecular orbital (NLMO) contributions to V_{33} for **3** and **4**. The largest differences are that the metal core orbitals, significantly reduce the C_Q in the order $Cu^+ < Ag^+ < Au^+ < Au^-$. (Figure 5.9a-5.10) This decrease is expected from Sternheimer shielding, which increases down the period as the metal becomes more polarizable. A larger negative V_{33} contribution is present in **4** for σ(B…M…B), which is

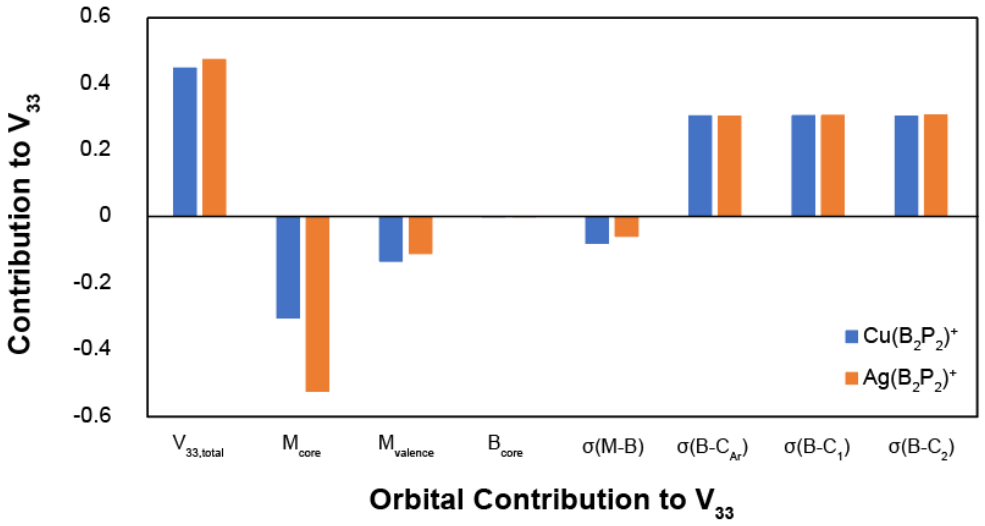

Figure 5.10. NLMO contributions to V_{33} for **1** and **2**.

expected for the presence of extra electron density for an Au-B interaction. In **3** and **4**, all three σ(B-C) bonds contribute to V_{33}, with slightly larger contributions for **3** than **4**. The NLMOs that describe the bonding between gold and boron are shown in Figure 5.9b-c for both **3** and **4**. While there is noticeably larger negative contribution for the σ(B…Au…B) orbital for **3** and **4**, both show an orbital that is highly localized on gold than on boron. The 3c-2e interaction present in **4** significantly reduces the V_{33}. The results show that the smaller C_Q value in **4** can be attributed to the Au→BR_3 interaction.

The ^{11}B chemical shielding tensors (CST) for **3** and **4** are shown in Figure 5.11. The CST of **3** is more anisotropic than in **4**. The δ_{11} component of the CST that is responsible for the difference in shielding is oriented perpendicular to the B-C_{aryl} bond in **3** and **4** and lies along the plane defined by the diboraantracene ring. (Figure 5.11c) The NLMO contributions to the CST show that the σ(B-C_{aryl}) is the largest contributor to the paramagnetic chemical shielding in **3** and **4** (Figure 5.11d,e). Despite the similar orientation

of the CST in **3** and **4**, the magnitude of shielding is very different. In **3**, the orbital rotation model for $\hat{L}_{11}$ couples the σ(B-C_{aryl}) orbital to the π*(dπ$_{Au}$ → p_B). In **4**, though, the σ(B-C_{aryl}) orbital is coupled to the 3c-2e σ*(B…Au…B) orbital. These results show that the ^{11}B NMR chemical shift is related to the coupling of the NLMOs for each Au → BR_3 interaction and is different for **3** and **4**.

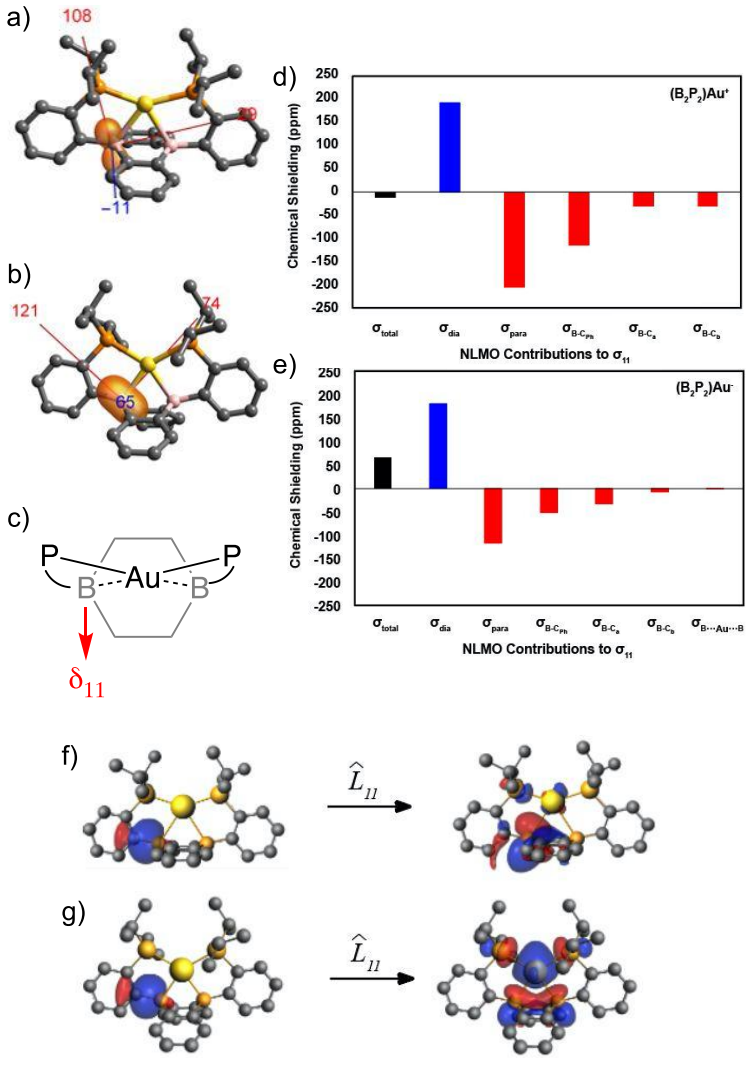

Figure 5.11. CST plots of **3** (a) and **4** (b) in Tensorview and the orientation of δ_{11} in these compounds. The NLMO decomposition for **3** (d) and **4** (e) responsible for deshielding and the orbitals responsible in **3** (f) and **4** (g) are displayed with isovalue = 0.03.

The greater deshielding in **3** compared to **4** can be understood from a qualitative molecular orbital diagram. (Figure 5.12) In **3**, the σ(B-C_{aryl}) and π*(dπ_{Au} → p_B) are orthogonal, similar to the planar boron model shown in Figure 5.2. In **4**, the addition of two electrons populates the σ(B…Au…B) orbital, and the consequence of this electronic perturbation couples the σ(B-C_{aryl}) instead to the 3c-2e σ*(B…Au…B).

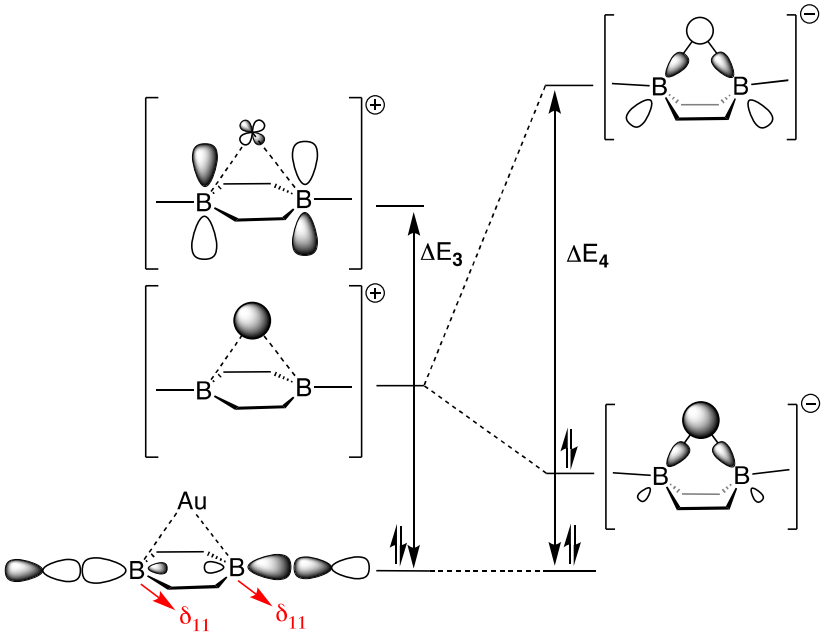

Figure 5.12 Qualitative molecular orbital diagram containing the orbitals that relate to deshielding in **3** (right) and **4** (left).

As shown above, the difference in the C_Q shielding for **3** and **4** can be explained by the strength of the Au → BR_3 interaction. The second order perturbation for delocalization of dπ_{Au} → p_B at this level of theory is 3.7 kcal/mol per boron, indicating that the Au → BR_3 interaction in **3** is weak. For comparison, the M→BR_3 value is 2.8 kcal/mol in **1** and 3.4 kcal/mol in **2**. In 4, this delocalization increases significantly to 14.8 kcal/mol per boron. The NLMO contributors for dπ_{Au} → p_B interaction is localized on gold [93% Au (100% d);

2% per B (3% s, 97% p)] in **3**. The NLMO contributors for the 3c-2e σ(B…Au…B) interaction is more evenly distributed [33% Au (97% s, 3% d); 28% per B (13% s, 87% p)] and as a result reduces both the C_Q and the σ^p.

5.4 Conclusion

The planar boron environments in **1-3** and long M…B distances result in large C_Q and Ω values. In contrast, the tetrahedral boron environments in **4** and short M…B distances result in smaller C_Q and Ω values. The DFT data for **1-3** show that the Z-type bonding M → BR_3 is minimal, but there are still slight reductions in the C_Q in relation to the planar boron in the free B_2P_2 ligand. The addition of two electrons to **3** generates **4**, and the addition of a 3c-2e interaction results in smaller C_Q and Ω values that are characteristic of tetrahedral boron environments. The origin of the C_Q and CST is studied by calculating the contribution of each NLMO to V_{33} and σ_{11}. The ^{11}B NMR differences observed in **1-4** validate models for the ^{11}B chemical shift analysis that commonly describe M → BR_3 complexes. While the CQ for boron is not commonly reported because $^{11}B\{^1H\}$ NMR spectra are often acquired in solution, this study illustrates that the use of solid-state ^{11}B NMR can help decipher the absence or presence of a M→BR_3 interaction.

5.5 Materials and Methods

1 – 4 were reported previously.[18-19] Solid state NMR spectra were recorded in 4 mm zirconia rotors packed inside an inert atmosphere glovebox, and acquired on a Bruker 400 Avance III or a Bruker Neo-600 NMR spectrometer. Static $^{11}B\{^1H\}$ NMR spectra were recorded with a Hahn-echo pulse sequence, with full echo detection ($\pi/2 - \tau - \pi -$ acq) and

referenced to solid $NaBH_4$ (δ = -42.06 ppm). The $\pi/2$ pulse length for $NaBH_4$ was 6 μsec (ν_{rf} = 41.67 kHz), and a "solid $\pi/2$ pulse" (e.g. 6μsec/(I + ½) = 3 μsec for I = 3/2 for ^{11}B). Echo delays (τ) were 100 – 250 μsec, and recycle delays were 250 μsec – 1 sec. All analytical simulations of solid-state spectra were performed in Topspin using Sola line shape analysis.

The geometries of all structures were optimized in Gaussian 09[21] using the PBE functional at the 6-31G(d,p) level of theory for H, B, C, and P. Copper, silver, and gold were described with the SDD basis set. The NMR parameters are calculated the Amsterdam Density Functional (ADF) suite,64 using the GIAO method[22323] with the PBE functional, QZ4P basis set on boron, the TZ2P basis set on the metal (Cu, Ag, or Au), and the DZ basis set on all other atoms. Natural Localized Molecular Orbital (NLMO)[24] contributions to shielding were also calculated at this level of theory, with scalar relativistic ZORA included in this analysis.[25] This analysis in ADF gives shielding (σ) as the sum of diamagnetic shielding (σ^d) and of the full paramagnetic shielding term (σ^{p+so}), which is the sum of paramagnetic shielding and spin-orbit contributions.

5.6 References

[1] Mui, K. W.; Ibers, J. A. *Inorg. Chem.* **1969**, *8*, 1921-1928.

[2] Burlitch, J. M. Leonowicz, M. E.; Petersen, R. B.; Hughes, R. E. *Inorg. Chem.* **1979**, *18*, 1097-1105.

[3] Amgoune, A.; Bourissou, D. *Chem. Comun.* **2011**, *47*, 859-871.

[4] You, D.; Gabbai, F. P. *Trends Chem.* **2019**, *1*, 485-496.

[5] Bouhadir, G.; Bourissou, D. in *The Chemical Bond III: 100 years old and getting stronger, ed. D. M. P. Mingos, Springer International Publishing*, Cham, **2017**, pp. 141–201, DOI: 10.1007/430_2015_201.

[6] Hill, A. F.; Owen, G. R.; White, J. P.; Williams, D. J. *Angew. Chem. Int. Ed.* **1999**, *38*, 2759-2761.

[7] Landry, V. K.; Melnick, G.; Buccella, D. Pang, K.; Ulichny, J. C.; Parkin, G. *Inorg. Chem.* **2006**, *45*, 2588-2597.

[8] Bontemps, S.; Bouhadir, G.; Miqueu, K.; Bourissou, *J. Am. Chem. Soc*. **2006**, *128*, 12056-12057.

[9] Sircoglou, M.; Bontemps, S.; Mercy, M.; Saffon, N.; Takahashi, M.; Bouhadir, G.; Maron, L. Bourissou, D. *Angew. Chem. Int. Ed.* **2007**, *46*, 8583-8586.

[10] Suess, D. L. M.; Tsay, C. J.; Peters, J. *J. Am. Chem. Soc.* **2012**, *134*, 14158-14164.

[11] Sircoglou, M.; Bontemps, S.; Mercy, M.; Miqueu, K.; Ladeira, S.; Saffon, N.; Maron, L.; Bouhadir, G.; Bourissou, D. *Inorg. Chem.* **2010**, *49*, 3983-3990.

[12] Bontemps, S.; Gornitzka, H.; Bouhadir, G.; Miqueu, K.; Bourissou, D. *Angew. Chem. Int. Ed.* **2006**, *45*, 1611-1614.

[13] Bontemps, S.; Sircoglou, M.; Bouhadir, G.; Puschmann, H.; Howard, J. A. K.; Dyer, P. W.; Miqueu, K.; Bourissou, D. *Chem. Eur. J.* **2008**, *14*, 731-740.

[14] Sircoglou, M.; Bontemps, S.; Bouhadir, G.; Saffon, N.; Miqueu, K.; Gu, W.; Mercy, M.; Chen, C.; Foxman, B. M.; Maron, L.; Ozerov, O. V.; Bourrisou, D. *J. Am. Chem. Soc.* **2008**, *130*, 16729-16738.

[15] Hermanek, S. *Chem. Rev.*, **1992**, *92*, 325–362.

[16] Alain, A. E.; Shoji, Y.; Fukushima, T.; Bryce, D. L. *Inorg. Chem.* **2015**, *54*, 11889-11896.

[17] Turner, G. L.; Smith, K. A.; Kirckpatrick, R. J.; Oldfield, E. *J. Magn. Reson.* **1986**, *67*, 544-550.

[18] Taylor, J. W.; McSkimming, A.; Moret, M.-E.; Harman, W. H. *Inorg. Chem.* **2018**, *57*, 15406-15413.

[19] Taylor, J. W.; McSkimming, A.; Moret, M.-E.; Harman, W. H. *Angew. Chem. Int. Ed.* **2017**, *56*, 10413-10417.

[20] Bontempts, S.; Bouhadir, G.; Dyer, P. W.; Miqueu, K.; Bourissou, D. *Inorg. Chem.* **2007**, *46*, 5149-5151.

[21] Gaussian 16, Revision C.01, Frisch, M. J.; Trucks, G. W.; Schlegel, H. B.; Scuseria, G. E.; Robb, M. A.; Cheeseman, J. R.; Scalmani, G.; Barone, V.; Petersson, G. A.; Nakatsuji, H.; Li, X.; Caricato, M.; Marenich, A. V.; Bloino, J.; Janesko, B. G.; Gomperts, R.; Mennucci, B.; Hratchian, H. P.; Ortiz, J. V.; Izmaylov, A. F.; Sonnenberg, J. L.; Williams-Young, D.; Ding, F.; Lipparini, F.; Egidi, F.; Goings, J.; Peng, B.; Petrone, A.; Henderson, T.; Ranasinghe, D.; Zakrzewski, V. G.; Gao, J.; Rega, N.; Zheng, G.; Liang, W.; Hada, M.; Ehara, M.; Toyota, K.; Fukuda, R.; Hasegawa, J.; Ishida, M.; Nakajima, T.; Honda, Y.; Kitao, O.; Nakai, H.; Vreven, T.; Throssell, K.; Montgomery, J. A., Jr.; Peralta, J. E.; Ogliaro, F.; Bearpark, M. J.; Heyd, J. J.; Brothers, E. N.; Kudin, K. N.; Staroverov, V. N.; Keith, T. A.; Kobayashi, R.; Normand, J.; Raghavachari, K.; Rendell, A. P.; Burant, J. C.; Iyengar, S. S.; Tomasi, J.; Cossi, M.; Millam, J. M.; Klene, M.; Adamo, C.; Cammi, R.; Ochterski, J. W.; Martin, R. L.; Morokuma, K.; Farkas, O.; Foresman, J. B.; Fox, D. J. Gaussian, Inc., Wallingford CT, 2016.

[22] Schreckenbach, G.; Ziegler, T. J. Phys. Chem. 1995, 99, 606-611.

[23] Krykunov, M.; Ziegler, T.; Van Lengthe, E.; *Int. J. Quant. Chem.*, **2009**, *109*, 1676-1683.

[24] Autschbach, J.; Zheng, S.; Schurko, R. W. *Concepts Magn. Reson., Part A,* **2010**, *36A*, 84-126.

[25] Autschbach, J. *J. Chem. Phys*., **2008**, *128*, 164112.

CHAPTER 6

Origin of the ^{29}Si NMR Chemical Shift in R_3Si-X and Relationship to the Formation of Silylium (R_3Si^+) Ions

6.1 Abstract:

The origin of deshielding in the ^{29}Si NMR chemical shift in R_3Si-X (R = alkyl, mesityl) for X = H, OMe, Cl, OTf, [$CH_6B_{11}X_6$], toluene, and O_x (O_x = surface oxygen) as well as $^{i}Pr_3Si^+$ and Mes_3Si^+ were studied via DFT methods. The geometries of each compound were optimized in M06-L/6-31G(d,p) and agree with the experimental crystal structures. The calculated ^{29}Si NMR chemical shifts also reproduce experimental trends, with $^{i}Pr_3Si$-H having the most shielded ^{29}Si NMR chemical shift and Mes_3Si^+ and $^{i}Pr_3Si^+$ having the most deshielded ^{29}Si NMR chemical shift. The natural localized molecular orbital (NLMO) analyses of the chemical shift in these compounds reveals that the major contributions to paramagnetic shielding is a result of coupling of the Si-R (R = alkyl, H) bonding orbitals to the empty p-orbital in Mes_3Si^+ and $^{i}Pr_3Si^+$ or the σ*(Si-X) orbital in R_3Si-X. This trend also applies to surface bound R_3Si-O_x and explains the trends in the recently isolated $^{t}Bu_2SiH^+$, $^{t}BuSiH_2^+$, and SiH_3^+ that show more shielded ^{29}Si NMR chemical shifts than R_3Si^+ species. There is no correlation between the charge at silicon and the isotropic ^{29}Si NMR chemical shift.

6.2 Introduction:

The silicon derivatives of carbocations (R_3C^+) are silylium ions (R_3Si^+). While R_3C^+ can be accessed in superacidic solutions containing weakly coordinating anions, the

synthesis of R_3Si^+ required counter anions with lower nucleophilicity. [1-2] While carbocations contain sp^2 hybridized geometries that are planar, silylium ions that have been isolated with $B(C_6F_5)_4^-$ or $[CH_6B_{11}Br_6]$ contain C-Si-C bond angles of 117º, which deviate from the expected angle of 120º.[3] The isolation of $[Et_3Si(toluene)][B(C_6F_5)_4]$[4] further complicated silylium chemistry, since this silicon was not planar, and charge was delocalized into the aromatic ring. The isolation of a true silylium cation was not settled until Reed and Lambert isolated $[Mes_3Si][CH(Me_5)B_{11}Br_6]$ which contains a truly planar sp^2 hybridized silicon.[5]

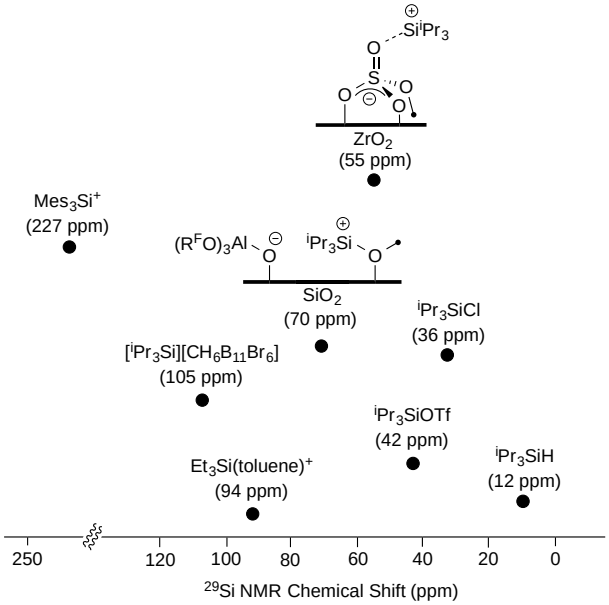

Figure 6.1. Selected ^{29}Si NMR chemical shifts in R_3Si-X and $[R_3Si][X]$

Early syntheses towards the isolation of silylium ions relied on X-ray crystal structures, and the ^{29}Si NMR chemical shift was an indicator used for gauging silylium character in $[R_3Si][X]$. Figure 6.1 is a collection of selected R_3Si-X and $[R_3Si][X]$ ion pairs. The general trend is that as positive charge accumulates on silicon, the ^{29}Si NMR chemical

shift increases. This trend is especially clear for $^{i}Pr_3Si$-H which contains $\delta(^{29}Si)$ = 12 ppm in toluene-d_8. Replacing Si-H with more electron withdrawing groups increases the chemical shift, until $[^{i}Pr_3Si][CH_6B_{11}Cl_6]$, which contains a chemical shift of 115 ppm in the solid state.

The trends in these molecular compounds are supported by DFT calculations of Me_3Si-Cl as a function of the Si-Cl bond distance. The increase in the Si-Cl bond distance led to positive charge accumulation on silicon, and the ^{29}Si NMR chemical shifts are predicted to shift higher.[6] The conclusion that the charge at silicon is related to the ^{29}Si NMR chemical shift is a metric used to quantify silylium character of isolable molecular salts and even silyliums supported on surface oxides. [7-10]

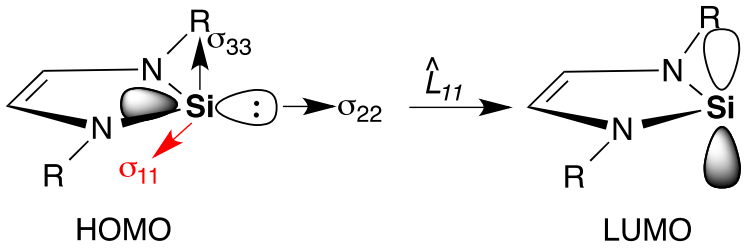

Figure 6.2. Orientation of the chemical shielding tensor in a typical silylene and the coupling of the HOMO and LUMO that result in deshielding through $\hat{L}_{11}$.

Chapter 1 introduced the concept of the orbital rotation model in understanding the chemical shift of a compound. (Figure 1.5) Orbital rotation models are useful in understanding the effects of deshielding, and an example of this for an N-heterocyclic silyleme is shown in Figure 5.2. The ^{29}Si NMR chemical shifts of these range from ~75-120 ppm, and the origin of the deshielding is related to the orientation of the σ_{11} component of the chemical shielding tensor (CST), which can be measured via solid-state

NMR. DFT calculations verified the chemical shift and showed that σ_{11} is oriented in the N-Si-N plane perpendicular to the silylene lone pair orbital. This orbital couples to the vacant p-orbital at silicon and maximizes the contribution of paramagnetic shielding (σ^p) in the nucleus. These deshielding trends can be applied to other silicon interactions such as $R_2Si{=}R_2$, $RSi{\equiv}SiR$, $R_2Si{=}CR'_2$, $R_2Si{=}X$ (X = O, S) and heteroatom substituted silyl lithiums.

This chapter shows that the deshielding of the ^{29}Si NMR chemical shift in R_3Si-X in Figure 5.1 is not related to the charge at silicon but rather the magnitude of paramagnetic shielding (σ^p). The σ^p for each R_3Si-X is calculated using DFT methods and shows that it is maximized when the occupied σ(Si-C) is perpendicular to the σ*(Si-X). In R_3Si^+, σ(Si-C) is instead coupled to the empty p-orbital at silicon. These results show that there is no relationship between the charge at silicon and the ^{29}Si NMR chemical shift.

6.3 Results and Discussion

The set of R_3Si-X selected for this study based on available crystallographic and ^{29}Si NMR data. The geometries of each are optimized at the M06-L/6-31G(d,p) level of theory, and the structures are shown in Figure 6.3. $^{i}Pr_3Si^+$ (**1**), Mes_3Si^+ (**2**), and $Et_3Si(toluene)^+$ were calculated without anions, while **4-9** contained anions. The structural data for the optimized geometries of R_3Si-X are summarized in Table 6.1 and compared to experimental crystal structures when available. This level of theory reproduces the Si-C and Si-X bond lengths and also reproduces the C-Si-C bond angles that are observed in X-ray diffraction structures. The Si-C bond lengths are fairly constant throughout the series

and indicates that these distances are not responsible for the difference in the ^{29}Si NMR chemical shift.

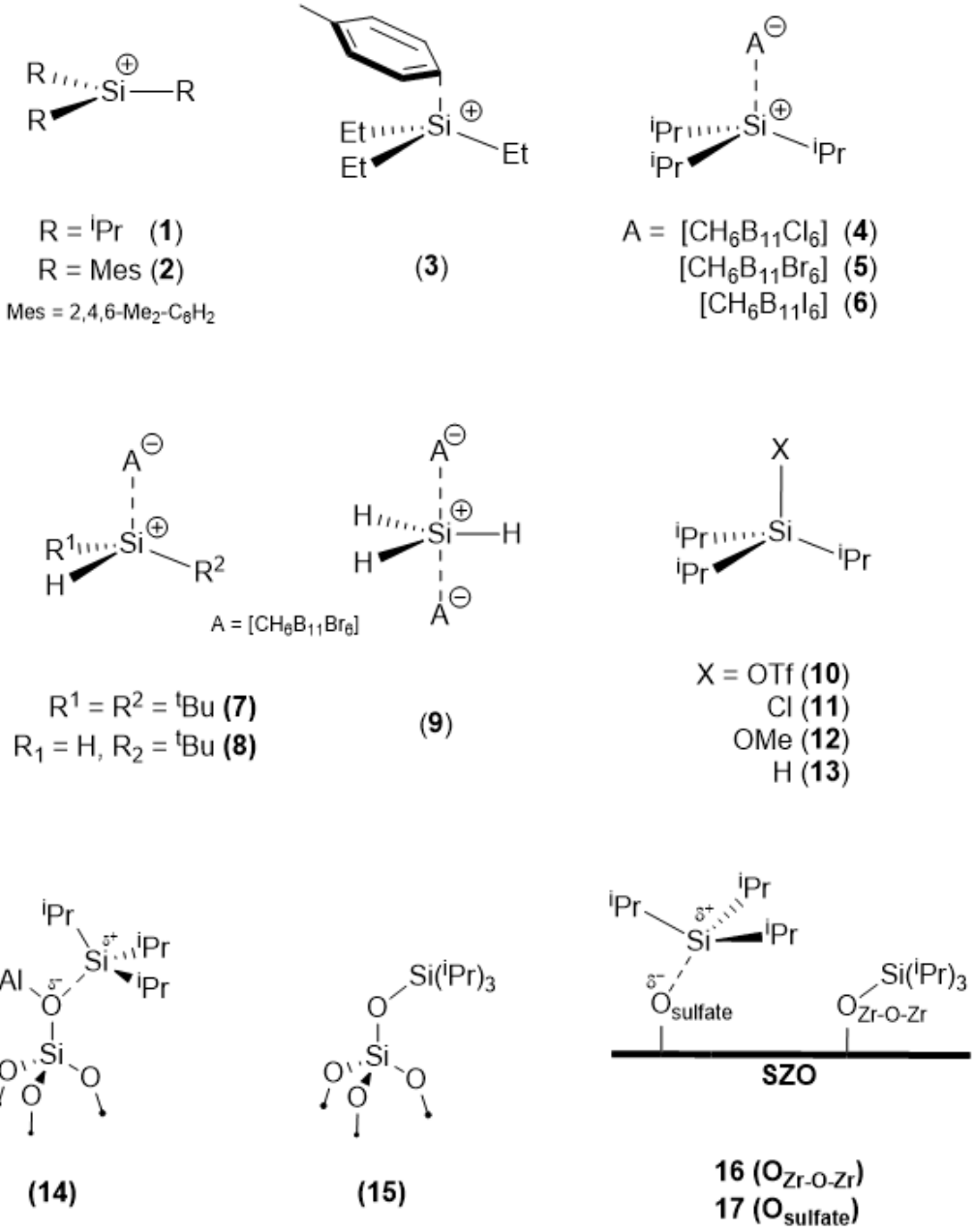

Figure 6.3 Structures **1-17** that are optimized at the M06-L/Zr, Br,I(SDD);6-31G(d,p).

Table 6.1. Key geometric data for $R_3Si–X$.[a]

$R_3Si–X$	Average r_{Si-R} (Å)	r_{Si-X} (Å)	Σ(R-Si-R) (deg.)
1	1.86	---	358.4
2	1.83 (1.82)	---	360.0 (360.0)
3	1.87 (1.85)	2.13 (2.20)	342.5 (341.6)
4	1.88 (1.85)	2.26 (2.32)	348.4 (351.9)
5	1.88 (1.86)	2.45 (2.48)	347.1 (350.9)
6	1.89 (1.88)	2.63 (2.66)	342.5 (346.8)
7	C: 1.89 (1.88) H: 1.48 (1.52)	2.41 (2.41)	345.4 (347.9)
8	C: 1.88 (1.85) H: 1.47 (1.37, 1.51)	2.37 (2.38)	343.4 (342.9)
9	H: 1.46 (1.50)	2.65, 2.65 (2.48, 2.77)	360.0 (357.0)
10	1.88	1.76	343.7
11	1.89	2.10	337.1
12	1.90	1.68	334.0
13	1.90	1.50	333.7
14	1.89	1.68	334.0
15	1.89	1.83	333.4
16	1.89	1.71	337.9
17	1.89	1.77	338.4

[a] – Bond distances and bond angles from $R_3Si–X$ optimized at the M06-L/Zr, Br, I(SDD); 6-31G** level of theory. Values given in parentheses are experimental values from X-ray crystal structures.

Table 6.1 shows that as R_3Si-X approaches R_3Si^+, the silicon becomes more planar which is expected for free silylium ions since they are sp^2 hybridized. For example, the sum of the C-Si-C bond angles in $^iPr_3Si^+$ (**1**) is 358.4° which is close to that obtained for Mes_3Si^+ (**2**) (360°) isolated by Lambert and co-workers.[4] The sum of the bond angles

contract and become less planar when coordinated to weakly coordinating such as toluene and carboranes (342-351^{o}) in **3-6**. Similar behavior is observed for **7** and **8** but an exception is seen in **9**, which exists as an infinite polymer of SiH_3^+ and $CH_6B_{11}Br_6^-$ and exhibits a trigonal pyramidal structure at silicon, resulting in the planarity in the plane formed by the three Si-H bonds.

The sum of the bond angles in $^{i}Pr_3Si$-OTf (**10**) is 343.7^{o} is close to the value for $[^{i}Pr_3Si][CH_6B_{11}X_6]$ (**4-6**), but the Si-O bond length is shorter than the Si-X bond for the weakly coordinating carborane salts. As X becomes more coordinating to silicon, the sum of the C-Si-C bond angles in R_3Si-X decreases from 337.1^{o} > 334.0^{o} > 333.7^{o} for X = Cl (**11**), OMe (**12**), and H (**13**), respectively.

Silylium ions may also form on surface oxides. Oxide surfaces are terminated with acidic -OH groups and can react to form R_3Si-O_x (O_x = surface oxygen) or $[R_3Si][O_x]$. Partially dehydroxylated silica and sulfated zirconia can react with silyl reagents to form R_3Si-O_x and $[R_3Si][O_x]$, respectively, and the solid-state ^{29}Si NMR spectra of these surface-supported R_3Si can be recorded. $Al(OC(CF_3)_3)_3$ activated silica also reacts with triisopropylsilane to form $[^{i}Pr_3Si][O_x]$ as evidenced by deshielded ^{29}Si NMR chemical shifts.

Four cluster models that approximate the $^{i}Pr_3Si$ supported on the aforementioned surface oxides is shown in Figure 6.4. The major surface species for silica partially dehydoryxlated at 700 ^{o}C are isolated silonals, and this is modeled with an $–SiH_3$ capped polyoligosequisiloxane cluster. [11] Capping the remaining silanol with $–Si(^{i}Pr_3)$ instead of

–SiH_3 results in $^{i}Pr_3Si\text{-}O_x$ **14**. Coordination of $Al(OC(CF_3)_3)_3$ to the isolated silanol results in $[^{i}Pr_3Si][O_x]$ (**15**). In **14**, the sum of the C-Si-C bond angles is 334.0°, which indicates a pyramidalized silicon. In **15**, the sum of the C-Si-C bond angles is 333.4° which is slightly lower than **14** but similar to **11-13**. The Si-O distance of 1.83 Å in **15** is significantly longer than in **14** (1.68 Å).

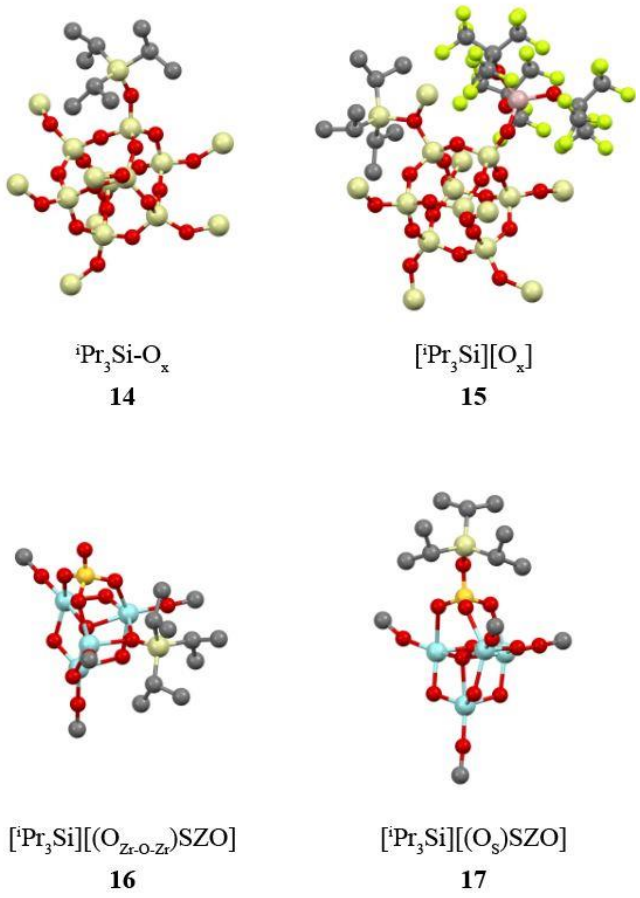

Figure 6.4. Calculated structures of **14-17** optimized at the M06-L/Zr, Zr, Br, I (SDD); 6-31G(d,p) level of theory. Hydrogens are omitted for clarity.

Sulfated zirconia (**SZO**) contains –OH sites that behave as strong acids and basic Zr-O-Zr bridges, and the cluster model in Figure 6.4 is similar to those used previously to

study sulfated oxides in organometallics.[12] As a result of the acidic and basic sites on SZO, the $^{i}Pr_3Si–$ was bound to both the Zr-O-Zr bridge (**16**) and contained a Si-O distance of 1.71 Å and also bound to the sulfate site (**17**), resulting in a longer Si-O distance of 1.77 Å. The sum of the C-Si-C angles in **16** is 337.9^{o} and in **17** is comparable at 338.4^{o}.

Table 6.2 contains the calculated ^{29}Si NMR data for **1-17** at the PBE/Si(TZ2P), DZ level of theory and in general accurately reproduce the isotropic chemical shifts obtained in experiment. Figure 6.5 contains a plot of this data and illustrates that the calculated and experimental chemical shifts are in fact correlated well at this level of theory. In general, as R_3Si-X approaches a free silylium, the chemical shift increases. The ^{29}Si NMR chemical shift of free iPr3Si^{+} is calculated at 343 ppm, and species that do not form silylium ions appear below 45 ppm. [$^{i}Pr_3Si$][$CH_6B_{11}X_6$] have ^{29}Si NMR chemical shifts ~100 ppm, which are between $^{i}Pr_3Si$-X and $^{i}Pr_3Si^{+}$.

$R_3Si–$ supported on surface oxides follow similar trends. The ^{29}Si chemical shift for **14** is not consistent with a silylium ion but for **15** is consistent with a “silylium like” surface spaces. In this trend, **8-9** contain silylium character but are exceptions since they contain chemical shifts below 40ppm. The origin of chemical shielding in these compounds will be discussed later.

Table 6.2. Calculated ^{29}Si NMR parameters of **1-17** at the PBE/Si,Zr(TZ2P), DZ level of theory.

$R_3Si–X$	δ_{expt}	δ_{calc}	Ω	σ_{11}	σ_{22}	σ_{33}	Ref
1	---	343	389	-157	-106	250	---
2	227[a]	213	279	32	33	311	5
3	93[a]	94	92	199	243	291	4
4	115[a]	100	87	208	232	276	2
5	110[a]	105	103	188	221	291	2
6	97[a]	102	113	197	217	299	2
7	73[b]	85	136	170	285	307	13
8	27[b]	40	145	217	318	362	13
9	-65[a]	-54	42	368	398	410	13
10	42[c]	45	22	283	293	305	14
11	36[d]	43	24	281	291	314	15
12	14[d]	14	36	310	317	346	16
13	12[e]	4	42	317	327	359	17
14	4[a]	15	30	310	320	340	18
15	70[a]	64	50	254	267	304	10
16	55[a]	42	30	284	291	314	9
17	-	27	28	305	310	332	-

[a] – solid-state measurement;
[b] – recorded in *o*-dichlorobenzene;
[c] – neat;
[d] – recorded in $CDCl_3$;
[e] – recorded in toluene-d_8

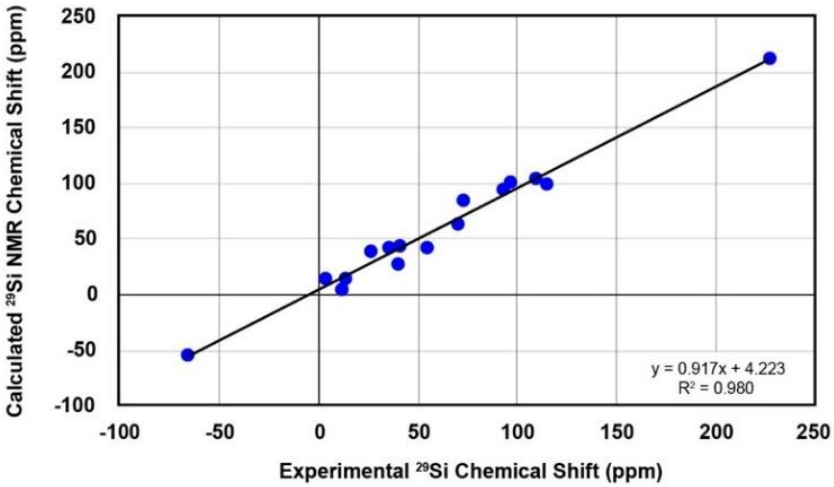

Figure 6.5 Plot of calculated and experimental 29Si NMR chemical shift for **2-15** and **17**. The linear regression gives an R^2 value of 0.980.

Figure 6.6 shows the static ^{29}Si solid-state NMR simulation of **1-3**, **5**, and **10**. In particular, an increased isotropic chemical shielding is generally associated with an increased Ω value. The increased Ω value is visible in the wider line shape produced in these spectra, with $^{i}Pr_3Si^{+}$ producing the widest spectrum in this series. The chemical shielding tensor (CST) which is responsible for the chemical shift is composed of both diagmagnetic (σ^d) and paramagnetic (σ^p) contributions. These values can be readily calculated with the NMR chemical shielding, and the results are graphically displayed in Figure 6.7. Despite a chemical shielding shift range that spans 400 ppm, the σ^d does not change noticeably across the series. This indicates that σ^p is primarily responsible for deshielding in **1-17**.

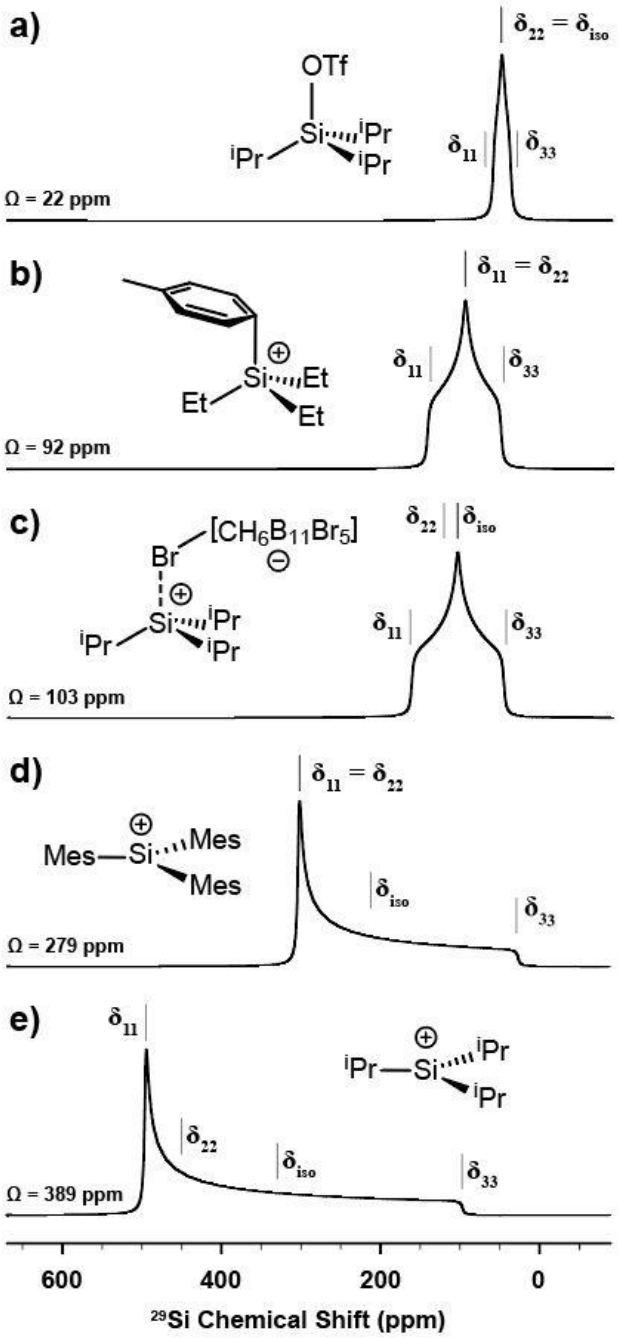

Figure 6.6. Static 29Si solid-state NMR spectra for $^{i}Pr_3Si$-OTf (**10**) $Et_3Si(toluene)^+$ (**3**), $[^{i}Pr_3Si][CH_6B_{11}Br_6]$ (**5**), Mes_3Si^+ (**2**), and $^{i}Pr_3Si^+$ (**1**). The spectra were simulated in Topspin 3.6.1 with line broadening of 500 Hz using the calculated parameters from Table 6.2.

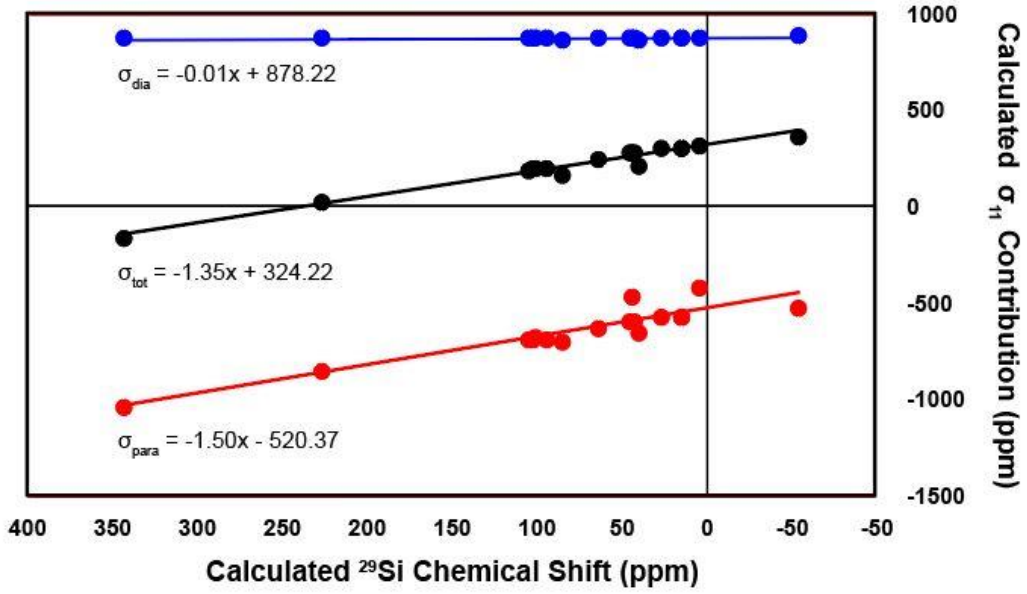

Figure 6.7. Comparison of the calculated σ, σ^d, σ^p versus the calculated isotropic ^{29}Si NMR chemical shift for σ_{11} in **1-17**.

The CST for these compounds is plotted in Figure 6.8. The orientation of the CST contains σ_{11}, the most deshielded component, oriented perpendicular to both the Si-X interaction and a σ(Si-C) bond. In $^{i}Pr_3Si^+$ (**1**), the lack of an Si-X interaction instead places σ_{11} perpendicular to both the vacant p-orbital on silicon and a σ(Si-C) bond. The orientation of σ_{22} is also perpendicular to the Si-X interaction but instead of being perpendicular to a σ(Si-C) roughly bisects two σ(Si-C) bonds. The orientation of σ_{33} is nearly along the Si-X bond.

The orbital rotation model for $\hat{L}_{11}$ couples a σ(Si-C) bond to the σ*(Si-X) antibonding orbital for R_3Si-X and [R_3Si][X]. In free silyliums R_3Si^+, the orbital rotation model for $\hat{L}_{11}$ couples a σ(Si-C) bond to the vacant p-orbital on silicon. (Figure 6.9, page

113) For σ_{22} and $\hat{L}_{22}$, the analysis is roughly the same, but for σ_{33}, the orbital rotation model for $\hat{L}_{33}$ couples a σ(Si-C) bond to a σ*(Si-C) bond, which is much higher in energy. As a result, this interaction leads to shielding in the nucleus. A qualitative molecular orbital diagram that illustrates this is presented in Figure 6.10. DFT calculations of the energy gaps for the major orbitals responsible for deshielding to be 3.61 eV in **1** and 5.57 eV in **5**.

As mentioned earlier, **7-9** are exceptions to the trend in ^{29}Si NMR chemical shift in assigning silylium ion character. The CST tensor plots of **5** and **7-9** are shown in Figure 6.11 and show similar anisotropies and Ω values. While their orientations are different, the NLMO decomposition shows that all contain Si-C bonding orbitals as the main contributor to deshielding in σ_{11}. In **5** and **8**, σ_{11} is oriented along a σ(Si-C) bond similar to **1**. However, in **7**, σ_{11} is oriented along the σ(Si-H) bond and bisects the σ(Si-C) bonds. This orientation allows for the coupling of σ(Si-C) with the empty p-orbital on silicon via $\hat{L}_{11}$. These results show that the origin of the ^{29}Si NMR chemical shift in **7** and **8** are related to other R_3Si-X.

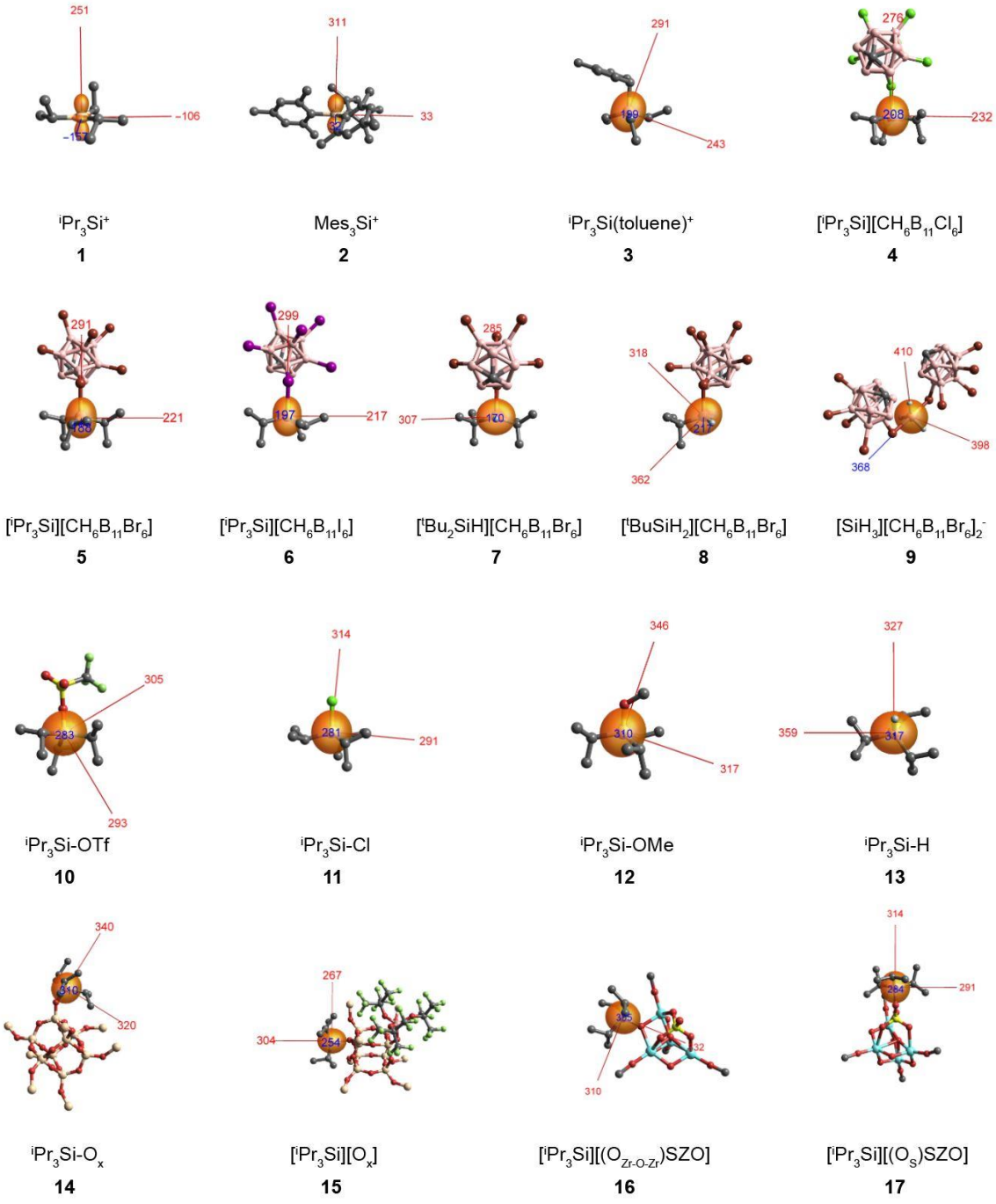

Figure 6.8. Chemical shielding tensor plots for **1-17** with axes shown. When possible, σ_{11}, colored blue, is pointing towards the reader. Selected hydrogens are omitted for clarity.

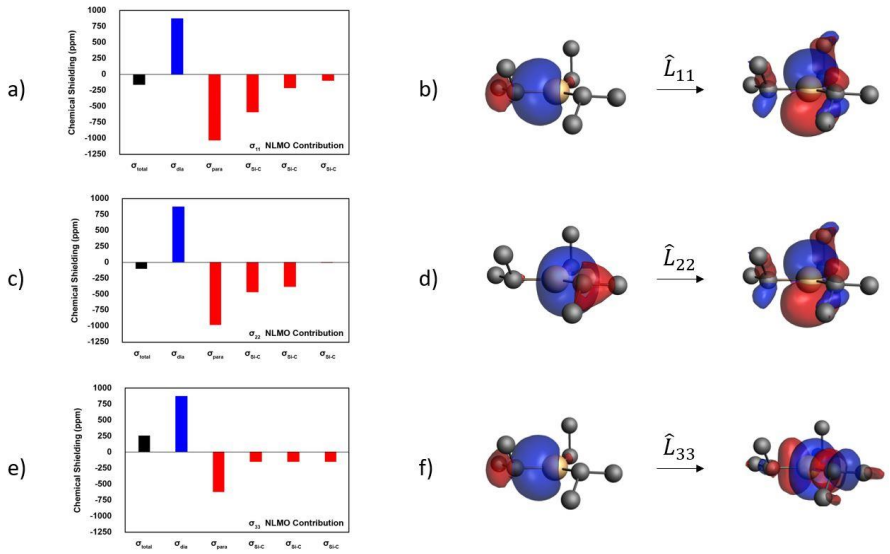

Figure 6.9 NLMO contributions to to σ_{11} (a), σ_{22} (c), and σ_{33} (e) and the major orbitals responsible for deshielding in $^{i}Pr_3Si^+$ (b, d, and f).

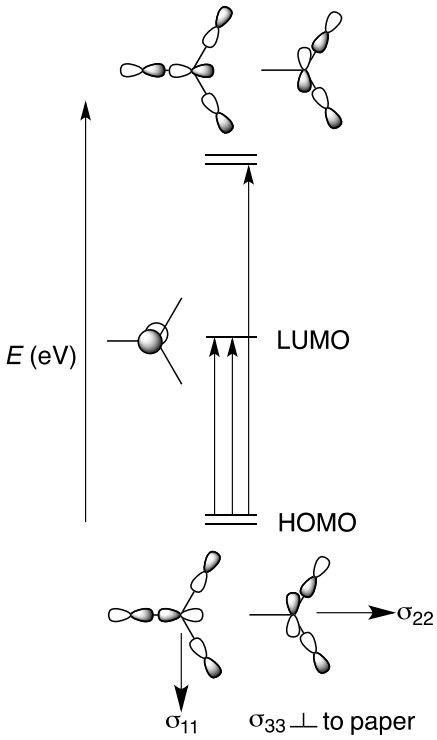

Figure 6.10. Qualitative molecular orbital description of coupling via σ_{11}, σ_{22}, and σ_{33} in $^{i}Pr_3Si^+$.

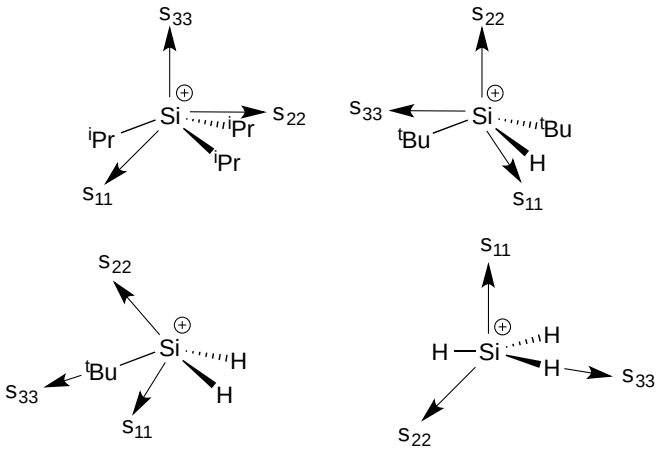

Figure 6.11. Orientation of the chemical shielding tensor in 5, 7-9.

The SiH_3^+ fragment in **9** contains a planar silicon ($\sum_{R-Si-R} \sim 360^o$) like for **1** and suggests that they may contain a similar ^{29}Si NMR chemical shift. However, they are separated by ~400 ppm, with **9** being more shielded than **1**. The CST of **9** is different from **1** and contains σ_{11} perpendicular to the plane defined by the three Si-H bonds. The NLMO decomposition shows that the major deshielding in **9** is a result of coupling between σ(Si-H) and σ*(Si-H) as a consequence of two [CH6B11Br6]- anions interacting with the p-orbital of the SiH_3^+ fragment. This analysis also explains the smaller Ω predicted in **9** than for **1**.

Figure 6.12 shows the net paramagnetic and diamagnetic shielding for each component of the CST for **5** and **7-9**. The σ^d values are consistent throughout, but the σ^p values are responsible for the difference in NMR chemical shift. As one σ(Si-C) bond is substituted with a σ(Si-H) bond, the magnitude of σ^p value is reduced and likely results in an increased energy gap between the σ(Si-C) bond and the σ*(Si-X) orbital. The overall effect is a more shielded ^{29}Si chemical shift as more Si-C are replaced with Si-H bonds.

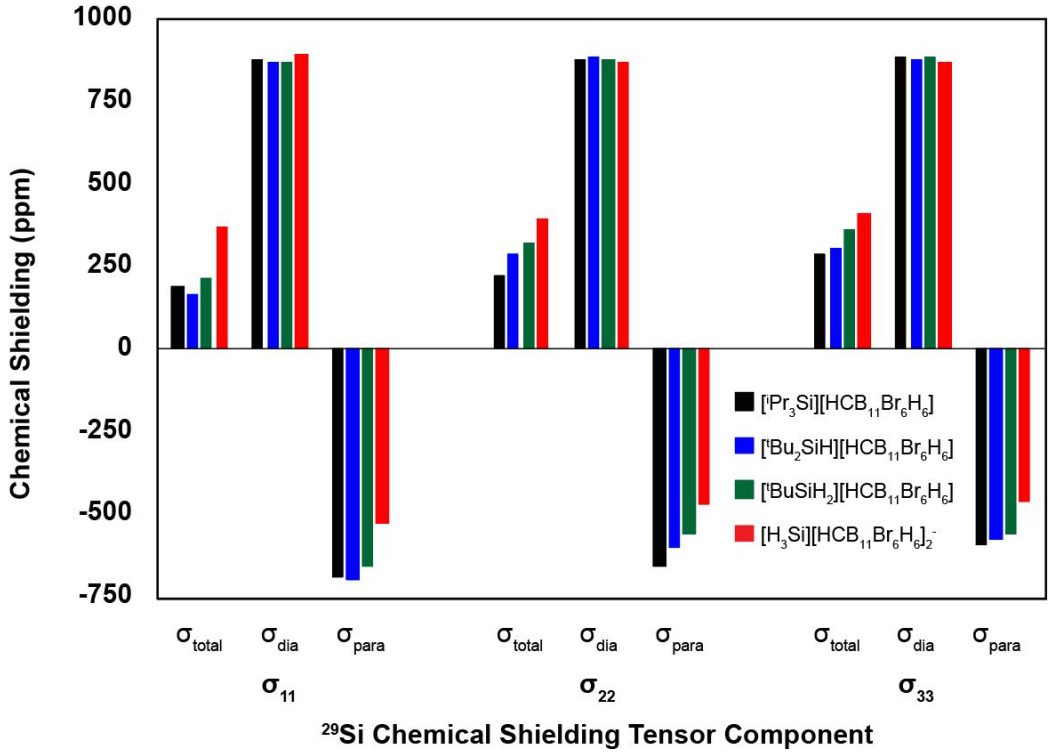

Figure 6.12. Total diamagnetic and paramagnetic contribution to the isotropic chemical shielding tensors for **5**, **7**-**9**.

Plots of ^{29}Si NMR chemical shift or Ω versus charge at this level of theory show no correlation. (Figure 6.13) The absence of any unambiguous correlation in Figure 6.13 indicates that charge is not related to the NMR parameters discussed in this chapter.

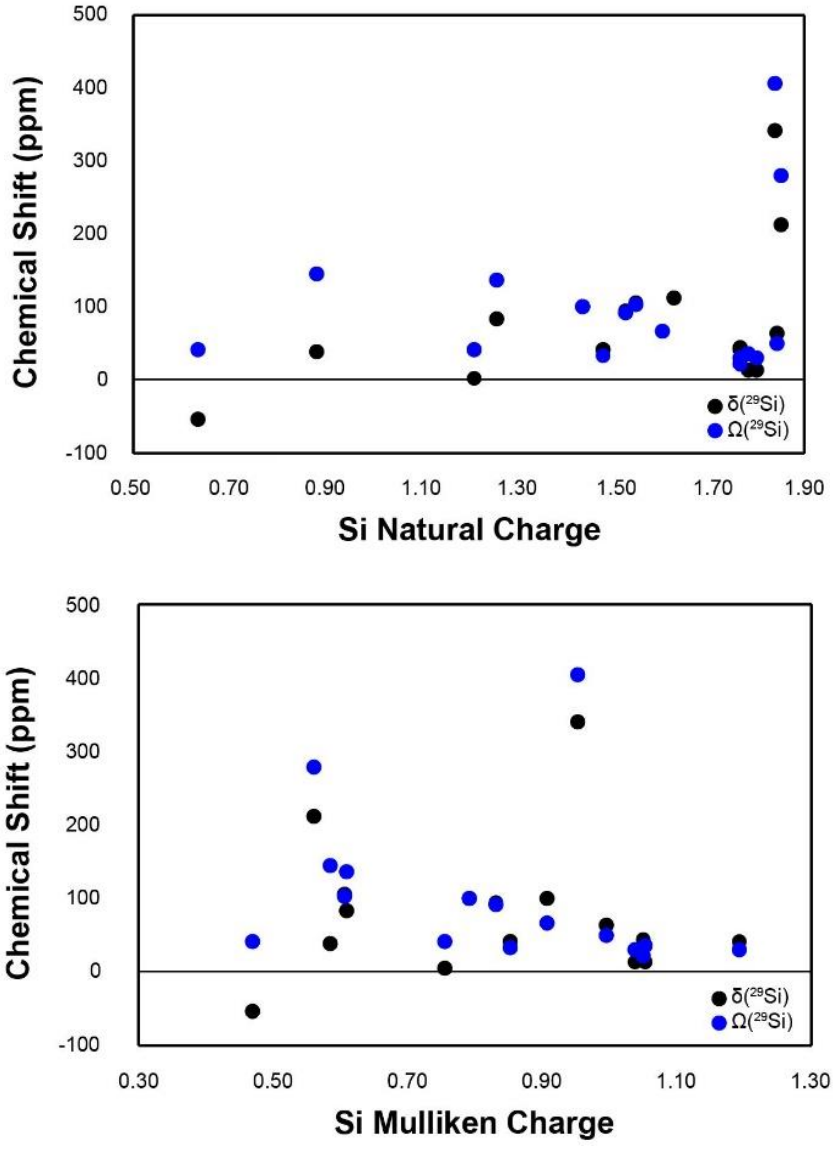

Figure 6.13. Plots of isotropic ^{29}Si NMR chemical shift and span versus natural charge and Mulliken charge.

6.4 Conclusion

DFT methods accurately reproduce the structure and ^{29}Si NMR parameters of a family of molecular and surface R_3Si-X and [R_3Si][X]. Although these species span ~400 ppm on the ^{29}Si NMR chemical shift scale, an analysis of the chemical shielding tensors shows that they are very similar. In all cases except SiH_3^+, the σ_{11} component of the CST couples the σ(Si-C) bonds to σ(Si-X) and deshields the ^{29}Si nucleus. For $^{i}Pr_3Si^+$, the σ(Si-C) bonds are instead coupled to the empty p-orbital on silicon. This behavior is independent of the ^{29}Si NMR chemical shift and is unrelated to the charge at silicon. SiH_3^+ is unique and contains less σ^p than in other R_3Si-X and is more shielded because it interacts with two carborane anions in the soild-state.

Overall, deshielding in the ^{29}Si NMR chemical shift for R_3Si-X can be understood by the coupling of the HOMO and the LUMO. As this energy gap decreases, there is an increase in σ^p and net deshielding of the ^{29}Si nucleus. The structural parameters for R_3Si-X and the CST orientations of **1-17** with the exception of SiH_3^+ are remarkably consistent and will be relevant in the analysis of new R_3Si-X and [R_3Si][X] molecules as they become synthesized. These methods will also be especially relevant for new R_3Si- sites supported on surfaces.

6.5 Materials and Methods

The geometries of all structures were optimized in Gaussian 09[19] using the M06-L functional[20] at the 6-31G** level of theory for H, B, C, O, Si and Cl. Heavier elements (Zr, Br, I) were described with the SDD basis set. Frequency calculations at this level of theory

produced no imaginary frequencies, indicating a ground-state energy minimized structure. **1 – 3** were calculated as free cations, **4 – 8** were calculated as neutral ion-pairs, **9** was calculated as the anion, and **10 – 13** were calculated as molecular species.

The NMR parameters are calculated the Amsterdam Density Functional (ADF) suite,[21] using the GIAO method[22-23] with the PBE functional, the TZ2P basis set on silicon and zirconium, and the DZ basis set on all other atoms. NMR calculations with the meta-GGA functional M06-L is not yet supported in ADF. However, the combi-nation of geometry optimization in G09 at the M06-L/6-31G**/SDD level of theory, followed by computation of NMR parameters in ADF at the PBE/TZ2P(Si, Zr)/DZ results in good agreement with experiment. Natural Localized Molecular Orbital (NLMO) contributions to shielding were also calculated at this level of theory, with scalar relativistic ZORA included in this analysis.[24] This analysis in ADF gives shielding (σ) as the sum of diamagnetic shielding (σ^{d}) and of the full paramagnetic shielding term (σ^{p+so}), which is the sum of paramagnetic shielding and spin-orbit contributions. In this study the spin-orbit contributions are negligible. Therefore, we refer to para-magnetic shielding as σ^{p} for the species studied here. The canonical orbitals for **1** and **5** were calculated at the same level of theory to extract energies for the orbitals contributing to σ^{p} from the NLMO analysis.

6.6 References

[1] Olah, G. A.; Prakash, K. S.; Sommer, J.; Molnar, A. *Superacid Chemistry, John Wiley & Sons*, **2009**.

[2] Reed, C. A. *Acc. Chem. Res.* **1998**, *31*, 325-332.

[3] Reed, C. A.; *Acc. Chem. Res.* **2010**, *43*, 121-128.

[4] Lambert, J. B.; Zhang, S.; Stern, C. L.; Huffman, J. C. *Science*, **1993**, *260*, 1917-1918.

[5] Kim, K.-C.; Reed, C. A.; Elliott, W.; D.; Mueller, L. J.; Tham, F.; Lin, L.; Lambert, J. B. *Science*, **2002**, *297*, 825-827.

[6] Xie, Z.; Manning, J.; Reed, R. w.; Mathur, R.; Boyd, P. D. W.; Benesi, A.; Reed, C. A. *J. Am. Chem. Soc.* **1996**, *118*, 2922-2928.

[7] Wu, Q.; Qu, Z.-W.; Omann, L.; Irran, E.; Klare, H. F. T.; Oestreich, M. *Angew. Chem. Int. Ed.* **2018**, *57*, 9176-9179.

[8] Kuppers, T.; Bernhardt, E.; Eujen, R.; Willner, H.; Lehmann, C. W. *Angew. Chem. Int. Ed.* **2007**, *46*, 6346-6349.

[9] Culver, D. B.; Conley, M. P.; *Angew. Chem. Int. Ed.* **2018**, 57, 14902-14905.

[10] Culver, D. B.; Venkatesh, A.; Huynh, W.; Rossini, A. J.; Conley, M. P. *Chem. Sci.* **2020**, *11*, 1510-1517.

[11] Del Rosal, I.; Gerber, I. C.; Poteau, R.; Maron, L. *J. Phys. Chem. A.* **2010**, *114*, 6322-6330.

[12] Syed, Z. H.; Kaphan, M.; Perras, F. A.; Pruski, M.; Ferrandon, M. S.; Wegener, E. C.; Celik, G.; Wen, J.; Liu, C.; Dogan, F.; Goldberg, K. I.; Delferro, M. *J. Am. Chem. Soc.* **2019**, *141*, 6325-6337.

[13] Ramirez-Contreras, R.; Bhuvanesh, N.; Zhou, J.; Ozerov, O. V. *Angew. Chem. Int. Ed.* **2013**, *52*, 10313-10315.

[14] Olah, G. A.; Laali, K.; Farooq, O. *Organometallics*, **1984**, *3*, 1337-1340.

[15] Zhang, C.; Patschinski, P.; Stephenson, D. S.; Panisch, R.; Wender, J. H.; Holthausen, M. C.; Zipse, H. *Phys. Chem. Chem. Phys.* **2014**, *16*, 16642-16650.

[16] Savela, R.; Zawartka, W.; Leino, R. *Organometallics* **2012**, *31*, 3199-3206.

[17] Xie, Z.; Liston, D. J.; Jelinek, T.; Mitro, V.; Bau, R.; Reed, C. A. *J. Chem. Soc. Chem. Commun.* **1993**, 384-386.

[18] Epping, J. D.; Yao, S.; Karni, M.; Apeloig, Y.; Driess, M. *J. Am. Chem. Soc.* **2010**, *132*, 5443-5455.

[19] Gaussian 16, Revision C.01, Frisch, M. J.; Trucks, G. W.; Schlegel, H. B.; Scuseria, G. E.; Robb, M. A.; Cheeseman, J. R.; Scalmani, G.; Barone, V.; Petersson, G. A.; Nakatsuji, H.; Li, X.; Caricato, M.; Marenich, A. V.; Bloino, J.; Janesko, B. G.; Gomperts, R.; Mennucci, B.; Hratchian, H. P.; Ortiz, J. V.; Izmaylov, A. F.; Sonnenberg, J. L.; Williams-Young, D.; Ding, F.; Lipparini, F.; Egidi, F.; Goings, J.; Peng, B.; Petrone, A.; Henderson, T.; Ranasinghe, D.; Zakrzewski, V. G.; Gao, J.; Rega, N.; Zheng, G.; Liang, W.; Hada, M.; Ehara, M.; Toyota, K.; Fukuda, R.; Hasegawa, J.; Ishida, M.; Nakajima, T.; Honda, Y.; Kitao, O.; Nakai, H.; Vreven, T.; Throssell, K.; Montgomery, J. A., Jr.; Peralta, J. E.; Ogliaro, F.; Bearpark, M. J.; Heyd, J. J.; Brothers, E. N.; Kudin, K. N.; Staroverov, V. N.; Keith, T. A.; Kobayashi, R.; Normand, J.; Raghavachari, K.; Rendell, A. P.; Burant, J. C.; Iyengar, S. S.; Tomasi, J.; Cossi, M.; Millam, J. M.; Klene, M.; Adamo, C.; Cammi, R.; Ochterski, J. W.; Martin, R. L.; Morokuma, K.; Farkas, O.; Foresman, J. B.; Fox, D. J. Gaussian, Inc., Wallingford CT, 2016.

[20] Zhao, Y.; Truhlar, *Theor. Chem. Acc.* **2008**, *120*, 215-241.

[21] te Velde, G.; Bickelhaupt, F. M.; Baerends, E. J.; Guerra, C. F.; van Gisbergen, S. J. A.; Snijders, J. G.; Ziegler, T. *J. Comp. Chem.* **2001**, *22*, 931.

[22] Schreckenbach, G.; Ziegler, T. J. Phys. Chem. 1995, 99, 606-611.

[23] Krykunov, M.; Ziegler, T.; Van Lengthe, E.; *Int. J. Quant. Chem.*, **2009**, *109*, 1676-1683.

[24] Autschbch, J. *J. Chem. Phys.* **2008**, *128*, 164112.

CHAPTER 7

Formation of a Strong Heterogeneous Aluminum Lewis Acid on Silica

7.1 Abstract:

$Al(OC(CF_3)_3)_3(PhF)$ coordinated to silica partially dedroxylated at 700 ^oC on silica form well-defined $\equiv Si–OH\text{---}Al(OC(CF_3)_3$. (**1**) The ^{27}Al NMR and DFT calculations with small cluster models of $SiO_{2\text{-}700}$ show that **1** contains a Lewis acidic aluminum site with a distorted trigonal bipyramidal coordination geometry, with two additional coordinates to a fluorine from the alkoxide and a nearby siloxane bridge. Fluoride ion affinity (FIA) calculations show that 1 is more Lewis acidic than the isolable $B(C_6F_5)_3$ and $Al(OC(CF_3)_3)_3(PhF)$ but weaker than solvent-free $Al(OC(CF_3)_3)_3$ and $^iPr_3Si^+$. $Cp_2Zr(CH_3)_2$ reacts with **1** to form **3** by methide abstraction and forms $[Cp_2ZrCH_3][\equiv SiOAl(OC(CF_3)_3)_2(CH_3)]$.

7.2 Introduction:

Lewis acids are synthetically useful in catalysis either as activating agents or as the active species.[1-3] The simplest Lewis acids are tri-coordinate boron halides are known to be active in the polymerization of styrene, and Lewis acids may also serve as additives that initiate polymerization.[4-6] The more complex yet strong Lewis Acid $B(C_6F_5)_3$ reacts with silanols on silica partially dehydroxylated at 500 ^oC to form new Lewis acidic sites (Figure 7.1) Understanding the generation of Lewis acid sites on surface oxides is useful in the development of new Lewis acidic surfaces that may catalyze other reactions.

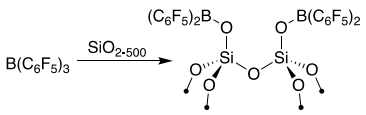

Scheme 7.1. Reaction of $SiO_{2\text{-}500}$ with $B(C_6F_5)_3$.

One strategy to assess the Lewis acidity of compounds includes the Gutmann-Beckett method which involves the coordination of triethylphosphine oxide (TEPO) to a Lewis acid for form TEPO→LA.[7] The downfield shift in the ^{31}P NMR chemical shift after Lewis acid coordination to TEPO is used to assess its Lewis acidity, and this method has been applied to assess the Lewis acidity in tri-coordinate boranes as well as frustrated Lewis pairs.[8-11] This method is often a convenient experiment to measure a compound's Lewis acidity, but binding of the NMR solvent may also affect the ^{31}P NMR chemical shift.

Another strategy to assess Lewis acidity is the calculation of the fluoride ion affinity (FIA).[12] The method for FIA calculations is presented below in Figure 7.2. The method begins with calculating the energy for the Lewis Acid (A), the fluorinated Lewis acid (A-Y^-; Y = F), and both Me_3Si^+ and Me_3Si-F. These calculations require the isodesmic reaction in Figure 7.2 because the energy of the naked fluoride ion is difficult to accurately

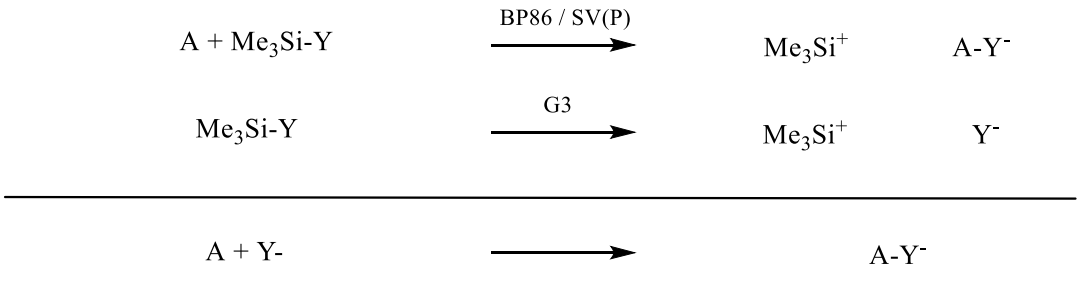

Figure 7.1. Isodesmic reaction for the calculation of ion affinity; for FIA, Y = F.

calculate experimentally at lower levels of theory.[13] To avoid this problem, the energy calculations of the previously mentioned compounds are often performed at a lower level of theory and anchored to the true fluoride ion affinity of Me_3Si^+ at very high levels of theory such as G3.[12]

The reaction of $Al(OC(CF_3)_3)_3(PhF)$ and Aerosil $SiO_{2\text{-}700}$ in perfluorohexanes yields ≡Si–OH---$Al(OR^F)_3$.[14] When fluorobenzene is instead used as the solvent, the reaction yields ≡$SiOAl(OC(CF_3)_3)_2$ (**1**) a very strong well-defined Lewis acid. (Scheme 7.1) The Lewis acid site is supported on a solide oxide, and FIA calculations show that **1** is a stronger Lewis acid than $B(C_6F_5)_3$. **1** also reacts with $Cp_2Zr(CH_3)_2$ via methide abstraction to generate metallocenium ions.

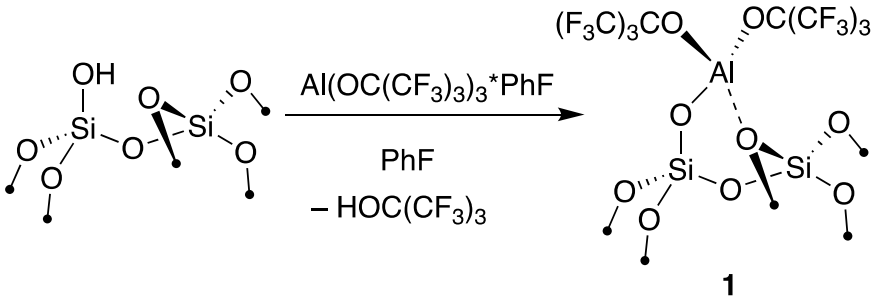

Scheme 7.2. Synthesis of **1**.

7.3 Results and Discussion

$Al(OC(CF_3)_3)_3(PhF)$ reacts with Aerosil $SiO_{2\text{-}700}$ at 45 ^oC to form **1** and 0.22 ± 0.01 mmol H-$OC(CF_3)_3$ g^{-1}. The FTIR of **1** contains sp^2 C-H stretches and sp^2 C=C stretches at 1480 cm^{-1} associated with adsorbed PhF as well as a complex ν_{OH} region for unreacted silanols. (Figure 7.3) The 1H MAS NMR spectrum of 1 contains signals expected for PhF

(7.1 ppm) as well as hydrogen bonded (4.6 ppm) and free (2.3 ppm) silanols (Figure 7.3) The bridging silanol in ≡Si–OH---Al(OC(CF_3)$_3$ appears at 5.0 ppm in the ^{1}H NMR spectra and is not noticeably present in **1**.

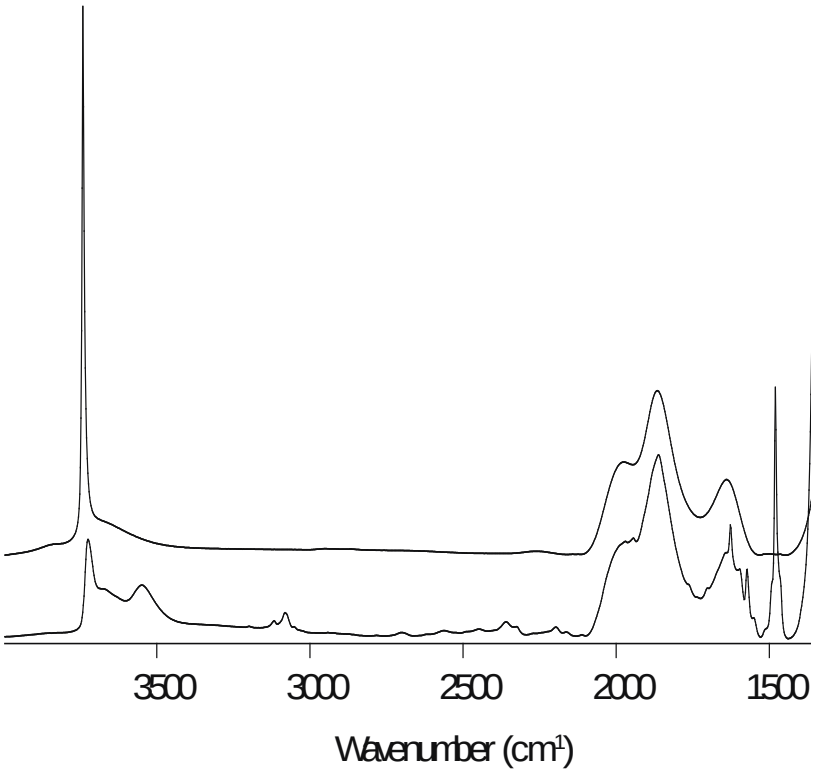

Figure 7.2. FTIR spectra of **1** (bottom) and $SiO_{2\text{-}700}$ (top).

The static ^{27}Al NMR spectrum of 1 contains a broad signal, and simulations reveal an isotropic chemical shift (δ_{iso}) of 48 ppm and a quadrupolar coupling constant (C_Q) of 17.7 (2) MHz (Figure 7.4). The ^{19}F MAS NMR spectrum contains signals at -78 and -132 ppm that are expected for adsorbed PhF and the –OC(CF_3)$_3$ groups of **1**. While the ratio of these signals is 1:1, the 1H and ^{19}F NMR chemical shifts indicate that PhF is not in close proximity to the Al sites of **1**.

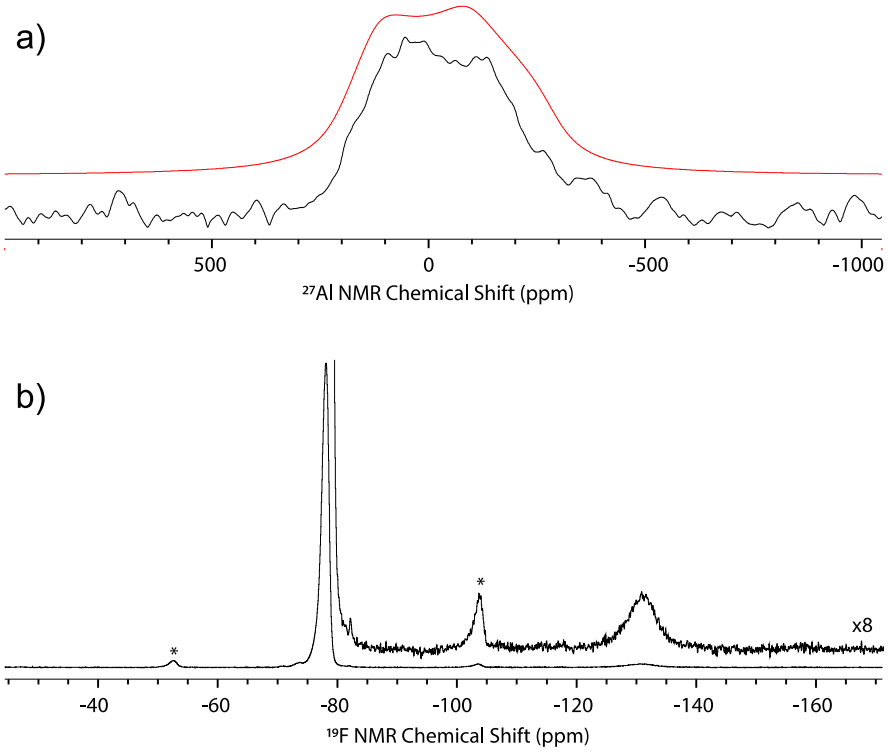

Figure 7.3. Static ^{27}Al NMR spectrum of **1** at 14.1T (a). The experimental spectrum is in black, and the simulated spectrum is in red. ^{19}F MAS NMR spectrum of **1** (b). * denotes spinning side bands.

The NMR parameters of SiH_3-capped polysequisiloxane models of **1** calculated at the B3LYP/6-31G++(d,p) level of theory are shown in Figure 7.4. Figure 7.4a shows a distorted bipyramidal structure with Al-OSi (1.693 Å), two Al_OC(CF3)3 (1.755 Å), and two long Al-F (2.100 Å and 2.120 Å). The sum of the O-Al-O bond angles is 360.0º, and the F-Al-F bond angle is 163.7º. This structure is predicted to have ^{27}Al NMR properties of δ_{iso} = 53ppm and C_Q = 26.0 MHz, both of which are inconsistent with experimental simulations. Replacing one Al-F with a siloxane bridge results in Figure 7.4b and yields δ_{iso} = 50ppm and C_Q = 18.7 MHz, which are in good agreement with experiment. This structure contains Al-X distances of 1.775 Å (Al-OSi), 1.724 Å and 1. 752 Å (Al-

$OC(CF_3)_3$), 1.974 Å (Al—$O(Si\equiv)_2$) and 2.381 Å (Al-F). The sum of the O-Al-O angles is 353.03° and the F-Al--$(OSi\equiv)_2$) angle is 162.7°. The coordination of PhF results in Figure 7.4c, which contains a C_Q of 20.1 MHz, which is inconsistent with the experimental C_Q.

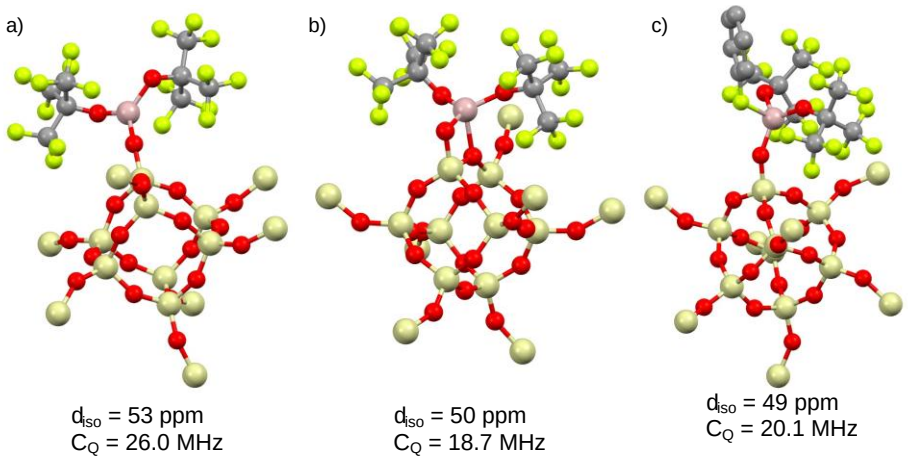

Figure 7.4. Calculated structures of **1** using the polysequisiloxane cluster to model the surface of SiO_2. The calculated ^{27}Al parameters are shown below each.

Table 7.1. Fluoride Ion Affinity (FIA) of Selected Lewis Acids and **1** in kJ mol^{-1}.

Compound	**FIA**
$B(C_6F_5)_3$	448
$Al(OC(CF_3)_3)_3(PhF)$	514
1	528
$Al(OC(CF_3)_3)_3$	540
$^{i}Pr_3Si^{+}$	1073

Fluoride ion affinity (FIA) calculations show that **1** is a strong Lewis acid. Table 7.1 contains the calculated FIA at the BP86/SV(P) level of theory for $B(C_6F_5)_3$, **1**, $Al(OC(CF_3)_3)_3(PhF)$, base-free $Al(OC(CF_3)_3)_3$, and $^{i}Pr_3Si^{+}$. The FIA of **1** is 528 kJ/mol which is strong than both $B(C_6F_5)_3$ and $Al(OC(CF_3)_3)_3(PhF)$ but weaker than base-free $Al(OC(CF_3)_3)_3$ and $^{i}Pr_3Si^{+}$.

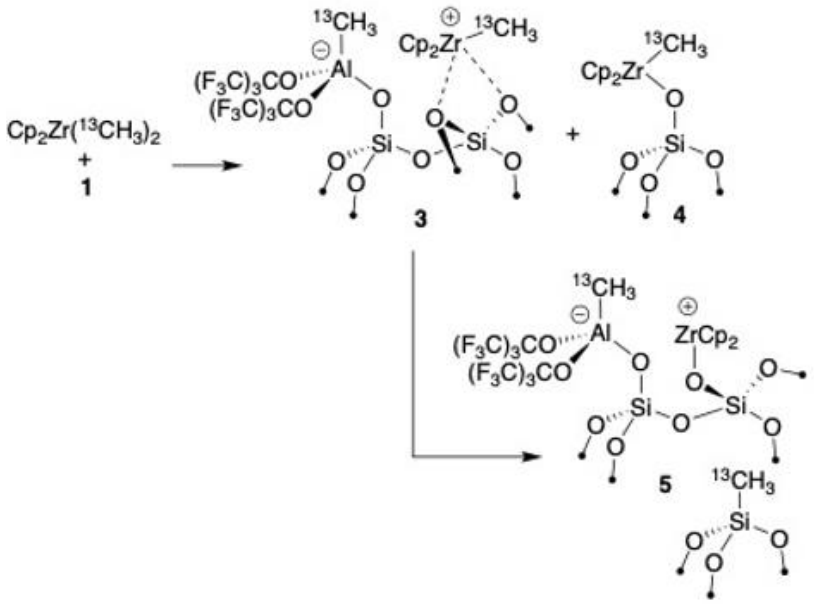

Scheme 7.3. Reaction of $Cp_2Zr(CH_3)_2$ with **1**.

$Cp_2Zr(^{13}CH_3)_2$ reacts with **1** to yield $[Cp_2ZrCH_3][\equiv SiOAl(OC(CF_3)_3)_2(CH_3)]$ (**3**) (Scheme 7.2) The $^{13}C\{^{1}H\}$ CPMAS NMR spectrum of **3** contains chemical shifts at 38, 23, 3, and -11 ppm. (Figure 7.5) The signal at 23 ppm is assigned to $Cp_2Zr(^{13}CH_3)(OSi\equiv)$ (**4**),[15] which is consistent with the 0.06 ± 0.01 mmol/g methane that forms from the reaction of residual silanols present on **1**. The signal at 3ppm is assigned to $\equiv Si-^{13}CH_3$, [16] and only the peaks at 38 and -11 ppm are associated with **3**.

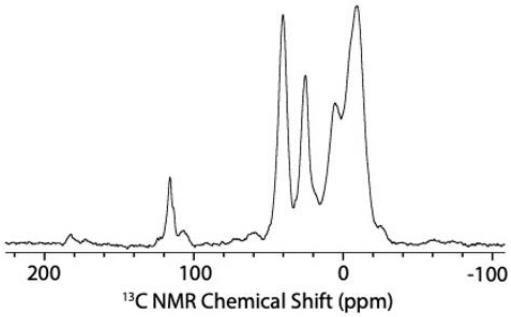

Figure 7.5. $^{13}C\{^{1}H\}$ CPMAS NMR spectrum of $Cp_2Zr(^{13}CH_3)_2$/**1**.

The signal at 38 ppm is assigned to the Zr-CH_3, and the peak at -11ppm is assigned to the Al-CH_3 in **3**. A 2D ^{1}H-^{13}C CP heteronuclear correlation (HETCOR) NMR spectrum of **3** shows that the ^{13}C NMR signal at 38ppm correlates with the ^{1}H NMR signal at 2.0ppm, and the Al-^{13}**C**H_3 signal at -11 ppm correlates with the ^{1}H NMR signals at 0.6 ppm. The ^{27}Al MAS NMR of **3** contains a narrower signal with δ_{iso} = 77 ppm and C_Q = 11.2 MHz (Figure 7.6) This smaller C_Q value is expected for aluminum in a more symmetrical, tetrahedral environment in **3** than compared to **1**.

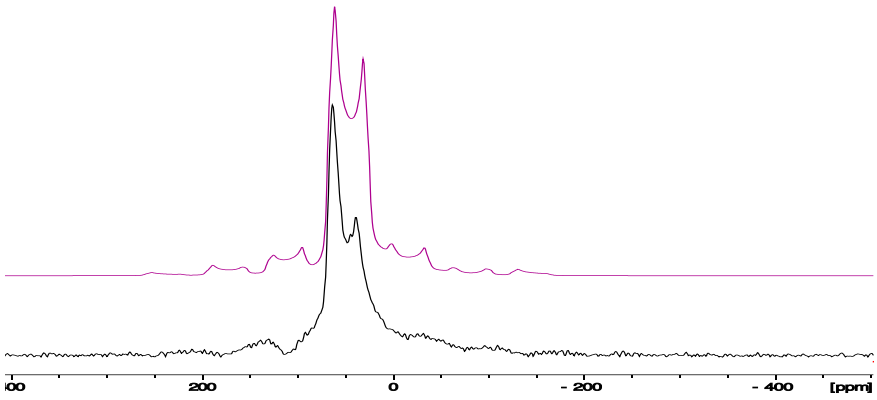

Figure 7.6. $^{27}Al\{^{1}H\}$ MAS spectrum of **3** at magic angle spinning speed of 10 kHz. The experimental spectrum is in black, and the simulated spectrum is in magenta.

A $^{13}C\{^{27}Al\}$ Phase-Modulated Resonance-Echo Saturation-Pulse Double-Resonance (PM-RESPDOR) [17-19] (Figure 7.7a) selectively dephases ^{13}C-^{27}Al spin pairs in close proximity and further identifies that the peak at -11ppm corresponds to the Al-CH_3.Simulations of the dipolar dephasing curve with a dipolar coupling constant of 1.35 kHz show that the C-Al internuclear distance is 1.8 Å and assigns this to the [≡SiOAl(OC(CF_3)$_3$)$_2$(**^{13}C**H_3)] anion. (Figure 7.7a) The ^{13}C NMR signals for the Zr-**^{13}C**H_3 fragments in 3 and 4 do not exhibit dephasing in the $^{13}C\{^{27}Al\}$ PM-RESPDOR experiment and therefore belong to carbon that are far (> ~5 Å) from aluminum. (Figure 7.7b)

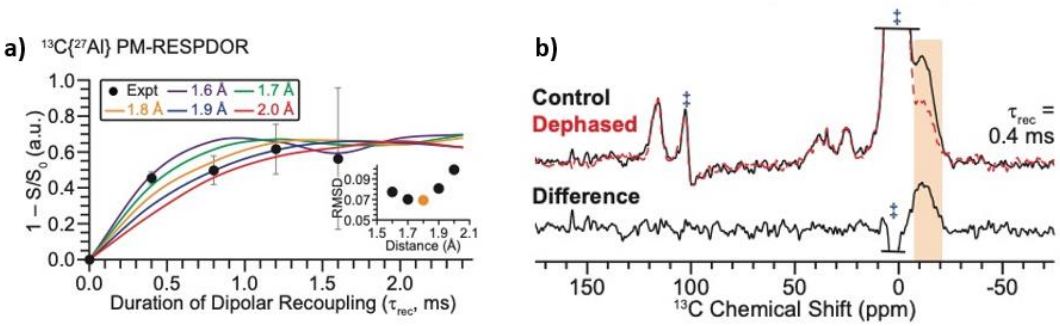

Figure 7.7. $^{13}C\{^{27}Al\}$ PM-RESPDOR curve of **3** for the ^{13}C NMR signal at -11 ppm. (a) Experimental points are in black, and simulations are solid lines. Control, dephased, and difference RESPDOR spectra (b) are recorded with ‡ indicating ^{13}C NMR signals from the silicon plug.

The NMR experiments described above aid DFT calculations of **3-DFT** that is shown in (Figure 7.8. At the B3LYP/6-31++G(d,p) level of theory, **3-DFT** is predicted to have ^{13}C NMR chemical shifts of -10ppm and 35ppm for the Al-**^{13}C**H_3 fragment and the Zr-**^{13}C**H_3 fragment, respectively. The calculated ^{27}Al C_Q is -11.6MHz, which is close to the experimental C_Q of 11.2 MHz. The calculated Al-C distance of 1.96 Å is close to the value extracted from the $^{13}C\{^{27}Al\}$PM-RESPDOR experiments. The $Cp_2Zr(CH_3)^+$

fragment in **3-DFT** is formally a saturated 18-electron zirconocenium and contains Zr-$(OSi\equiv)_2$ distances of 2.497 Å and 2.532 Å, which are longer than the Zr-O distances in $Cp_2ZrCH_3(thf)^+$ (2.122(14) Å).[20]

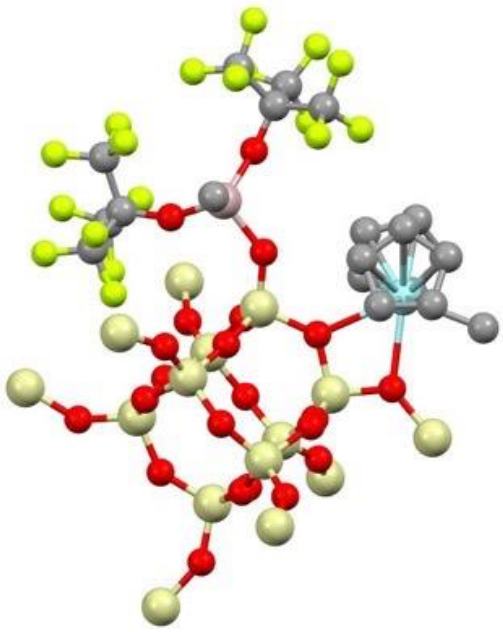

Figure 7.8. Structure of **3-DFT** calculated at the B3LYP/6-31++G(d,p) level of theory.

7.4 Conclusion

The reaction of $Al(OC(CF_3)_3)(PhF)$ with $SiO_{2\text{-}700}$ is interesting. When mixed in apolar perfluorohexane, the Lewis acid coordinates to silanols present in $SiO_{2\text{-}700}$. [14] When coordinated to slightly more polar fluorobenzene, a proton transfer occurs and releases H-$OC(CF_3)_3$ to form **1**. The FIA of **1** indicates that it is more Lewis acidic than $B(C_6F_5)_3$ and its strong Lewis acidity allows for methide abstraction from $Cp_2Zr(CH_3)_2$ to form a well-defined surface-supported metallocenium ion pair. Solid-state NMR experiments and DFT calculations were used in tandem and allowed for the full characterization of **1** and **3**.

7.5 Materials and Methods

All manipulations were performed under an inert atmosphere of nitrogen or argon either on a high vacuum Schlenk line or in a glovebox. Grafting reactions were performed in double Schlenk flasks or flasks equipped with Teflon valves that connect directly to high vacuum lines. Benzene-d_6 was purchased from Cambridge Isotope Laboratories, dried over sodium/benzophenone, degassed by freeze-pump-thaw cycles, distilled under vacuum, and stored in an inert atmosphere glovebox. N-pentane was dried by passing through a J.C. Meyer solvent system containing two activated alumina columns, stored over sodium/benzophenone, and degassed and distilled under vacuum. Fluorobenzene and triethylsilane were dried over CaH_2, degassed, and vacuum distilled prior to use.

FT-IR spectra were recorded as pressed pellets using a Bruker Alpha IR spectrometer in an argon-filled glovebox. Elemental analysis of Al and Zr were carried out by digesting solid samples in dilute nitric acid and measuring samples at the University of California, Riverside Environmental Sciences Research Laboratory (ESRL) on a Perkin-Elmer Optima 7300DV ICP-OES.

Solution NMR spectra at 7.05T were acquired on an Avance Bruker 300. ^{1}H NMR spectra were referenced to the NMR solvent residual peal. Solution $^{19}F\{^{1}H\}$ spectra were referenced to an external standard of C_6F_6 (-163.9 ppm). All solid-state NMR samples were packed in an argon or nitrogen filled glovebox. Solid state NMR spectra at the University of California, Riverside were recorded in 4 mm zirconia rotors at 10 kHz spinning at the magic angle at 14.1 T on an Avance Bruker NEO600 spectrometer equipped with a

standard-bore magnet. All solid-state NMR were processed and simulated using Topspin v.4.0.9.

*Synthesis of **1***. $SiO_{2\text{-}700}$(1g, 0.26 mmol OH) and $Al[OC(CF_3)_3]_3$(PhF) (240 mg, 0.29 mmol, 1.1 mol eq) were transferred to one arm of a double-Schlenk flask inside an argon-filled glovebox. Fluorobenzene (ca. 6 mL) was transferred under vacuum to the flask at 77K. The mixture was heated to 45˚C and gently stirred for two hours. The clear solution was filtered to the other side of the double Schlenk to yield **1** and was washed three times by condensing PhF, stirring, and filtering solvent back to the other side of the flask. The volatiles were vacuum transferred to quantify $H\text{-}OC(CF_3)_3$ released during this reaction, and then the solid was dried under vacuum for 40 minutes. **1** was collected as a white solid and was stored in an Ar glovebox freezer at -20˚C. FTIR: νO-H = 3724 (≡Si-OH) and 3548 (≡Si-OH---$Al(OR^F)_3$) cm-1 as well as νC-H = 3081 (PhF physisorbed to surface) cm^{-1}. Solid State NMR: ^{1}H MAS NMR (600MHz): 6.21 (PhF), 3.74 (≡Si-OH---$Al(OR^F)_3$), 1.3 (≡Si-OH) ppm $^{13}C\{^1H\}$ MAS NMR: 122 (≡Si-$OC(CF_3)_3$, 114 (PhF), 78 (≡Si-$OC(CF_3)_3$.

*Synthesis of **3***. **1** (0.400 g, 0.088 mmol Al LA site) and Cp_2ZrMe_2 (1.5 eq, 0.132 mmol, 0.033 g) were transferred to one arm of a double-Schlenk flask inside an argon-filled glovebox. Pentane (ca. 8 mL) was transferred over the mixture under vacuum at 77 K, and the mixture was stirred for 40 minutes at room temperature. The pale-yellow solution was then filtered to the other side of the double-Schlenk. The mixture was then filtered to the other side of the double-Schlenk. The surface was washed three times of residual Cp_2ZrMe_2 by condensing the pentane in the double-Schlenk over the surface, stirring, and filtering through the glass frit to the other side of the flask. The volatiles were

collected and isolated in a separate Schlenk storage tube fitted with a Teflon-tap and set aside to be analyzed by ^{1}H and $^{19}F\{^{1}H\}$ solution NMR. The surface was then dried under diffusion pump vacuum for 45 minutes. The non-volatile molecular compounds from the grafting were analyzed by rinsing the opposite arm of the double-Schlenk tube with C_6D_6 and analyzing the ^{1}H and $^{19}F\{^{1}H\}$ solution NMR. The Cp_2ZrMe_2-Al LA SiO_2 was collected as a pastel yellow solid and was stored in an Ar glovebox freezer at -20˚C. **FT-IR:** $\nu_{C\text{-}H}$ = 3081 and 2935 (C-H from Cp_2ZrMe) cm^{-1}.

7.6 References

[1] Corma, A.; Garcia, H. *Chem. Rev.* **2003**, *103(11)*, 4307-4366.

[2] Kobayashi, S.; Manube, K. *Pure Appl. Chem.* **2000**, *72(7)*, 1373-1380.

[3] Walker, J. C. L.; Klare, H. F. T.; Oestreich, M. *Nat. Rev. Chem.* **2019**, *4*, 54-62.

[4] Kennedy, J. P.; Feinberg, S. C. *J. Polymer Sci.* **1978**. 2191-2197.

[5] Berchtold, B.; Lozan, V.; Lassahn, P.-G. Janiak, C. *J. Polymer Chem. A*, **2002**, 3604-3613.

[6] Rojas, R. S.; Peoples, B. C.; Cabrera, A. R.; Valderrama, M.; Frohlich, R.; Kehr, G.; Erker, G.; Wiegand, T.; Eckert, H. *Organometallics*, **2011**, *30(23)*, 6372-6382.

[7] Gutmann, V.; Coord. *Chem. Rev.* **1976**, *18*, 225-255.

[8] Beckett, M. A.; Brassington, D. S.; Coles, S. J.; Hursthouse, M. B. *Inorg. Chem. Commun.* **2000**, *3*, 530-533.

[9] Welch, G. C.; Cabrera, L.; Chase, P. A.; Hollink, E.; Masuda, J. D.; Wei, P.; Stephan, D. W. *Dalton Trans.*, **2007**, 3407-3414.

[10] Mewald, M.; Frohlich, R.; Oestreich, M. *Chem. Eur. J.* **2011**, *17*, 9406-9414.

[11] Korte, L. A.; Schwabedissen, J.; Soffner, M.; Blomeyer, S.; BReuter, C. G.; Vishnevskiy, Y. V.; Neumann, B.; Stammler, H.-G. Mitzel, N. W. *Angew. Chem. Int. Ed.* **2017**, *56*, 8578-8582.

[12] Bohrer, H.; Trapp, N.; Himmel, D.; Schleep, M.; Krossing, I. *Dalton Trans.* **2015**, *44*, 7489-7499.

[13] Christe, K. O.; Dixon, D. A.; McLemore, D.; Wilson, W. W.; Sheehy, J. A.; Boatz, J. A. *J. Fluorine Chem.*, **2000**, *101*, 151-153.

[14] Culver, D. B.; Venkatesh, A; Huynh, W.; Rossini, A. J.; Conley, M. P. *Chem. Sci.* **2020**, *11*, 1510-1517.

[15] Jezequel, M.; Dufaud, V.; Ruiz-Garcia, M. J.; Carillo-Hermosilla, F.; Neugebauer, U.; Niccolai, G. P.; Lefebvre, F.; Bayard, F. Corker, J.; Fiddy, S.; Evans, J.; Broyer, J.-P.; Malinge, J.; Basset, J.-M. *J. Am. Chem. Soc.* **2001**, *123*, 3520-3540.

[16] Popoff, N.; Gauvin, R. M.; De, M. A.; Taoufik, M. *Organometallics,* **2012**, *31*, 4763-4768.

[17] Gan, Z.; Chem. Commun. 2006, 4712-4714.

[18] Chen, L.; Wang, Q.; Hu, B.; Lafon, O.; Trebosc, J.; Deng, F.; Amoureux, J.-P. Phys. Chem. Chem. Phys. 2010, 12, 9395-9405.

[19] Nimerovsky, E.; Gupta, R.; yehl, J.; Li, M.; Polenova, T.; Goldbourt, A. *J. Magn. Reson.* **2014**, *244*, 107-113.

[20] Jordan, R. F.; Bajgur, S.; Willett, R.; Scott, B. *J. Am. Chem. Soc.* **1986**, *108*, 7410-7411.

CHAPTER 8

Conclusion

8.1 Conclusion

Solid-state NMR with the aid of computational modeling is a valuable technique in the structure elucidation of both molecules and surface-supported molecular fragments. The chemical shielding tensors and electric field gradient tensors give rise to important spectroscopic observables in multinuclear solid-state NMR such as the isotropic chemical shift, span, and quadrupolar coupling constant that can be used to probe the environment around the nucleus of interest. Density functional theory, specifically the natural localized molecular orbital decomposition of the contribution to NMR properties, is especially useful in understanding the primary coordination sphere of a nuclei.

Chapter 2 – 4 presented a series of permethylscandocenes that eventually resulted in the unambiguous characterization of Cp^*_2Sc-Et synthesized by Bercaw and co-workers in 1987. A series of Cp^*_2Sc-X and Cp^*_2Sc-X(THF) (X = F, Cl, Br, I) were studied and the remarkably larger C_Q values in Cp^*_2Sc-X than compared those of Cp^*_2Sc-X(THF) helped guide the study of Cp^*_2Sc-OR (R = $SiPh_3$, fluorinated tertbutoxides) and the surface-supported Cp^*_2Sc fragment. Importantly, the larger C_Q values resulted from tri-coordinate scandium sites, and the smaller C_Q values were associated with four-coordinate scandium sites. The synthesis and study of these molecular scandocene complexes guided the elucidation of structure for $Cp^*_2ScOSi{\equiv}$ and $Cp^*_2Sc(OSi{\equiv})O(SiO_x)_2$.

The concept of geometric perturbations affecting the C_Q of quadrupolar nuclei are not unique to scandium. Chapter 5 revisited coinage metal complexes of diboraanthracene ligands B_2P_2 and whether each contained a M → BR_3 interaction. While the X-ray crystal structures revealed trigonal planar boron environments for cationic $M(B_2P_2)^+$ (M = Cu, Ag, Au) complexes and a tetrahedral boron environment for anionic $Au(B_2P_2)^-$, solid-state $^{11}B\{^1H\}$ NMR revealed the solvent-free signals of each complex. In addition, DFT studies provided a thorough understanding of the origin of the isotropic chemical shift and C_Q in these compounds.

Chapter 6 explored the origin of the ^{29}Si NMR chemical shift of R_3Si-X in relation to the formation of silylium ions in both molecular compounds and $–SiR_3$ fragments supported on solid supports. In particular, the orientation of the chemical shielding tensor preferentially coupled the σ(Si-C) to the σ*(Si-X) in these compounds. In addition, the dependence of the ^{29}Si NMR chemical shift being a result of the paramagnetic chemical shielding and its effect on orbital rotation model is highlighted. In particular, the ^{29}Si NMR chemical shift is not a result of the charge accumulation on silicon.

Chapter 7 explored the experimental structure of ≡Si–OH---$Al(OC(CF_3)_3$ and $[Cp_2ZrCH_3][≡SiOAl(OC(CF_3)_3)_2(CH_3)]$ via multinuclear solid-state NMR. While there are a variety of spectroscopic experiments to gain an understanding of these materials, the computational models of each helped guide the assignment of structure in these complexes. Chapter 7 demonstrates that a combination of solid-state NMR and DFT is a powerful technique in structure elucidation for a variety of systems including species that are supported on amorphous solids.